Jan Auffenberg

Production of Direct Photons in Ultra-Relativistic d + Au Collisions Measured by the PHENIX Experiment

— 2006 —

Experimentelle Physik

Production of Direct Photons in Ultra-Relativistic d + Au Collisions Measured by the PHENIX Experiment

Diplomarbeit
vorgelegt von

Jan Auffenberg

aus Lippstadt

Westfälische Wilhelms-Universität Münster
Institut für Kernphysik

— 2006 —

Inhaltsverzeichnis

1. Introduction

Since the beginning of the 21st century the Relativistic Heavy Ion Collider observes the traces of heavy-ion collisions. Until the year 2003 five different types of collisions with center of mass energies of up to $\sqrt{s_{NN}} = 200\,\text{GeV}$ were studied. The most important collisions at this time were Au + Au with $\sqrt{s_{NN}} = 200\,\text{GeV}$ and p + p.
The first results on Au + Au collisions gave evidence for the existence of a new kind of thermodynamic phase, the Quark-Gluon Plasma, expected at high densities and temperatures. It has been predicted that such a state of matter existed a few microseconds after the Big Bang. To understand the complex interactions of the point-like quarks and gluons, called partons, when colliding two huge "clumps" like gold ions with high center of mass energies, it is important to study the properties of more simple collisions like p + p with the same center of mass energies. Particles coming from hard scatterings[1] are the dominant source of particle production with high transverse momenta in such high-energy p + p collisions. The measurement of particle yields confirm Quantum Chromodynamic (QCD) and its perturbative model calculations (pQCD), that model the strong interaction. It was found that the experimental results in p + p collisions are well described by such pQCD predictions at sufficiently high transverse momenta.
A comparison of the total cross sections of hadrons and direct photons in Au + Au and p + p collision shows two interesting facts:

First, it was an important result to observe that the production of the π^0 and other hadrons at high transverse momenta is suppressed in central gold collisions. The phenomenon can be explained with energy loss of particles in a hot and dense medium created in collisions with high energy densities. It is called *jet quenching*.

Second, in contrast to jet quenching for hadrons, the production of direct photons, i.e. photons not coming from hadronic decays, are not suppressed in central collisions. Thus, the total cross section for direct photons with high transverse momenta in p + p collisions scales with the number of partons involved in a Au + Au collision N_{coll}.

This leads to different possible interpretations. Perhaps the suppression of the total cross section of hadrons in Au + Au collisions is a final state effect[2] of hot and dense matter, e.g. a QGP. A alternativ theory for the suppression of hadrons is e.g. the color

[1] Hard scattering mean in simple words direct scatterings of quarks and gluons with large momentum transfer.

[2] Final state effects are called effects after hard scatterings.

glass condensate (CGC), a initial state effect[3] of the colliding matter. An possible explanation for the suppression of hadrons in both scenarios would be parton energy loss. If direct photons do not interact with the medium and no other remakable sources of direct photons apart from hard scatterings exist, they would not be "quenched". This would also explain the scaling behavior of the cross section for direct photons.
To test these theories and to observe properties of cold nuclear matter , it has been decided to collide gold nuclei with deuterium at the same center of mass energies as in Au + Au and p + p in the year 2003.
It has been observed in those d + Au collisions that the production of π^0 and η is not suppressed scales with N_{coll}. For direct photons the scaling of the production rates should be the same.
Thus the main motivation of this thesis is to analyse direct photons in such d + Au collisions measured with the PHENIX experiment at $\sqrt{s_{NN}}$ = 200 GeV and to find the direct photons as a function of transverse momentum suppressed or not.
A enhancement of direct photons at intermediate transverse momenta would give evidence for new medium effects of cold nuclear matter.
If the direct photons scale with N_{coll} for d + Au collisions in respect to p + p, this would give a new evidence for jet quenching as a final state effect of hot and dense nuclear matter, e.g. QGP.

The outline of this thesis is as follows. First, some basics of nuclear matter at high energies and of ultrarelativistic collisions are presented in Chapter 2. The PHENIX experiment at BNL is then described in Chapter 3. Chapter 4 explains the different analysis steps which lead to the direct photon spectra. The results are presented and discussed in Chapter 5.

[3] Initial state effects are called effects before hard scattering.

2. Theoretical Basics

Since the mid 80's one of the aims of experimental programs colliding highly energetic nuclei is to create highly excited strongly interacting matter in an extended region of space time. It is still not answered for sure what kind of matter is observed in these experiment (hadronic or nucleonic). The PHENIX experiment is one of the experimental programs that aims at observing the different kinds of hot and dense matter and extract their different properties. For that it is of great importance to understand the different properties of the different kinds of matter and its signals as will be outlined in the following.

2.1 Quarks and Gluons

The currently most popular theory of matter and its interactions is the *standard model*. It describes the structure of matter and its interaction properties and divides the number of existing particles into three groups, *quarks*, *leptons* and *gauge bosons*. While quarks are strongly interacting particles and form *hadrons*, leptons are only interacting via the weak and the electromagnetic force. The gauge bosons are the interaction quanta of the four interactions[1]. Table 2.1 shows the *fermions* (quarks and leptons) subdivided into their three *families*. These spin 1/2 particles follow the Fermi-Dirac statistics and therefor have to obey the Pauli principle. The six different kinds of quarks, also called *flavors*, allow to construct the hadrons, with *baryons* containing three quarks (qqq) and *mesons* made up of quark-anitquark pairs ($q\overline{q}$). The existence of three quark states like Ω^- motivated a quantum number called *color* to satisfy the Pauli principle. The experimental observation that no single quarks are observed leads to the assumption that only color neutral objects can exist in nature.

The theory of strongly interacting quarks is Quantum Chromodynamic (QCD). Based on concepts of the description of electrically charged particles in the Quantum Electrodynamic (QED), the QCD differs in the interaction possibilities. This is due to the fact that in the electromagnetic interaction the uncharged photon mediates the interaction force, while in QCD the gluons themselves carry a color charge and interact among each other. In QCD eight different gluons exist, each a combination of color and anticolor. Another difference of QCD in comparison to QED is the coupling constant of the strong interaction α_s. The coupling constant α_s can be up to two orders of magnitude larger than the electromagnetic coupling constant $\alpha = 1/137$. Hence multiple gluon exchanges $(\alpha_s^2, \alpha_s^3, ...)$

[1] strong, electromagnetic, weak interaction and gravity

	Leptons			Quarks		
		Charge	Mass		Charge	Mass
1.	e	$-1e$	$0.511\,\mathrm{MeV}/c^2$	u	$+2/3e$	$1.3-4\,\mathrm{MeV}/c^2$
	ν_e	0	$<3\,\mathrm{eV}/c^2$	d	$-1/3e$	$4-8\,\mathrm{MeV}/c^2$
2.	μ	$-1e$	$105.7\,\mathrm{MeV}/c^2$	c	$+2/3e$	$1.15-1.35\,\mathrm{GeV}/c^2$
	ν_μ	0	$<0.19\,\mathrm{MeV}/c^2$	s	$-1/3e$	$80-130\,\mathrm{MeV}/c^2$
3.	τ	$-1e$	$1777\,\mathrm{MeV}/c^2$	t	$+2/3e$	$\approx 174\,\mathrm{GeV}/c^2$
	ν_τ	0	$<18.2\,\mathrm{MeV}/c^2$	b	$-1/3e$	$4.1-4.4\,\mathrm{GeV}/c^2$

Table 2.1: Mass and charge of the three generations of fundamental fermions.

contribute significantly to the interaction amplitudes, making perturbative calculations similar to QED inadequate in most situations and leads to another important feature: the force of the strong interaction increases with distance and leads to two interesting effects, the *confinement* and the *asymptotic freedom*.
The confinement can be illustrated with the phenomenological potential for the strong interaction given in [Per98]:

$$V_s = -\frac{4}{3}\frac{\alpha_s}{r} + kr, \tag{2.1}$$

where the first term, dominating at small r between two quarks, is similar to the Coulomb potential and the second linear term can be associated with the confinement at larger r. Because of the linear term, attempts to free a quark from a hadron simply results in the production of new $q\overline{q}$ pairs, i.e. mesons when its energetically more favorable than forming a gluon tube or string.

The asymptotic freedom can be motivated with a leading order perturbative approximation of the coupling constant in dependence of the momentum transfer Q^2. This leads to the equation:

$$\alpha_s(Q^2) \approx \frac{12\pi}{(33-2\cdot n_f)\cdot \ln\frac{Q^2}{\Lambda^2}}, \tag{2.2}$$

where n_f are the number of degrees quark flavors (6). Λ is the QCD scale parameter, which has to be determined experimentally and is found to be $\Lambda \approx 200-400$ MeV/c, depending on several parameters. For more details see for example [Cas98]. Because of the perturbative approximation in leading order, Equation (2.2) is only valid for

$Q^2/\Lambda^2 \gg 1$, but it illustrates that at asymptotically large Q^2 the coupling $\alpha_s\left(Q^2\right) \to 0$. In this limit the quarks behave as if they were free.

2.2 Phase Transition to the Quark-Gluon Plasma

QCD calculations have predicted a phase transition from hadronic matter to quark matter at a certain temperature already in the mid 70's [Wil74]. The so called *lattice* QCD calculations (LQCD) formulate the gauge theory of QCD on a discrete lattice of space time. This approach has the advantage that it retains the fundamental characteristics of QCD and makes it accessible to computational methods. In face of the non-perturbative character of QCD calculations of the properties of quarks and gluons, e.g. the thermodynamic equation of state for strongly interacting matter, are made with such LQCD methods.

However, LQCD calculations are heavily limited by computing resources, making it difficult to use physical quark masses m_q and a negligible lattice spacing a, the *chiral limit* $m_q \cdot a \to 0$, as well as finite baryo-chemical potential. A modern LQCD calculation is shown in Figure (2.1). It illustrates the sudden rise of the energy density ε/T^4 at a critical temperature $T_c \approx 170$ MeV for different numbers of quark flavors. This is on the same order of magnitude than in bag model calculations [Won94] and interpreted as the phase transition into a *deconfined* quark-gluon plasma phase [Kar02]. After this phase transition quarks and gluons that are normally bound in hadrons can move freely.

A sketch of the current understanding of the phase diagram is given in Figure (2.2). The baryochemical potential μ_b is a measure of the baryon density of the system. It represents the necessary energy to add another baryon to the system. The QGP transition is also interesting from a cosmological and astrophysical point of view. In the Big Bang scenario of the origin of the universe the hadrons are produced in the freeze-out from a QGP phase with high temperature and low baryon density on the order of $1\,\mu$s after the Big Bang. Another example for a QGP possibly reached in nature are neutron stars. Here very high baryon densities are reached which could lead to a QGP-phase transition at very low temperature.

Besides deconfinement another characteristic of the phase transition is expected from LQCD calculations: the restoration of *chiral symmetry* at high temperature and density. This is explained for example in [Tho01].

2.3 Ultra-Relativistic Heavy-Ion Collisions

Reactions with center of mass energies for each nucleon-nucleon pair $\sqrt{s_{NN}} \geq 10$ GeV are called *ultra-relativistic*. Collisions with such energies provide the opportunity to study

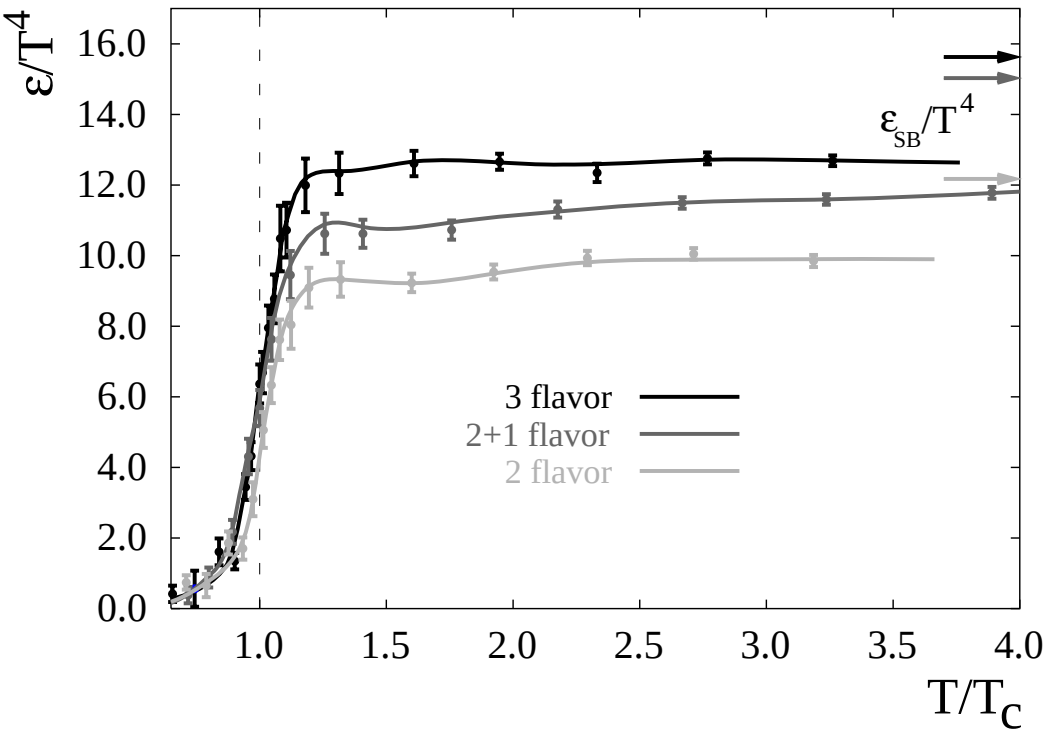

Figure 2.1: Lattice QCD results for normalized energy density ε/T^4 versus temperature for different quark configurations [Kar02]: two degenerate flavors, two degenerate light flavors plus one heavy, and three degenerate flavors. The expectation for an ideal gas with quark and gluon degrees of freedom, the Stefan-Boltzmann limit, is also shown.

strongly interacting matter at high energy densities which might be sufficient to create a quark-gluon plasma. However, a single indisputable signature for the creation of a quark-gluon plasma is not known. It is an experimental challenge to find observables that reflect the QGP, which are not entirely diluted by the later stages of the reaction, in the detected products of the nuclear collision. In order to find characteristic QGP signals, not only heavy ion collisions are studied, but also collisions which help to verify their signals, for example nucleon-nucleon collisions.

Nucleon-nucleon reactions, for example p + p, provide an important baseline for nucleon-nucleus or nucleus-nucleus collisions. Above a center of mass energy of $\sqrt{s_{NN}} > 10\,\text{GeV}$ the total cross section for p + p collisions is roughly constant at $\sigma_{tot} \approx 40$ mb. Inelastic reactions are the main part of the cross sections of collisions with these energies. It this case the colliding particles lose a large fraction of their energy, with the deposited energy resulting in new particles. Most of this particles, about 90%, are pions and have small transverse momenta ($p_\text{T} < 2$ GeV/c). In this p_T region the particle production is domi-

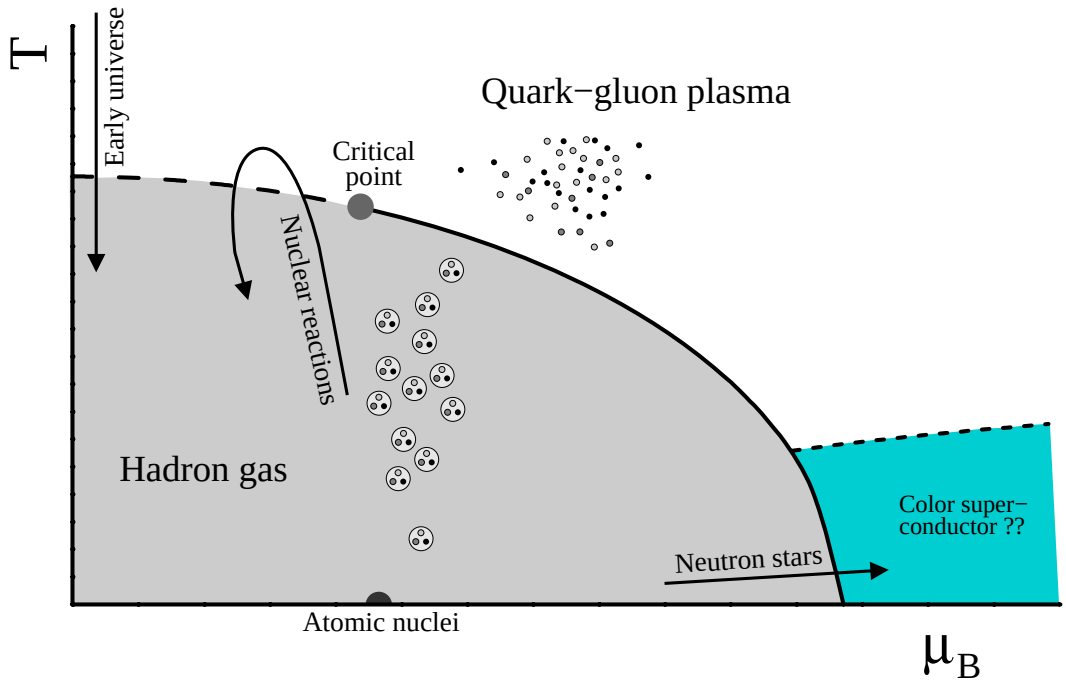

Figure 2.2: A schematic phase diagram of strongly interacting matter. The solid line indicates the first order phase transition from hadronic matter to the quark-gluon plasma. The dashed line at small baryon density represents a crossover transition [IKP06].

nated by so-called *soft* processes.
At low transverse momenta the total cross section can be parametrized with an exponential function:

$$\frac{d\sigma}{dp_T^2} \propto e^{-\alpha p_T}, \tag{2.3}$$

with $\alpha \approx 6\ c/\text{GeV}$.
The extrapolation of the exponential function fails for large p_T. The distribution is better described by a power law:

$$\frac{d\sigma}{dp_T^2} \propto p_T^{-n}. \tag{2.4}$$

In this kinematic region the particle production is governed by so-called *hard* processes, where the α_s is sufficiently small to apply pQCD.

It is a phenomenological observation that the differential cross sections for various hadrons have the same form when expressed as a function of the transverse mass $f(m_T)$ [Bou76]:

$$E\frac{d^3\sigma_h}{dp^3} = C_h \cdot f(m_T), \tag{2.5}$$

with

$$m_T = \sqrt{p_T^2 + m_0^2}. \tag{2.6}$$

This so-called m_T-scaling is used to estimate the production of hadrons like η' or ω which are not directly measured relative to π^0 [Kau04] to calculate the background of radiative decays in measured photon spectra (see Section 4.2.2).

To describe the space-time evolution in heavy-ion collisions, one make use of the fact that the de-Broglie wavelength of the individual nucleons is so small that the nuclei can be seen as an independent accumulation of nucleons. This simple view implies that the Lorentz-contracted nuclei interact only in the geometrical overlap region determind by an impact parameter *b*, as can be seen in Figure 2.3, where the corresponding nucleons are called *participants* and the nucleons outside the geometrical overlap are called *spectators*. The participants interact in the reaction zone, leading to the formation of a hot and dense region, the *fireball*.

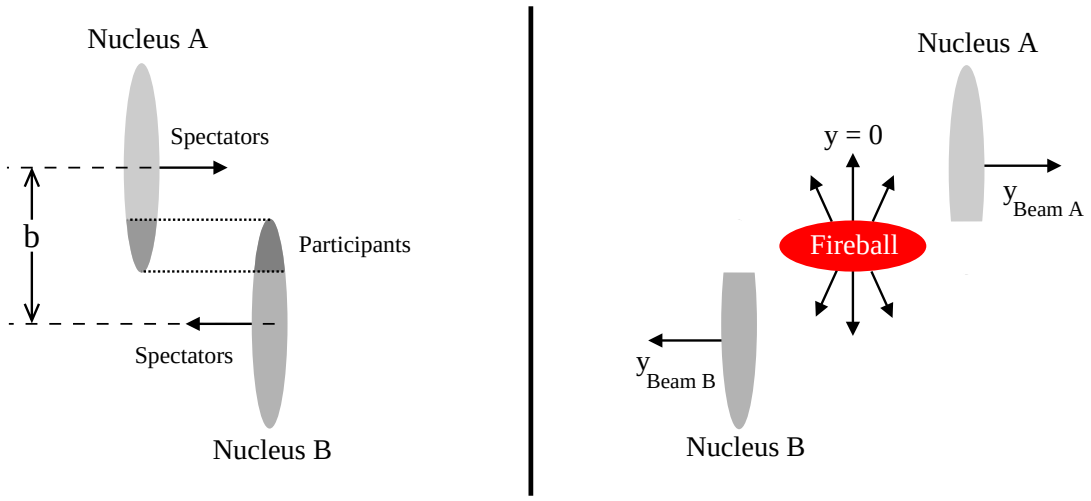

Figure 2.3: Schematic view of two colliding nuclei in the geometrical participant-spectator model. The distance between the centers of the two Lorentz contracted nuclei is the impact parameter $\vec{b}$ [IKP06].

The system reaches its thermodynamic equilibrium during this formation. Beyond a certain energy density the system is assumed to form a QGP. Then the expanding plasma cools down. Below the critical temperature T_c, hadrons are created which form a hadron gas. The formation of the hadron gas possibly occurs via a mixed phase with domains of a co-existing QGP. Finally the temperature of the system decreases with expansion of the system to the so-called thermal *freeze-out*, before the created hadrons decouple completely in the chemical freeze-out.

2.4 Probes for a Quark-Gluon Plasma Phase

The formation of a quark-gluon plasma would have a variety of probes. Most of the signals can be described in different models without phase transition. But a simultaneous description of all signatures without assuming a phase transition is not available. Furthermore it is difficult to measure the signals from a QGP, because of its fleeting existence and of the background effects resulting from the subsequent hadron gas. For many signatures of the QGP it is important to compare reactions which could create a QGP with more elementary reactions like p + p or d + Au collisions at the same energy. These control experiments help to understand effects in cold nuclear matter under similar premises. An overview of some of the predicted QGP signals will be given in the following. For a more complete review, see e.g. [Har96, Fis06].

2.4.1 Kinematic Probes

A phase transition influences on the thermodynamical properties like temperature, pressure, energy density, and entropy of the system or their mutual dependence to each other. For example, a change in the number of the degrees of freedom, when going from a quark-gluon plasma back to a hadron gas, can have direct impact on the dependence of the energy density on the temperature. The average transverse momentum of particles $\langle p_{\mathrm{T}} \rangle$ in the QGP phase is in principle related to the temperature of the system. But hadrons do interact after the chemical freeze-out from the QGP in the hadron gas, which dilutes the direct connection to the temperature. A better probe may be provided by thermally produced dileptons and photons, which do not suffer strong final state interactions, as discussed below.

2.4.2 Electromagnetic Probes

The fact that electromagnetic probes are not affected by the strong force is the main advantage of, for example, direct photons or lepton pairs. They are created basically

throughout all stages of the reaction and can provide a direct measure of the evolution of the fireball. The investigation of direct photons is the main part of this work and is therefore explained in Section (2.7).
Another particle production channel in a QGP phase is given by the quark-antiquark annihilation into dileptons $q\bar{q} \rightarrow l^+l^-$. This process depends on the thermal distribution of the quarks and antiquarks in the plasma. However it is covered by the Drell-Yan production, which is the annihilation process of a valence quark with a sea antiquark, already present in nucleus-nucleus collisions, and the lepton production in a hadron gas via the process $\pi^+\pi^- \rightarrow l^+l^-$. For more details see e.g. [Won94].
In addition the measurement of ρ, ω and ϕ mesons via their dileptonic decay branch could be a interesting probe for a QGP phase. Their mass might be influenced by chiral symmetry restoration, as will be described below.

2.4.3 Probes for the Deconfined Phase

The strangeness enhancement is another prediction concerning the QGP. For the production of ϕ $(s\bar{s})$ in a QGP only the current quark mass of approximately 300 MeV/c^2 is needed while the simplest reaction in a hadron gas $pp \rightarrow \Lambda^0 K^+ p$ to create a strange quarks needs 700 MeV/c^2.
The J/Ψ supression is another promising probe for deconfinement, as the bound $c\bar{c}$ state is primarily produced in hard parton-parton scatterings due to its large mass ($m_{J/\Psi} = 3079\,\mathrm{MeV}/c^2$). In a QGP the attractive potential between a $c\bar{c}$ is screened by the large density of free color charges in the medium. During the QGP following hadronization the disassociated charm quarks couple with a larger probability to the abundant lighter u and d quarks instead of recombining to J/Ψ.
The quarks and gluons, produced in initial hard scatterings, should be influenced by the large color charge density in the deconfined phase of a QGP by losing energy. This is discussed seperatly in Section (2.6).

2.4.4 Probes for Chiral Symmetry Restoration

The formation of a disoriented chiral condensate (DCC) may be a probe for the restoration of chiral symmetry. The deconfined phase of a QGP can prelude the restoration of chiral symmetry. When the transition from the phase with restored chiral symmetry back into the chirally broken ground stade occours very fast, the chiral condesate may populate an energetically less favourable state than "usual" nuclear matter, a DCC. Possible signatures for the creation of a DCC are random fluctuations between the production

amplitudes of the pion isospin-triplet (π^+, π^0, π^-), different from the usual value of $N_{\pi^X}/(N_{\pi^+} + N_{\pi^0} + N_{\pi^-}) \approx 1/3$, as discussed in [Pei97].
Another effect for the chiral symmetry restoration is a modification of the mass and decay width of the light vector mesons ρ, ω, and Φ, which are usually detected via their e^+e^- decay channel.

2.5 The Nuclear Modification Factor

As already mentioned above for the large momentum transfer in initial hard scatterings the partons can be considered as asymptotically free, as in p + p collisions. The cross section in a collision of two nuclei $A+B$ or a nucleon and a nucleus $n+A$ should be connected to the p + p cross section by a scaling factor, the number of inelastic binary nucleon-nucleon collisions N_{coll} in the reaction.
For $A+B$ as for $n+A$ collisions at a fixed impact parameter N_{coll} is proportional to the nuclear thickness function $T_{AB}(b)$. The impact parameter b is shown in Figure (2.3). $T_{AB}(b)$ is analogous to an integrated "nucleon luminosity" for two overlapping colliding systems, as illustrated in Figure (2.3) for $A+B$ collisions. In addition each centrality selection by the experiment samples a different distribution of impact parameters. The cross section for a high-p_T particle h produced in an $A+B$ collision with centrality f is linearly connected to the p + p cross section via the average nuclear thickness $\langle T_{AB} \rangle_f$:

$$\left.\frac{1}{N_{AB}^{\mathrm{evt}}} \frac{\mathrm{d}^2 N_{AB}^h}{\mathrm{d}p_{\mathrm{T}} \mathrm{d}y}\right|_f = \langle T_{AB} \rangle_f \cdot \frac{\mathrm{d}^2 \sigma_{\mathrm{pp}}^h}{\mathrm{d}p_{\mathrm{T}} \mathrm{d}y}, \tag{2.7}$$

with:

$$\begin{aligned} \langle T_{AB} \rangle_f &= \frac{\int_f T_{AB}(b) \mathrm{d}^2 b}{\int_f \left(1 - e^{-\sigma_{\mathrm{NN}} T_{AB}(b)}\right) \mathrm{d}^2 b} \\ &= \frac{\langle N_{\mathrm{coll}} \rangle_f}{\sigma_{\mathrm{nn}}}, \end{aligned} \tag{2.8}$$

where $\langle N_{\mathrm{coll}} \rangle_f$ is the average number of inelastic, binary nucleon-nucleon collisions with an inelastic cross section σ_{nn}. To calculate the average nuclear thickness function and $\langle N_{\mathrm{coll}} \rangle$ for a given centrality a Glauber Monte Carlo method is used [Kel00]. Many medium effects are usually studied by means of the *nuclear modification factor* R_{AB}:

$$\begin{aligned} R_{AB} &= \frac{\mathrm{d}N_{AB}^h}{\langle T_{AB} \rangle_f \cdot \mathrm{d}\sigma_{\mathrm{nn}}^h} \\ &= \frac{\mathrm{d}N_{AB}^h}{\langle N_{\mathrm{coll}} \rangle_f \cdot \mathrm{d}N_{\mathrm{nn}}^h}, \end{aligned} \tag{2.9}$$

which is expected to be unity above a certain p_{T}, where hard scattering is the dominant source of particle production, and in the absence of any medium effects.
Discrepancies to the behavior of for example p + p collisions can now directly be seen in a deviation of R_{AB} from unity. Examples for possible medium effects leading to a deviation concerning p + p are given in the next section.

2.6 Jets and Jet Quenching

Most of the particles with high transverse momenta are produced in hard scatterings of the colliding participants. In nucleon + nucleon collisions the scattered partons fragment directly in the QCD vacuum. The fragments form *jets* of particles, hadrons and photons, along the direction of motion of the primordial parton. The hard inelastic cross section to produce hadrons is calculable via perturbative QCD (pQCD) invoking the factorization theorem [Col85]:

$$E\frac{\mathrm{d}^3\sigma^{\mathrm{hard}}_{\mathrm{NN}\to\mathrm{h}}}{\mathrm{d}p^3} = \int \sum_{a,b,c} f_a(x,Q^2)\otimes f_b(x,Q^2) \otimes\frac{\mathrm{d}\sigma^{\mathrm{hard}}_{ab\to c}}{\mathrm{d}^3p}\otimes D_{c/h}\left(z,Q^2\right). \tag{2.10}$$

The different factors are:

- The non-perturbative distribution functions $f_{q,g}(x,Q^2)$ of partons in the colliding nucleons, which depend only on the momentum transfer and the parton fractional momentum x. They can be determined e.g. in deep-inelastic electron-nucleus reactions,
- The short-distance, perturbatively computable parton-parton scattering $ab \to c$,
- The fragmentation function $D_{c/h}\left(z,Q^2\right)$ of the scattered parton c into a hadron h carrying a fraction $z = p^h/p^c$ of the parton momentum. The fragmentation function reduces for photons to a $\delta(1-z)$ function.

It has to be noted that the calculation of total cross sections via Equation (2.10) suffers from uncertainties due to the arbitrary choice of factorization, renormalization and fragmentation scales. The scales are usually chosen identical and on the order of the transverse momentum and build a huge part of the uncertainty of pQCD calculations.

In collisions where heavy ions are involved, the hard scattering processes occur in the initial state of the collision. Thus the scattered partons may have to transverse the hot dense medium before they fragment into hadrons and can interact with the matter produced in later stages of the collision. A colored medium should distort the back-to-back correlation of particle jets and lead to a suppression of particle production at high p_{T} compared to p + p collisions, the *jet quenching* [Gyu90, Bai95].

2.6.1 Effects of Cold Nuclear Matter

It is important for the observation of parton energy loss or jet quenching, which should lead to $R_{AB} < 1$, to know all other medium effects leading to a modification of the particle production compared to nucleon-nucleon collision. To collide nucleons with large nuclei or small nuclei with large nuclei is a possibility to observe those effects. Possible medium effects are:

- Enhanced particle production by multiple soft scattering.
- Modification of the particle distribution function in the initial state.
- Absorption or energy loss due to passage through cold matter.

Cronin Effect

Comparisons of p + p and p + A collisions with center of mass energies of $\sqrt{s} \lesssim 8$ GeV have shown that the cross section does not simply scale with the number of nucleons A involved in the collision. This was first shown by Cronin et al. in 1974 [Cro75] with a proton beam on beryllium, titanium and tungsten targets. It was found that the cross section for a given p_{T} scales like:

$$E\frac{\mathrm{d}^3\sigma}{\mathrm{d}p^3}(p_{\mathrm{T}},A) \quad = \quad E\frac{\mathrm{d}^3\sigma}{\mathrm{d}p^3}(p_{\mathrm{T}},1)\cdot A^{\alpha(p_{\mathrm{T}})}, \tag{2.11}$$

with $\alpha > 1$ for transverse momenta larger than approximately 2 GeV/c. This effect is called *Cronin effect*. The reason for this effect is dedicated to be multiple soft scatterings of the incoming nucleons, leading to an additional broadening in their transverse momentum.

Nuclear Shadowing

Each parton in a nucleon carries a small fraction x of the complete momentum of the hole nucleon. As the same is valid for nuclei, particle distribution functions (PDF) [Per98]

give the probability to find a parton with momentum fraction x. The PDF differs for nuclei ($F_2^A(x,Q^2)$) and free nucleons ($F_2^p(x,Q^2)$) as measured in various deep inelastic scattering experiments [Pil00]. Effects of the different PDFs can be described by $R_F = F_2^A/F_2^d$, using the PDF of deuterium ($F_2^d(x,Q^2)$) as an approximation to the average structural function of nucleons. The observed effects are:

$R_F < 1$:	nuclear shadowing	for $0.0 \leq x \leq 0.1$
$R_F > 1$:	anti shadowing	for $0.1 \leq x \leq 0.2$
$R_F < 1$:	EMC effect	for $0.3 \leq x \leq 0.8$
$R_F > 1$:	Fermi motion	for $x \to 1$

The Color Glass Condensate

The *color glass condensate* (CGC) provides a solution for the so called *small x problem* [Fro61]. This CGC has also implications for the particle production in heavy-ion collisions [Ian03]. The basic idea of the color glass condensate is that at sufficiently high gluon densities not only the coupling constant becomes weak, but the gluons can also start to fuse ($gg \to g$), which limits the gluon density at small x.
The number of gluons seen by a hadronic probe or a photon [2] when traversing the nucleus A is propotional to $A^{1/3}$. Q_S, the saturation scale where the CGC effects become important [Kha03], depends not only on the number of seen gluons, but also on the rapidity region since the probed x region decreases with $x \propto e^{-y}$. If the saturation scale is reached in RHIC collisions at large transverse momenta, the depletion of the gluon density implies a reduction of the nuclear modification factor already in d + Au collisions.

2.6.2 Effects of Hot and Dense Nuclear Matter

Similar to cold nuclear matter, hot and dense nuclear matter has several properties which might influence the particle production. Where some properties between cold and hot matter are in principle the same, they can change in influence:

- Nuclear shadowing depends on the PDF of the matter and should influence the passage of partons to hot dense matter.
- The color glass condensate is the initial state for a QGP and could influence the colored medium.

[2] e.g. via annihilation

- Gluon bremsstrahlung leads to an energy loss of traversing partons in hot dense matter.

Parton Energy Loss

Similar to electromagnetic bremsstrahlung of an electron passing through matter, a parton which traverses a colored medium loses energy by radiating soft gluons [Wan92]. The theoretical treatment is complicated by the fact that a destructive interference effect of the emitted gluons has to be considered if the formation time of the gluons $\tau \approx \hbar/E_g$ is large compared to its free path λ/c in the medium (e.g. [Gyu90]). First studies of the passage of highly energetic electrons or photons through highly energetic matter were already made in the mid 50's. The effect is known as the Landau-Pomeranchuk-Migdal effect (LPM) [Mig56].
The total energy loss of a parton $\Delta E/\Delta x$ influenced by this quantum interference depends on the density of the medium and is proportional to its path length L through the medium [Bai97]:

$$\frac{\Delta E}{\Delta x} \propto \frac{L}{\lambda} \ln \frac{L}{\lambda}. \tag{2.12}$$

It has to be remarked that this growth of energy loss is only valid for a static medium but not in heavy-ion collisions, where a rapid decrease of the energy density and color charge density in the expanding fireball has to be taken into account.
The most commonly used description of the parton energy loss [KB04] is the GLV formalism which is explained in [Gyu00].

2.7 Direct Photons

The examination of direct photons is an important tool to study the properties of the different kinds and the different stages of heavy-ion collisions. As photons are not influenced by the strong interaction and of hadronization processes, direct photons provide to be useful to examine the quark-gluon plasma. *Direct* photons are all photons not originating from hadronic decays, e.g. $\pi^0 \rightarrow \gamma\gamma$ or $\eta \rightarrow \gamma\gamma$. They are usually further subdivided into *thermal* photons, emitted from a thermally equilibrated phase, and into *prompt* photons produced in early hard scatterings. While a clear experimental separation of thermal and prompt photons is not possible, a region of transverse momenta can be given, where the different direct photon sources should be dominant. It is expected, that for heavy-ion collisions at lower transverse momenta $1\,\mathrm{GeV}/c \lesssim p_\mathrm{T} \lesssim 3\,\mathrm{GeV}$ the thermal signal gives the largest contribution to the total direct photon yield. At high p_T hard scattered prompt

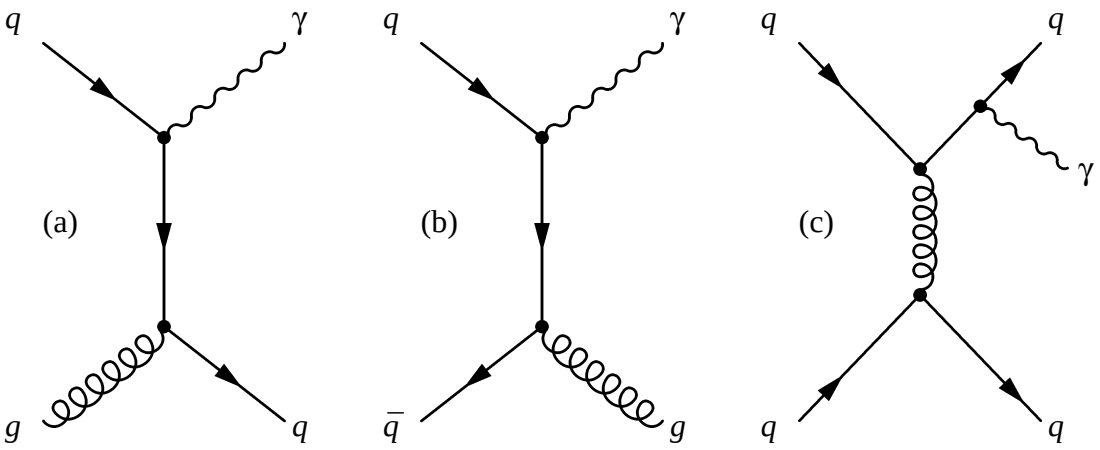

Figure 2.4: Feynman graphs of the main production processes for direct photons in initial hard scatterings as well as in a thermalized quark-gluon plasma phase: (a) quark-gluon Compton scattering of order $\alpha_s\alpha$, (b) quark-antiquark annihilation of order $\alpha_s\alpha$, (c) Bremsstrahlung of order $\alpha_s^2\alpha$.

photons are the dominating part of the yield, as large momentum transfers in particle collisions lead statistically to high transverse momenta. The following subsections will give a short overview of the different direct photon sources during all stages of different kinds of particle collisions. For more details see e.g. [Won94, Pei02, KB04, Pau05].

2.7.1 Prompt Direct Photons

Prompt direct photons are produced in early hard parton-parton scatterings. They are the dominant part of non-thermal direct photons and produced similar to hadrons with large transverse momentum given in Equation (2.10). The only difference is that the fragmentation function reduces to a $\delta(1-z)$ function.
The main underlying processes for pQCD are given in Figure 2.4. The processes in leading order (LO) perturbation theory produce real photons via quark- antiquark annihilation $(q\bar{q} \rightarrow g\gamma)$ and by a quark-gluon Compton scattering $(qg \rightarrow q\gamma)$ while the Bremsstrahlung process, in which a quark radiates a photon, is a next-to-leading-order (NLO) process.
In p + p collisions the prompt photons are the only direct photons source as there is no thermally equilibrated phase. PQCD calculations give a good description of prompt photons produced in hard p + p collisions as shown in Figure 2.5
For the production of direct photons in p + *A* collisions the same effects become important as for the hadron production as explained in Section 2.6:

- The nuclear p_T broadening effect, called Cronin effect,

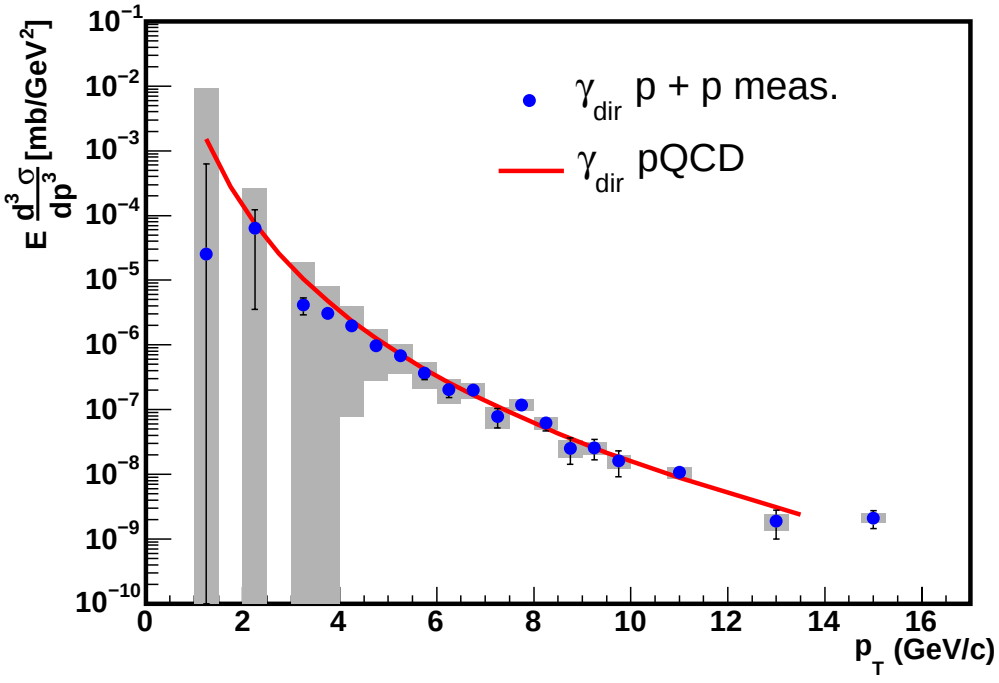

Figure 2.5: Direct photon spectrum of p + p collusions with $\sqrt{s} = 200\,\text{GeV}$ measured with the PHENIX experiment together with pQCD predictions of W. Vogelsang [Zau05]. The pQCD data points are listed in Appendix F.

- shadowing effects of the nuclear distribution functions and
- the effect of a reduced "gluon thickness" caused by a CGC.

Thus d + Au collisions help understanding direct photon signals of $A+A$ collisions, where thermal photons are presumed for a quark-gluon plasma. Especially the Cronin effect can be a rather significant contribution to the total yield in the intermediate p_T range, where the largest thermal signal of the QGP is expected. This has been demonstrated for the measurement of direct photons at SPS energies and for RHIC energies in [Dum01] by smearing the transverse momentum of the hard scattered partons with a Gaussian distribution:

$$f(k_T) = \frac{1}{\pi \langle k_T^2 \rangle} e^{-k_T^2/\langle k_T^2 \rangle}. \tag{2.13}$$

The smearing parameter of the Gaussian is a transverse momentum called k_T.

2.7.2 Thermal Direct Photons from a QGP

The processes in the QGP which lead to direct photon emission are the same as for prompt photons, shown in Figure 2.4. The QGP emits thermal photons like every thermal source with the difference, that e.g. in stars the photons themselves are thermalized, whereas the mean free path of photons in a QGP is large and so the photons are not likely to interact, although the quarks and gluons should be thermalized. Basis for the calculation of the corresponding emission rates are the two LO contributions (annihilation and compton). They can be determined analogous to the equivalent QED processes $e^+e^- \rightarrow \gamma\gamma$ and $e\gamma \rightarrow e\gamma$ [Won94]. One main problem of a direct photon calculation in a QGP is the thermal particle distribution. Perturbative QCD dose not work at temperatures about 200 GeV when α_s becomes great.
However, in different calculations it is tried to include Bremsstrahlung effects and annihilation with additional scattering effects (AWS). For more detail see [Kar88, Kap91, Ste01, Arn01].

2.7.3 Thermal Direct Photons from a Hot Hadron Gas

A *hot hadron gas* (HHG) creates direct photons, too. A HHG is an alternative thermodynamic scenario for the fireball in a heavy-ion collision without phase transition. Furthermore, the HHG phase follows the QGP phase before the complete freeze out. The calculation of thermal photon spectra emitted from the HHG can be treated very similar to the QGP case [Kap91]. Three examples for relevant hadronic processes are given in Figure 2.6. Calculations of the emission rate from a hot hadronic gas are given in [Tur03] considering the hadronic decays:

- $\pi^{\pm}\rho^0 \rightarrow \pi^{\pm}\gamma$, Compton scattering shown in Figure 2.6(a),
- $\pi^+\pi^- \rightarrow \rho^0\gamma$, the annihilation process shown in Figure 2.6(b),
- $\rho^0 \rightarrow \pi^+\pi^-\gamma$, ρ^0 decay shown in Figure 2.6(c),
- $\omega \rightarrow \pi^0\gamma$, ω decay.

These can be compared to the rates for the QGP from [Aur98], for different temperatures [KB04] as can be seen in Figure 2.7. The agreement between the rates of a QGP and a HHG may be a coincidence at a certain temperature, but it cannot be ruled out especially given the current uncertainties of the calculations.

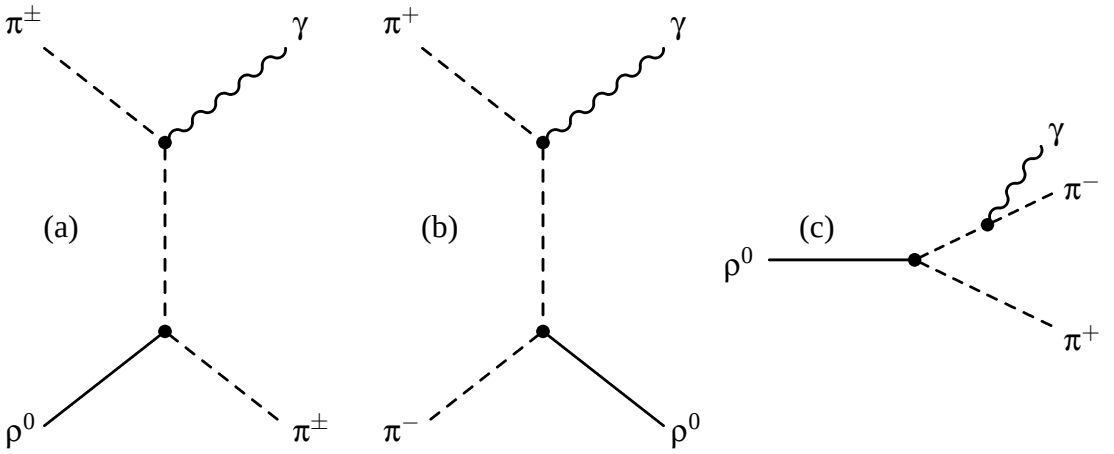

Figure 2.6: Examples of processes for the production of photons in a hadron gas: (a) $\pi^{\pm}\rho^0$ Compton scattering, (b) $\pi^+\pi^-$ annihilation, (c) ρ^0 decay.

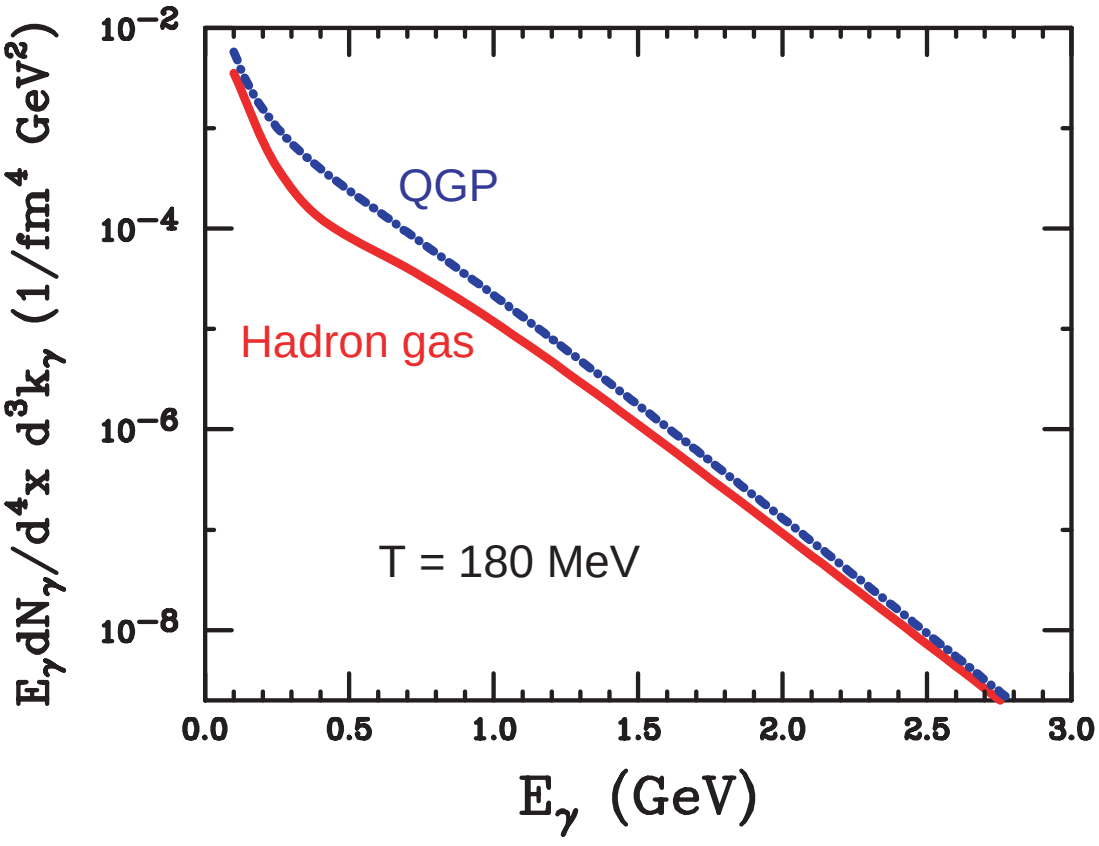

Figure 2.7: Comparison of the photon production rate from the quark-gluon plasma and the hadron gas at T = 180 MeV and for two quark flavors [Tur03].

3. PHENIX

The PHENIX Experiment is one of the two larger experiments at the Relativistic Heavy Ion Collider (RHIC).
PHENIX, the Pioneering High Energy Nuclear Interaction eXperiment, is an experiment for the investigation of high-energy collisions and has explored gold-gold, copper-copper, deuterium-gold and proton-proton collisions. PHENIX is specially designed to measure direct probes of the collisions such as electrons, muons, and photons. One of the primary goals of PHENIX is to discover and study a new state of matter, the so called *Quark-Gluon Plasma* (QGP).

3.1 The Relativistic Heavy Ion Collider

The two ring collider RHIC started operation in the year 2000 with colliding gold nuclei at a center of mass energy of $\sqrt{s_{NN}} = 130$ GeV. The two accelerator rings are denoted as *yellow* and *blue*, and accelerate the colliding particles in opposite direction. The ionisation and the initial acceleration process will be described for gold ions in the following. The different stages of the acceleration process are illustrated in Figure (3.1) together with an overview of RHIC.
Negatively charged gold ions are generated in a pulsed sputter source and injected into a Tandem-van-de-Graaff accelerator, where a fraction of their electrons is removed by so-called *stripping-foils*. The Tandem accelerates the ions to about 1 MeV/nucleon followed by further ionization. After that all Au^{+32} ions are selected and transfered to the AGS (Alternating Gradient Synchrotron) Booster.
The Booster accelerates the ions to 95 MeV/nucleon and strips them to Au^{+79} after four Booster cycles. After the energy of the ions has increased to 8.86 GeV/nucleon in the AGS the bunches of ions are injected into the two RHIC-rings, where they are accelerated to the colliding energy of up to 100 GeV/nucleon.
As the two rings of RHIC are operating independently and the beam injection has two Tandem-van-de-Graaff accelerators at its disposal, RHIC is ideal for studying asymmetric collisions. This was exploited in the third RHIC run in which deuterium-gold collisions were investigated. This kind of collisions are made to study the effects of cold nuclear matter. One part of this studies will be presented in this work.
The choice of deuterium instead of protons has only technical reasons. The mass/charge ratio of deuteron is similar to gold, which makes it possible to adopt the accelerator configurations for Au to that for deuterium. An overview of the first five beam times

of RHIC, along with amount of data recording time, for the different particle species is given in Table 3.1.

Run	species	particle energy [GeV/n]	time in physics	total delivered luminosity
Run-1	$Au^{+79}+Au^{+79}$	27.9	3 shifts	$< 0.001\ \mu b^{-1}$
2000	$Au^{+79}+Au^{+79}$	65.2	5.3 weeks	$20\ \mu b^{-1}$
Run-2	$Au^{+79}+Au^{+79}$	100.0	15.9 weeks	$258\ \mu b^{-1}$
2001/02	$Au^{+79}+Au^{+79}$	9.8	2 shifts	$0.4\ \mu b^{-1}$
	pol. p + p	100.0	8.3 weeks total	$1.4\ pb^{-1}$
Run-3	$d+Au^{+79}$	100.0	10.2 weeks	$73\ nb^{-1}$
2002/03	pol. p + p	100.0	9.0 weeks total	$5.5\ pb^{-1}$
Run-4	$Au^{+79}+Au^{+79}$	100.0	12.0 weeks	$3740\ \mu b^{-1}$
2003/04	$Au^{+79}+Au^{+79}$	31.2	9 days	$67\ \mu b^{-1}$
	pol. p + p	100.	6.1 weeks total	$7.1\ pb^{-1}$
Run-5	$Cu^{+29}+Cu^{+29}$	100.0	7.8 weeks	$42.1\ nb^{-1}$
20004/05	$Cu^{+29}+Cu^{+29}$	31.2	12 days	$1.5\ nb^{-1}$
	$Cu^{+29}+Cu^{+29}$	11.2	5 shifts	$0.02\ nb^{-1}$
	pol. p + p	100.0	9.4 weeks	$29.5\ pb^{-1}$
	pol. p + p	204.9	2 stores	$0.1\ pb^{-1}$

Table 3.1: Collected data by the PHENIX experiment during the first five RHIC beam periods [Fis06].

3.2 Other Experiments at RHIC

The loactions of the four experiments at RHIC are shown in Figure 3.1. In cost, size of construction and in the number of participating physicists and technicians, PHENIX and STAR[1] are larger than the BRAHMS[2] and PHOBOS[3] experiment. The PHENIX experiment will be described in the next section to give a more detailed overview.

[1] **S**olenoidal **T**racker **A**t **R**HIC
[2] **B**road **RA**nge **H**adron **M**agnetic **S**pectrometer
[3] PHOBOS is not an acronym.

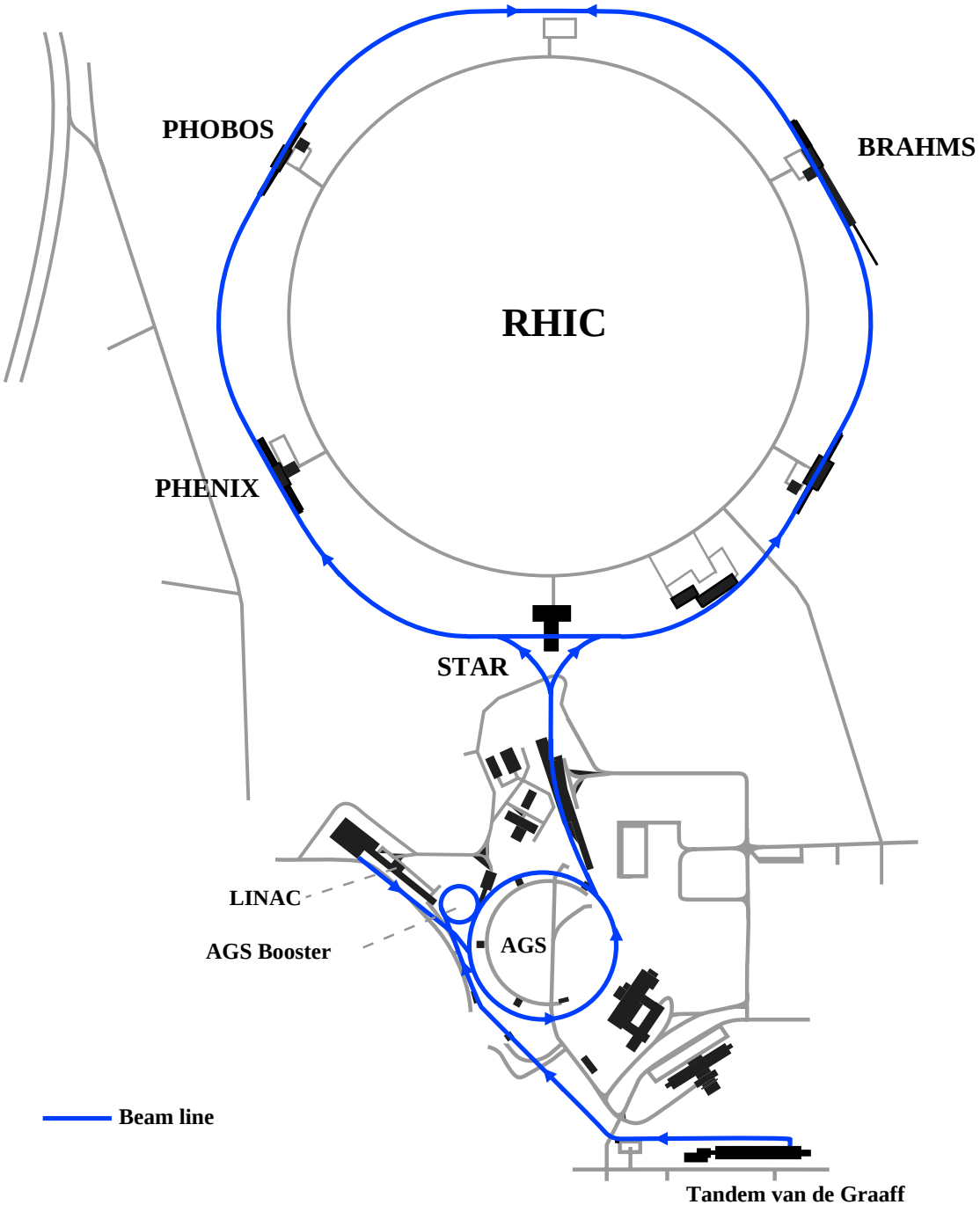

Figure 3.1: RHIC complex with its six interaction points and four experiments. The arrows indicate the direction of the ions at the different stages of acceleration [IKP06].

3.2.1 STAR

The STAR (see Figure (3.2)) experiment is specialized in reconstructing the tracks of thousands of particles produced in a heavy-ion collision at RHIC [Ack03]. One of the goals of the detector is to measure the hadron production and to study global observables to look for the signals of QGP.
The most important part of STAR is the Time Projection Chamber, with a diameter and length of 4 m, which tracks and identifies particles emerging from heavy-ion collisions. The tracking system is completed by a Silicon Vertex Detector (SVD) surrounding the beam pipe. The SVD improves the momentum resolution of the system and facilitates the reconstruction of secondary vertices of short-lived particles. Capability for photon and electron detection as well as energy measurement is added in a STAR upgrade by calorimeters surrounding the TPC: the Barrel Electromagnetic Calorimeter and the End-cap Electromagnetic Calorimeter.

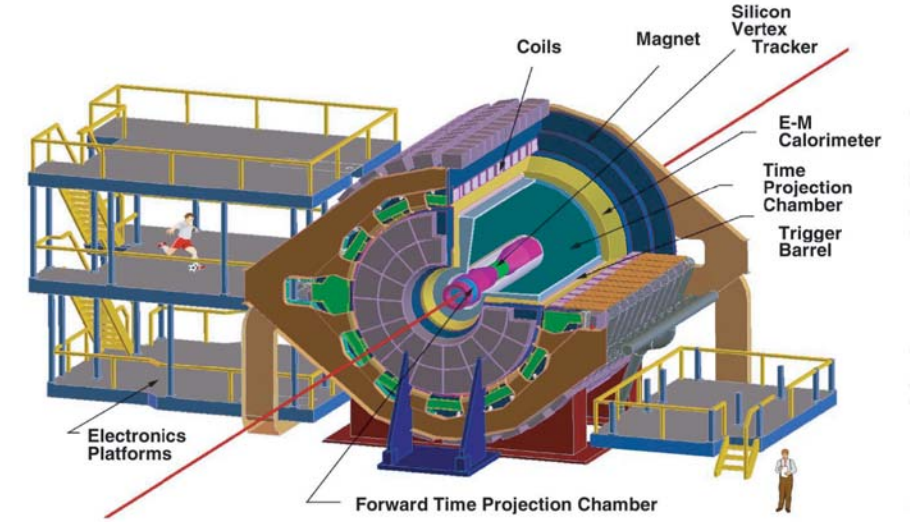

Figure 3.2: Perspective view of the STAR detector, with a cutaway for viewing inner detector systems [RHIC].

3.2.2 PHOBOS

PHOBOS consists of a large number of silicon detectors which surround the collision point (see Fig. 3.3), to measure the multiplicity of charged particles [Bac03]. Together with the spectrometry of charged particles near mid-rapidity ($0 \leq \eta \leq 2$) PHOBOS offers

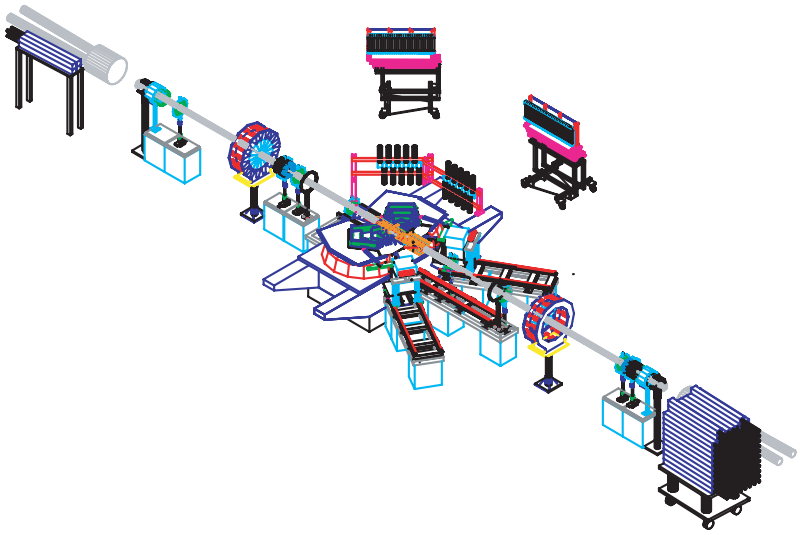

Figure 3.3: Perspective view of the PHOBOS detector [RHIC].

the possibility to study particle production in a broad kinematical region of the colliding nuclei.

3.2.3 BRAHMS

Like the PHOBOS experiment, BRAHMS [Ada03] covers a broad pseudo-rapidity range by means of two movable spectrometer arms (Figure 3.4). The spectrometers can be positioned at an angle ϑ with respect to the beam axis in the intervals $2.3^\circ \leq \vartheta \leq 90^\circ$ and $30^\circ \leq \vartheta \leq 95^\circ$, respectively.

3.3 Layout of PHENIX

PHENIX is designed to measure many different particles as photons, electrons, charged hadrons and muons at high rates in one experiment [Adc03]. A schematic view of the PHENIX experiment is given in Figure 3.5. The setup of the PHENIX experiment can be subdivided into the inner detectors close to the beam pipe and the four spectrometer arms, the east and west central arm at mid-rapidity, and the north and south muon arm at forward and backward rapidity, respectively

3.3.1 Inner Detectors and the ZDC

The inner detectors are the *Beam-Beam Counters* (BBC) and the *Multiplicity Vertex Detector* (MVD) [All03].

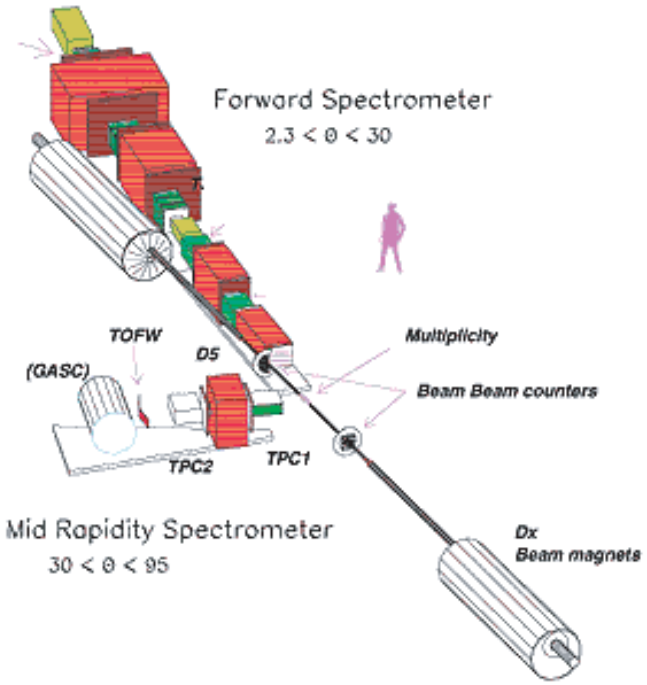

Figure 3.4: Perspective view of the BRAHMS detector [RHIC].

The BBC are located at both sides of the collision region. Their distance to the collision point is $z = \pm 144$ cm. They are able to measure the arrival time of particles in the pseudo-rapidity range $3.1 < |\eta| < 3.9$. Thus they can be used to determine the time and the location of the collision. Furthermore, the BBC plays a major role for the centrality determination and within the *Level-1* triggering system (see Sec. 4.1.1), to decide whether an inelastic collision occurred.
The MVD surrounds the collision point, covering the pseudo-rapidity range of $-2.64 < |\eta| < 2.64$ in full azimuth. The MVD consists of Si-Bands and Si-Pads and was constructed to measure the vertex position with high precision together with the particle distribution in pseudo-rapidity and azimuth. However the MVD never really worked.

Zero Degree Calorimeters (ZDCs) are positioned at each of the four RHIC experiments [Adl03a]. In PHENIX they are located at a distance of $z = \pm 18.25\,\mathrm{m}$ along the beam axis from the collision point between deflecting dipole magnets and are used as trigger detectors to help determine the vertex and centrality. That is possible because most of the ZDC detected particles are spectator neutrons, whose number depends on centrality. Due to the fact that every experiment uses the same type of ZDCs, the results can be compared by the global measurement category E_F which is the energy in forward direction.

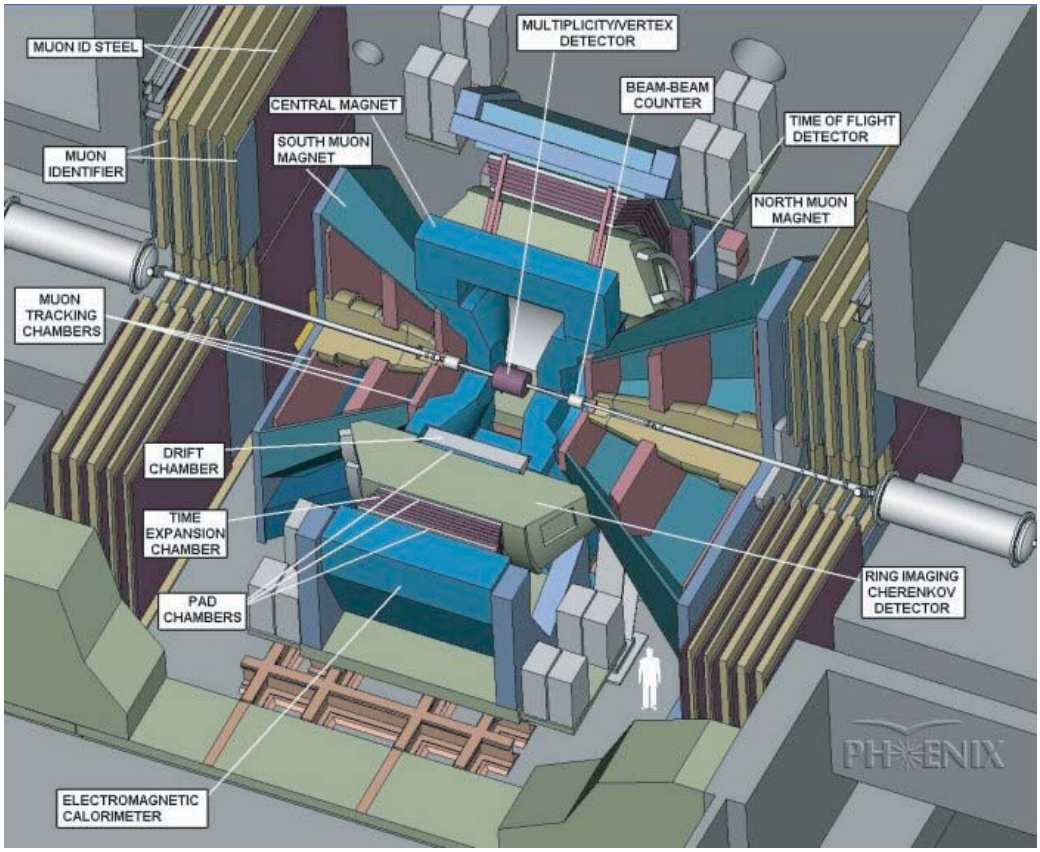

Figure 3.5: Perspective view of the PHENIX detector [IKP06].

3.3.2 Detectors of the Central Arms

The PHENIX detectors of the east and west arms are arranged concentric at different distances around the beam pipe. They cover the pseudo-rapidity range of approximately $|\eta| \lesssim 0.35$ and 90° in azimuth each and have the capacity to measure different particle species.

The *Central Magnet* (CM), weighing 421 tons, creates with its two concentric, independent coils a magnetic field in the interaction region around the beam axis with a maximum field integral of 1.15 Tm. The field drops strongly outward because it must not influence the measurement of the outer detectors. The magnetic field bends charged particles and helps to separate them by momentum. More information about the magnet is given in [Aro03].

Located at the edge of the magnetic field in both arms are the *Drift Chambers* (DC), with a radial distance to the beam axis of 2.02 m < r < 2.46 m. In addition to the

measurement of deflection of the charged particles in the magnetic field, they give a position information of charged particles.

Adjacent to the drift chambers is the first *Pad Chamber* (PC1) in both arms. It is read out via pads with a size of $8.45 \times 8.40\ \mathrm{mm}^2$. This first pad chamber and the drift chambers are used for particle tracking in the inner region of the central spectrometer directly behind the strong magnetic field.

Next to the PC1 there is the *Ring Imaging Cherenkov Detector* (RICH). It plays a major role for electron identification and has with the radial range of $2.50\ \mathrm{m} < r < 4.0\ \mathrm{m}$ in both arms a gas volume of $40\ \mathrm{m}^2$. Charged particles with velocities larger than the speed of light within the gas medium emit Cherenkov radiation in a light cone that falls as a ring on the RICH mirror system and is reflected onto photomultipliers. Due to different thresholds for electrons and pions to generate Cherenkov radiation, with CO_2 as radiator gas no pions are detected below $p = 4.65$ GeV/c and electrons below $p = 18$ MeV/c, the RICH provides good separation of the two particle species.

The next *Pad Chamber* (PC2) is located behind the RICH at $r = 4.19$ m in the west arm. The pads in this pad chamber have a size of $14.24 \times 13.55\ \mathrm{mm}^2$, which leads to the same resolution in η and ϕ for the PC2 as the PC1.

Instead of the PC2 there is a *Time Expansion Chamber* (TEC) in the east arm behind the RICH. Its four wire layers have a distance of $4.23\ \mathrm{m} < r < 4.88$ m to the beam axis. The TEC provides in addition to position information an energy loss measurement to separate electrons and charged pions with $250\ \mathrm{MeV}/c < p < 2.5\ \mathrm{GeV}/c$.

The third *Pad Chamber* (PC3) can be found at a radius $r = 4.90$ m, with a pad size of $16.7 \times 16.0\ \mathrm{mm}^2$. It has the same spacial resolution as PC1 and PC2. Its signal can be used to determine the fraction of charged particles in the EMCal as explaind in 4.2.1.

The *Time-Of-Flight* spectrometer (TOF), with its timing resolution of about 100 ps, allows to distinguish between kaons and protons up to $p = 4$ GeV/c and pion/kaon separation up to $p = 2.4$ GeV/c [Aiz03]. As the TOF is only installed in front of the two sectors of the lead-glass calorimeter, it covers only a small angular range of $\Delta\phi \approx 45^\circ$. Therefore the identification of charged particles is supported by a time-of-flight measurement of the larger acceptance lead-scintillator calorimeter with a nominal timing resolution of approximately 270 ps [Aph03].

The *Electromagnetic Calorimeter* (EMCal) completes the central arms. It consists of six sectors of a lead-scintillator sandwich calorimeter (PbSc) and two sectors of lead-glass Cherenkov calorimeter (PbGl), each sector covering 22.5° in azimuth. With a radial distance of more than 5 m it is the outermost detector part and is finely segmented for a good position and energy resolution. The EMCal will be introduced in Section 3.4.

3.3.3 The Muon Spectrometer

The Muon Arms spectrometers (see Figure 3.6) allow the measurement of J/Ψ, Ψ', and ϒ through their decay into muon pairs as well as the Drell-Yan process. It detects and tracks muons in the forward pseudo rapidity range $1.2 < |\eta| < 2.4$ and covers the full azimutal angle. The complete PHENIX muon arms subsystem is made up of the *Muon Identifier* (MuTR) and the *Muon Tracker* (MuID) [Aki03].

The *Muon Trackers* (MuTR) are composed of three so-called stations, tracking chambers with cathode-strip readout. It is implemented in the conical shaped *Muon Magnets* with radial field, to track charged particles with a position resolution of approximately 100 μm and allows the separation of the heavy mesons like J/Ψ as well ρ/ω and ϕ. The largest background in the measurement of muons is formed by mis-identified pions and by muons from pion decays.

The *Muon Identifier* (MuID) is located behind the muon magnets. Consisting of six steel armored absorber plates, which are chosen in a thickness, that only muons with an energy above 2.9 GeV penetrate the MuID completely. The combination of MuID and different absorbers leads to a π/μ separation of $2 \cdot 10^{-4}$ to $3.9 \cdot 10^{-3}$ in the momentum region 2 GeV/$c < p <$ 10 GeV/c.

3.4 The Electromagnetic Calorimeter

The Electromagnetic Calorimeter (EMCal) is the major subsystem of the detector for the analysis presented in this thesis. Its two different detector types, two sectors lead-glass Cherenkov calorimeter (PbGl) and six sectors lead-scintillator sandwich calorimeter (PbSc), are designed to measure the energy and position of photons and electrons at midrapidity ($|\eta| < 0.35$) over an azimuthal angle of π (see Figure 3.6) and to provide with their different systematics a possibility for internal cross-checks of each EMCal measurement.

3.4.1 Mode of Operation

Because of the different ways of interaction typically a distinction is drawn between electromagnetic and hadronic showers to describe the detector properties because of their different channels of interaction.

Highly energetic photons hitting the EMCal interact mainly via electron-positron pair production. Other processes such as photoelectric effect and Compton scattering play only a minor role in this energy regime. The produced electrons and positrons subsequently lose their energy in the electric field of the atomic nuclei of the detector medium by radiating bremsstrahlung. These photons can again convert into e^+e^- pairs. The result is an **electromagnetic shower**, which aborts when the individual energy of the particles falls below the critical energy E_c, where the energy loss via ionization begins to dominate over the energy loss by bremsstrahlung.
Except for the first step, electrons and positrons form an electromagnetic shower in the same way as photons do. The depth of the shower maximum depends on the initial energy E_0 of the incoming particle and can be expressed in units of the radiation length [Eid04]:

$$\frac{X_{\max}}{X_0} \approx \ln\left(\frac{E_0}{E_c}\right) + t \tag{3.1}$$

($t = 0.5$ for photons, $t = -0.5$ for electrons),

where X_0 is the radiation length, the distance where the energy of an electron decreases by a factor of e. The lateral extension of an electromagnetic shower is determined by multiple scattering of the shower particles. It is characterized by the Molière radius:

$$R_M \approx \frac{21\,\mathrm{MeV}\cdot X_0}{E_c}. \tag{3.2}$$

So-called **hadronic showers** originate from strongly interacting particles, such as pions and protons. Its characteristic quantity is the nuclear interaction length λ, the distance where 63% of the hadrons suffer an inelastic interaction and form further hadrons, mostly pions. Charged hadrons that do not participate in an inelastic reaction and deposit only a small fraction of their energy by ionization and possibly Cherenkov radiation are called *Minimum Ionizing Particles* (MIPs). Their energy loss is given by the Bethe-Bloch equation (see e.g. [Eid04]). It is constant over a wide energy range leading to the formation of the characteristic MIP peak.
The **Cherenkov radiation** can be an accessory way to detect particle properties e.g. used in the PbGl. Charged particles with a velocity v larger than the speed of light within a

Index of refraction	$\bar{n}$	1.648
Radiation length	X_0	2.8 cm
Molière radius	R_M	3.68 cm
Interaction length	λ	38 cm
Critical energy	E_c	16 MeV

Table 3.2: Physical parameters of the lead-glass TF1 [Aph03].

medium $v > c/n$, where n is the index of refraction of the medium, emit light. This phenomenom is known as Cherenkov radiation and emits light with an angle to the incident direction of the particle of:

$$\cos\theta_{Ch} = \frac{c}{vn}. \tag{3.3}$$

Thus the measurement of the angle of the Cherenkov cone allows the determination of the velocity of a particle. This fact could also be used for particle and energy detection.

3.4.2 The Lead-Glass Detector

The lead-glass detector in PHENIX is composed of the LEDA[4] detector from the WA98 experiment at CERN where direct photons were measured successfully for the first time in heavy ion collisions. It has been reassembled to be installed as two sectors at PHENIX as can be seen in Figure 3.6.

The 9216 single detector modules of the PbGl consist of lead-glass type TF1 which properties are summarized in Table 3.2 and are individually read out by *FEU-84* photomultipliers [Neu95]. Each lead-glass sector consists of 16×12 supermodules containing of 6×4 modules each. Each supermodul forms a self contained detector with its own reference system (see Figure 3.7), which allows the easy reassembly of the detector in a different geometry and without a completely new calibration. This reference system consists of three light emitting diodes at the front end of each super module and is chosen to emulate different aspects of the spectral and temporal behavior of a highly energetic photon that showers in the detector. For a more detailed description of the lead-glass and the reference system see [Sch94a].

3.4.3 The Lead-Scintillator Detector

The Lead-Scintillator Detector is a sandwich calorimeter consisting of alternating layers of lead absorber and scintillator plates, read out by photomultipliers connected optical

[4] **LE**ad glass **D**etector **A**rray

Active sampling cells		66
Scintillator		0.4 cm Polystyrene (1.5% PT/0.01% POPOP)
Absorber		0.15 cm Pb
Radiation length	X_0	2.02 cm
Interaction length	λ	44.2 cm
Cell size		0.56 cm (0.277 X_0)
Active depth		37.5 cm (18 X_0)

Table 3.3: Physical parameters of the lead-scintillator sandwich calorimeter [Aph03].

with wavelength-shifting fibers. Each 2×2 array of the 15552 single towers is combined to modules. 6×6 module parts build a supermodul (see Figure 3.8) where 6×3 supermodules build each PbSc sector. Four sectors are located in the west arm and two sectors in the east arm of the PHENIX experiment positioned directly behind the PC3 at a radial distance of 5.10 m (see Figure 3.6). The physical detector parameters of this sandwich structure are summarized in Table 3.3. The hadronic interaction length is higher compared to the PbGl. That provides a better energy measurement for hadrons, as it also measures low energy shower particles via scintillation that would not emit Cherenkov light. This is advantageous for the determination of the total transverse energy E_T, but it means a larger background contribution from hadrons when measuring photons.

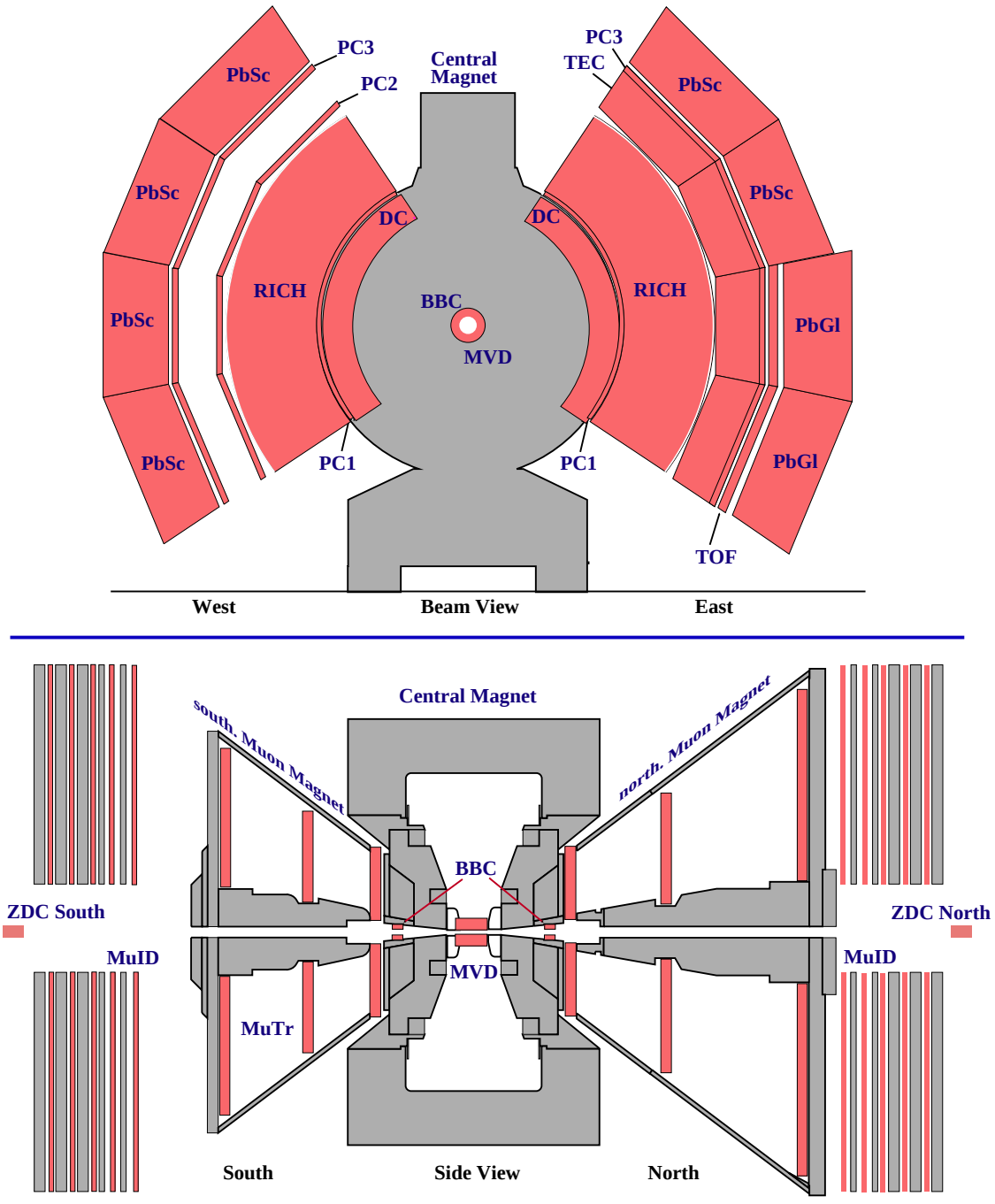

Figure 3.6: The PHENIX detector in 2003 [IKP06].

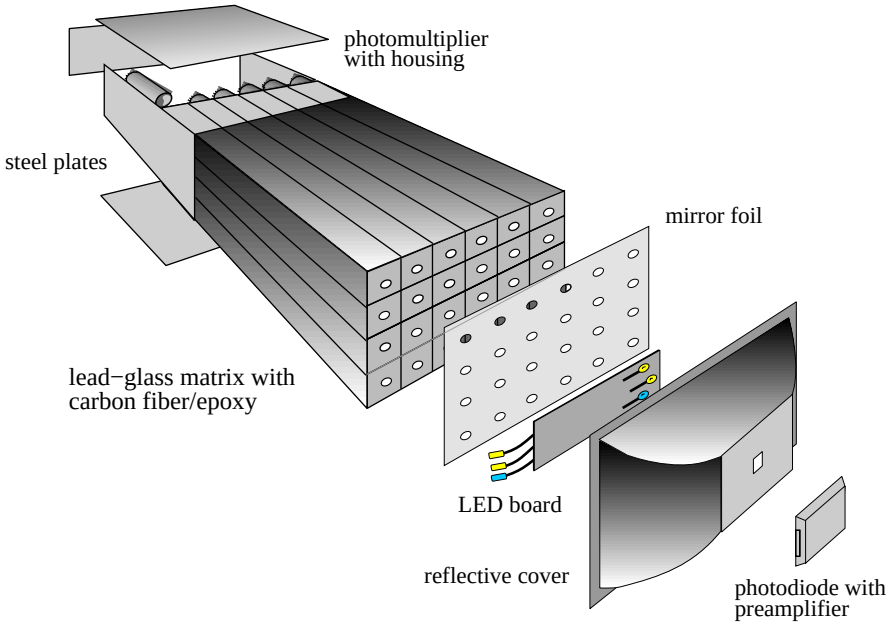

Figure 3.7: Exploded view of a lead-glass supermodule including the reference system [IKP06].

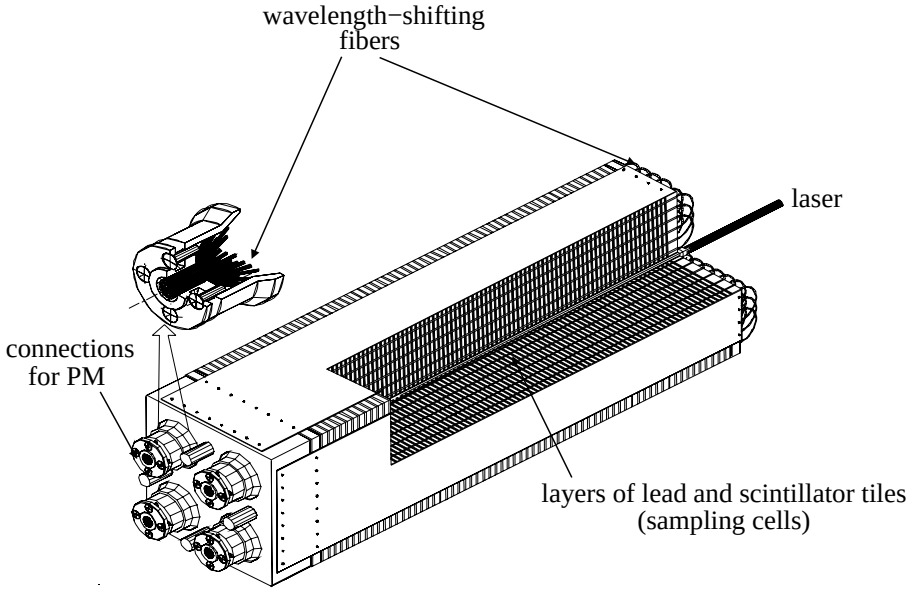

Figure 3.8: Interior view of one PbSc module, consisting of four towers [IKP06].

4. Measurement of Direct Photons

As discussed in Chapter 2.7 direct photons are well suited to study different stages of a heavy-ion collision, as they are produced throughout all phases of the reaction and can escape without strong interactions. In this chapter the measurement of direct photons in d + Au collisions at RHIC is presented, which allows to explore the production of direct photons in heavy-ion collisions in a transverse momentum region where hard scattering is the dominant source of particle production. A comparison with results from p + p and Au + Au collisions is given.

4.1 Data Selection and Processing

The Event Builder assembles the raw data from the detectors in the PHENIX Raw Data Format (PRDF). The raw collection of events are so called *runs*. They are recorded over a certain period of time (usually 30 minutes up to 2 hours) and get consecutive numbers. Within one run the global settings of the data acquisition, e.g. the prescale factors of the triggers, and of the detectors remain unchanged. This raw data selections have to be converted into quantities with more physical meaning. Two different types of event selections have been analysed: minimum bias events, which are only biased by the limited BBC efficiency, and high-p_{T} events specially selected because they contain to at least one highly energetic photon. In addition to the trigger selection, it is required that the vertex z of a given event lies within the range -30 cm $\leq z \leq$ 30 cm, in order to exclude regions that are shadowed by the pole tips of the central magnet and to minimize the background of scattered particles [KB04]. The EMCal and PC3 multiplicity, as well as the BBC response, is monitored during the data analysis to meet certain quality criteria of the runs that are used for analysis. All runs showing a large deviation from the average behavior are excluded during the following analysis passes. A table of all analyzed runs can be found in Appendix B.

4.1.1 Minimum Bias and High-p_{T} Events

The minimum bias trigger condition in d+Au requires a signal from at least one photomultiplier of each BBC. This condition allows the measurement of 88% of the total geometrical d+Au cross section. Due to the limited bandwidth of the PHENIX data acquisition, usually only a fraction of all minimum bias events is recorded. This fraction is determined by the prescale factor, which is specified at the beginning of a run for each

trigger.
Because of the different production processes for direct photons in different regions of transverse momentum, it is important to cover a broad p_{T} range. This is only possible with the help of specialized triggers for high-p_{T} photons in d+Au in order to increase the number of high-p_{T} events in comparison to minimum bias. The following will concentrate on the specifics when analyzing data with different trigger conditions: It is important to pay attention to several points when combining data with two different triggers. The normalization to the number of unbiased events has to be taken into account as well as the events rejected by the trigger. Not less important is the calculation of the particle yields which has to account for the sensitivity or efficiency of the trigger to the respective particle species. These can be different compared to minimum bias triggers and depend on the energy of the measured particle, because of the effective trigger thresholds.

The typical way to calculate the number of underlying minimum bias events $\tilde{N}_{\mathrm{evt}}^{\mathrm{mb}}$ for a given photon trigger is, to start with a sample of minimum bias events and determine the fraction of events for which the trigger condition, including the prescale condition, is satisfied:

$$\varepsilon_{\mathrm{evt}}^{\mathrm{trig}} = \frac{N_{\mathrm{evt}}^{\mathrm{mb}\wedge\mathrm{trig}}}{N_{\mathrm{evt}}^{\mathrm{mb}}}. \tag{4.1}$$

The number of underlying minimum bias events is then given by correcting the number of measured triggered events for the total rejection factor $(1/\varepsilon_{\mathrm{evt}}^{\mathrm{trig}})$ of the trigger:

$$\tilde{N}_{\mathrm{evt}}^{\mathrm{mb}} = \frac{1}{\varepsilon_{\mathrm{evt}}^{\mathrm{trig}}} \cdot N_{\mathrm{evt}}^{\mathrm{trig}}. \tag{4.2}$$

Most of the data used in the analysis of d+Au collisions come from specially filtered runs in which only events satisfying the so called *ERT gamma1* trigger condition are recovered. In the analysed runs the ERT 4x4 is used. This trigger is sensitive to the sum of 4x4 EMCal towers, so called 4x4 trigger tiles which overlap to avoid inefficiencies at their edges. The trigger threshold is 2.1 GeV for the gamma1 trigger. The scaling factor for each event is determined from the PHENIX database, where the number of trigger counts for each run is recorded. The rejection power of the trigger for a given run is simply given by the comparison of the raw trigger counts for the gamma1 $(N_{\mathrm{raw}}^{\mathrm{G1}})$ and for the minimum bias $(N_{\mathrm{raw}}^{\mathrm{BBC}})$ condition given by the BBC, leading to the effective rejection power of the trigger. Additionally, the scaledown S^{L1} of the gamma1 trigger has to be considered which scales the ERT-triggered high-p_{T} events to the underlying minimum bias events:

$$\varepsilon_{\mathrm{evt}}^{\mathrm{trig}} = \frac{N_{\mathrm{raw}}^{\mathrm{G1}}}{N_{\mathrm{raw}}^{\mathrm{BBC}}} \cdot \frac{1}{S^{\mathrm{L1}}+1}. \tag{4.3}$$

To combine minimum bias and high-p_T triggered data it is important to consider the difference in the bias on the event by the trigger devices of the BBC for minimum bias and EMCal with ERT for high-p_T.
A comparison of the minimum bias triggered data and the ERT triggered data like Equation (4.3) is given in Figure (4.1). The predefined analog threshold of the ERT dose not define a sharp energy cut off at the nominal value of 2.1 GeV, what leads to an slow increase of the trigger efficiency for increasing p_T. This reflects the deviation of the hit energy determination for the ERT trigger (see [KB04]). The energy-dependent trigger efficiency would reach a plateau at the value of one, if the detector areas considered in the analysis is the same as in the trigger. This is not the case for the ERT triggered data because the maps of bad and dead modules are not the same for measurement and ERT trigger, wich can be seen in Appendix C.
As for the ERT trigger more bad modules are extracted, the EMCal acceptance is lower

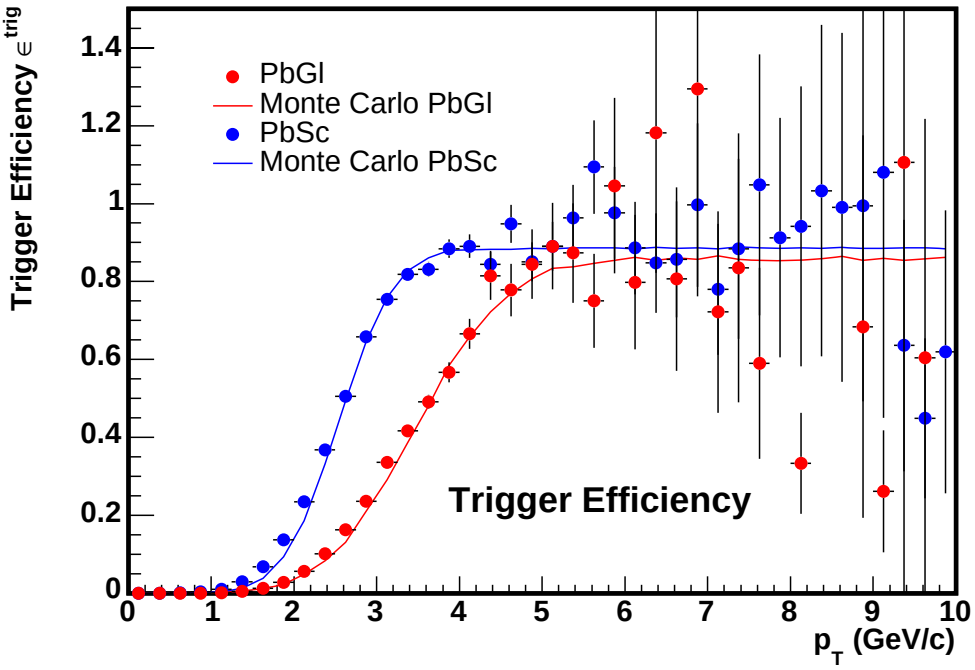

Figure 4.1: Trigger turn-on or trigger efficiency (ε^{trig}) for PbGl and PbSc determined by the comparison of minimum bias and high-p_T data in d + Au collisions together with the parameterization used in the Monte Carlo simulation to calculate the trigger efficiency. Because of different detector areas, used for the trigger and the analysis, the efficiency does not reach the value of one.

for the ERT-triggered high-p_T data as for the minimum bias triggered lower p_T data.

Thus the trigger efficiency is limited by the geometrical limit $\varepsilon_{\text{geo}}^{\text{trig}}$ determined by the active modules of the EMCal for the ERT trigger ($N_{\text{module}}^{\text{ERT}}$) compared to the total acceptance of the detector used for the minimum bias data ($N_{\text{module}}^{\text{minbias}}$):

$$\varepsilon_{\text{geo}}^{\text{trig}} = \frac{N_{\text{module}}^{\text{ERT}}}{N_{\text{module}}^{\text{minbias}}}, \tag{4.4}$$

where $N_{\text{module}}^{\text{ERT}}$ is given by the overlap of the maps shown in Figure C.1 and C.2.
To simulate the p_{T} dependence of the trigger efficiency, a Monte Carlo method is used. Though the trigger efficiency is well described over a broad p_{T} range as can be seen in Figure 4.1 the ERT-triggered data are only used above $p_{\text{T}}^{\text{trans}} = 5\,\text{GeV/c}$, where the efficiency approaches the geometrical limit. Since the minimum bias data in this p_{T} region add little statistics to the measurement, a sharp transition is used for the combined result of the photon yield in $\text{d}+\text{Au}$:

$$\frac{1}{N_{\text{evt}}}\frac{\text{d}N_{\text{raw}}}{\text{d}p_{\text{T}}} = \begin{cases} \frac{1}{N_{\text{evt}}^{\text{minbias}}}\frac{\text{d}N_{\text{raw}}^{\text{minbias}}}{\text{d}p_{\text{T}}} & \text{for } p_{\text{T}} < 5\,\text{GeV}/c, \\ \frac{1}{\varepsilon^{\text{trig}}}\frac{1}{\tilde{N}_{\text{evt}}^{\text{minbias}}}\frac{\text{d}N_{\text{raw}}^{\text{ERT}}}{\text{d}p_{\text{T}}} & \text{for } p_{\text{T}} \geq 5\,\text{GeV/c}. \end{cases} \tag{4.5}$$

4.1.2 Data Summary Tape

The structure where the data information of each detector is saved is named **D**ata **S**ummary **T**ape and contains information like particle tracks and momenta. It is the first conversion step of the raw detector information. The information of the DST is further condensed in *micro*DSTs, which is basically a reduction of the data on a requested focus. In the last step of specialization are the so called *nano*DSTs, where data important for different types of analysis are split into different files. This work bases on nanoDSTs for the EMCal. A short overview of the production of cluster tracks will be given and can be divided into the following steps as explained in [KB04]:

- Find a cluster, a group of adjacent towers each with an energy above the noise threshold.
- Find the local maxima of the cluster. A local maximum is a module above the peak threshold, with the maximum amplitude in the 3×3 region surrounding it.
- If more than one local maximum is found, split the cluster according to amplitude and positions of the maxima.

		PbGl	PbSc
PID 0	No cuts		
PID 1	Energy cut (d + Au)	0.2 GeV	0.2 GeV
PID 2	Shower shape cut	$\max(D_{\mathrm{corr},x}, D_{\mathrm{corr},y}) < D_{\mathrm{cut}}(\theta)$	$\chi^2 < 3$
PID 3	energy and shape cut		

Table 4.1: The parameters of the different cuts used during the analysis.

- Calculate the first and second moments of the clusters as basis for the determination of the impact position.
- Compare the shape of the cluster with the expectation for an electromagnetic shower for particle identification. This so called χ^2 method is described below.
- Compute and correct the total energy for the cluster.

To facilitate the measurement of photons within the EMCal, certain variables for their identification are also computed and associated with the cluster. The main tool to suppress the background from hadrons is a cut on the shower shape, as an hadronic shower usually spreads over more modules than an electromagnetic shower, whose lateral extension is given by Equation (3.2).

In this work four different PID criteria are used as can be seen in Table 4.1. In former analyses a time-of-flight (TOF) cut was used. In the DST the arrival time for the tower with the largest energy within the cluster is stored and can be compared to the calculated time-of-flight for a photon. However, in this analysis only a energy cut is used, which is seen to be essentially equivalent to a lose TOF cut. The main reduction of the background from hadrons comes from a cut on the shower shape. Since electromagnetic and hadronic showers differ in their width and spread over an increasing number of modules with increasing incident angle θ, the cut on the lateral extesion of the shower is chosen as a function of angle, the so called *dispersions-cut*, as given by Equation (4.6) for PbGl.

$$D_{\mathrm{cut}}(\theta) \quad = \quad 0.27 - 0.145 \cdot \theta + 0.00218 \cdot \theta^2, \text{ with } \theta \text{ in degrees.} \tag{4.6}$$

The shower shape cut for PbSc bases on a comparison of the deposited energy E_i^{meas} in each module of the measured cluster to the expectation for a cluster formed by an electromagnetic shower of the same cluster energy. The electromagnetic character of a cluster with N towers can be defined as:

$$\chi^2 = \frac{1}{N}\sum_{i=1}^{N}\frac{\left(E_i^{\text{ideal}} - E_i^{\text{meas}}\right)^2}{\sigma_i^2}, \tag{4.7}$$

where σ_i is the variance, which provides the dependence of the fluctuations on the energy and angle of incidence and on losses to the total energy due to the threshold used in the clustering. During the analysis of the PbSc data only clusters with a value of $\chi^2 < 3$ are considered as electromagnetic showers. For more details see [KB00].

The measured energy E is not linearly related to the energy of the incoming particle E_0 because a shower might not deposit all of its energy in the calorimeter and due to light absorption. To correct this effect the *non-linearity* of the PbGl and the PbSc has been determined in electron test beam measurements and by simulation studies [Aph03].

The next processing level are the microDSTs. One main difference to DSTs is a reduction of included information. The microDSTs can also be rewritten with substituted information. This is done using so called *afterburners* that can be applied to a micro DST for correction not known during the DST production (see [Chi02]).

Basis of this thesis are nanoDSTs produced for the centrality dependent measurement of neutral pions in d+Au [Bat03]. At this level different corrections of the energy are applied to account for miscalibrations during the DST or microDST production. These corrections can be subdivided into two types:

- absolute energy calibration
- exclusion of bad modules

The invariant mass measurement of π^0s is not only important to calculate the direct photon background but furthermore the absolute energy scale is in principle fixed by the measurement of the π^0 peak position and the comparison with the expectation from the π^0 efficiency simulation, which is also needed for the correction of the π^0 spectra. The peak position correction itself is described here. To avoid shifts in the reconstructed π^0 mass due to the overlap of clusters in events with large multiplicity, the empirical energy correction for the PbGl in the analysis of the $\mathrm{d}+\mathrm{Au}$ cluster data is based on the π^0 peak position measured in $\mathrm{p}+\mathrm{p}$ collisions during the same beam time. The functional form is given by:

$$E_{\text{corr}} = E\left(a_1 + a_2 \cdot e^{a_3 \cdot E}\right), \tag{4.8}$$

d + Au			
E0	1.02	0.03	-0.863
E1	1.	0.	0.
E2	0.98	0.07	-0.978
E3	0.99	0.06	-0.877
W0	0.985	0.05	-0.834
W1	0.989	0.04	-0.709
W2	0.98	0.05	-0.921
W3	1.	0.03	-0.359
	a_1	a_2	a_3

Table 4.2: Parameters for the linearity correction of the energy as given by Equation (4.8).

with the parameters summarized in Table 4.2.

The exclusion of bad modules depends on quality criteria for the clusters, to prohibit distortions of the energy measurement of a hit. This is of particular importance when detecting single photons.
Modules without any energy signal, denoted *dead*, within a cluster lead to a measured energy that is too low. Most of the dead modules are due to faulty photomultipliers, which produce either no signal or are switched off because they show a constantly large energy signal independent of a physics input. In addition, the edge modules of the detector are considered to have a dead neighbor to exclude clusters that suffer from leakage at the calorimeter edge.
It is also important to exclude modules that only sporadically contribute in a wrong way to the signal. Especially at higher energies, where the number of produced photons is small, one single *warm* module can easily distort the measured spectrum. For this reason the search for bad modules is also performed in different energy ranges by looking at the frequency at which a given module is the main contributor to a cluster with an energy falling into this region (see Appendix C).

4.2 Direct-Photon Analysis via the Cocktail Method

One of the main problems in the measurement of direct photons is to separate the signal from the contribution of radiative decays (mainly π^0,$\eta \rightarrow \gamma\gamma$) in the inclusive photon spectrum. For this analysis the cocktail method is used, where the direct photon signal is calculated as a fraction of the inclusive photon spectrum. The measured sample of

photon-like clusters is contaminated by charged hadrons, neutrons and anti-neutrons, which are removed on a statistical basis. Also photon conversion must be taken into account and corrected as well as shower merging effects of the π^0 spectra. After applying reconstruction efficiency and acceptance corrections, the γ/π^0 ratio is calculated. The background from hadronic decays is simulated with a fast Monte-Carlo which takes the measured π^0 spectrum as input. The photon excess is determined by comparing the measured γ/π^0 to the simulated γ/π^0 ratio. From this excess the direct photon invariant yield can be extracted (see also [Zau05]):

$$\left.\frac{1}{2\pi p_{\mathrm{T}} N_{\mathrm{in}}}\frac{\mathrm{d}^2 N_\gamma}{\mathrm{d}p_{\mathrm{T}}\mathrm{d}y}\right|_{\mathrm{direct}} = \left(1-\frac{\left.N^\gamma/N^{\pi^0}\right|_{\mathrm{bkgd}}}{\left.N^\gamma/N^{\pi^0}\right|_{\mathrm{meas}}}\right)\cdot\left.\frac{1}{2\pi p_{\mathrm{T}} N_{\mathrm{in}}}\frac{\mathrm{d}^2 N_\gamma}{\mathrm{d}p_{\mathrm{T}}\mathrm{d}y}\right|_{\mathrm{incl}}, \qquad (4.9)$$

where $\left.\frac{1}{2\pi p_{\mathrm{T}} N_{\mathrm{in}}}\frac{\mathrm{d}^2 N_\gamma}{\mathrm{d}p_{\mathrm{T}}\mathrm{d}y}\right|_{\mathrm{incl}}$ is the inclusive photon yield and $\left.N^\gamma/N^{\pi^0}\right|_{\mathrm{bkgd}}$ and $\left.N^\gamma/N^{\pi^0}\right|_{\mathrm{meas}}$ are γ/π^0 spectra which bases on a particle decay simulation and π^0 measurement, respectively. This will be explained in the following paragraph.

4.2.1 Inclusive Photons

The raw inclusive photon yield is contaminated by mis-identified charged particles and neutral hadrons, which make additional corrections necessary. The fully corrected inclusive photon spectrum is given by the equation:

$$\left.\frac{1}{2\pi p_{\mathrm{T}} N_{\mathrm{in}}}\frac{\mathrm{d}^2 N_\gamma}{\mathrm{d}p_{\mathrm{T}}\mathrm{d}y}\right|_{\mathrm{incl}} = \frac{1}{2\pi p_{\mathrm{T}} N_{\mathrm{in}}}\cdot\frac{(1-X_{\mathrm{n\bar{n}}})\cdot(1-X_{\mathrm{ch}})}{\varepsilon_\gamma\cdot a_\gamma\cdot c_{\mathrm{conv}}}\cdot\frac{\Delta N_{\mathrm{cluster}}}{\Delta p_{\mathrm{T}}\Delta y}, \qquad (4.10)$$

where a_γ is the acceptance and ε_γ the efficiency correction. The factors X_{ch} and $X_{\mathrm{n\bar{n}}}$ are the contributions of charged particles and neutral hadrons to the raw yield of photon-like clusters measured with the EMCal, $\frac{\Delta N_{\mathrm{cluster}}}{\Delta p_{\mathrm{T}}\Delta y}$. The determination of the correction factors will be discussed in the following.
Incorporated into the measurement of the raw inclusive photon spectrum is an event sample enriched with highly energetic photons, the LVL1-triggered data. This data for the photon measurement is combined with the minimum bias data above $p_{\mathrm{T}} = 5\,\mathrm{GeV}/c$.

Detector Acceptance

The geometric acceptance of a detector describes which fraction of particles, in this case photons, will hit the active detector surface, compared to the number of particles emitted

into the respective phase-space interval. The phase-space interval is usually chosen as a rapidity interval Δy and for full azimuthal coverage ($\Delta\phi = 2\pi$).
For single photons the acceptance is basically given as the fraction of phase-space covered by the detector in this interval. Within a rapidity interval of $\Delta y = 0.9$ the PbSc covers 21.5% of the phase-space and the PbGl 6.3%. This has been determined using a fast Monte Carlo simulation [Rey03] of the PHENIX setup, which is also used for the efficiency calculation and in the background determination for the direct photon measurement. The Monte Carlo method is called *fast*, because not the whole shower is simulated. To improve the calculating performance only the center of gravty of the shower is determind and smeared in its position and energy.
The difference of the acceptance between PbSc and PbGl shown in Figure 4.2 determined by the number of sectors employed for the analysis, as well as by dead and bad modules. The small p_T dependence comes from leakage effects of showers at the detector border. A high p_T shower has a bigger probability to leak out of the detector as it has on average a higher energy and thus a higher length and width.

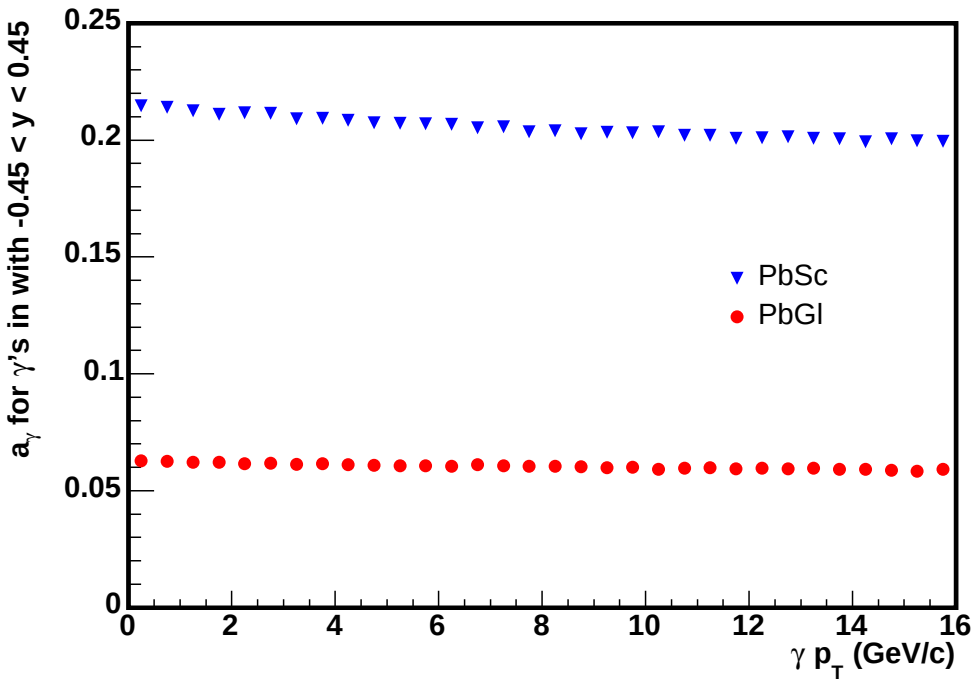

Figure 4.2: Geometrical acceptance of PbGl and PbSc calculated with a fast Monte Carlo method.

Detector Efficiency

The goal of the efficiency determination for a detector is to correct for all detector specific effects and analysis cuts, which cause the differences of the measured spectrum $f(p_{\mathrm{T_{out}}})$ in relation to the true input spectrum $f(p_{\mathrm{T_{in}}})$ of particles hitting the detector. This leads to the general definition of the efficiency:

$$\varepsilon(p_{\mathrm{T}}) \quad = \quad \frac{f(p_{\mathrm{T_{out}}})}{f(p_{\mathrm{T_{in}}})}. \tag{4.11}$$

The efficiency is not limited to $\varepsilon < 1$. The output spectrum and thereby the efficiency is influenced e.g. by the position and energy resolution of the detector but also by the event multiplicity, which determines the probability for EMCal clusters to overlap. In addition, the efficiency depends on the various PID and analysis cuts. Just like the acceptance, the efficiency for this analysis is calculated via a Monte Carlo simulation. The determination of the efficiency via a Monte Carlo simulation yields good results for analyses in a relativly low multiplicity environment like in $\mathrm{d}+\mathrm{Au}$ or $\mathrm{p}+\mathrm{p}$ collisions, where the effects of cluster overlap are negligible. Alternativ calculation methods, like the embedding method [KB04], need much more CPU-time and disc space. The simulation code used for the efficiency determination also incorporates the acceptance calculation and the determination of the decay background for the direct-photon analysis. Photons are generated within the fast Monte Carlo with the following characteristics:

- Flat transverse momentum distribution $0 < p_{\mathrm{T}} \leq 32\,\mathrm{GeV}/c$,
- Uniform vertex distribution $|z_{\mathrm{vtx}}| \leq 30\,\mathrm{cm}$,
- Gaussian rapidity distribution around zero in the interval $|y| \leq 0.45$ and width $\sigma_{\mathrm{rap}} = 3$,

The energy and position of the photons are smeared around their nominal energy and position resolution. In the Monte Carlo simulation the same cuts need to be applied as for the real data. For this purpose the effect of the shower shape cut on single photons is parameterized based on the comparison of the photon yields for different PIDs. Additionally there is implemented an energy threshold of 0.2 GeV similar to PID 1 in the simulation.

The cut on bad modules must also be implemented in the fast Monte Carlo. As discussed above, this cut depends on the module with the largest energy deposit within the cluster, hence on the depth of the maximum energy deposit of the shower. In the fast Monte Carlo only the impact position of a photon on the detector surface (x,y) is known.

For a more accurate description of the bad module cut this can be corrected with a parameterization obtained from real data by comparing the reconstructed impact position and the position of the tower with maximum energy deposit [Rey05]:

$$\begin{aligned} r_{\text{shift}} &= 0.07\,\text{cm} \cdot \theta \cdot (0.32 + 0.51 \cdot \log(1+E) \\ &\quad + 0.45 \cdot \log^2(1+E)), \end{aligned} \tag{4.12}$$

$$x_{\text{shifted}} = x + r_{\text{shift}} \cdot \cos\varphi, \tag{4.13}$$

$$y_{\text{shifted}} = y + r_{\text{shift}} \cdot \sin\varphi,$$

where θ is the impact angle in degrees with respect to a perpendicular to the detector surface, and E is the energy of the photon in GeV. The corrected position determines the position of the tower which is compared to the list of bad modules also used during the analysis of the real data (see Appendix C).

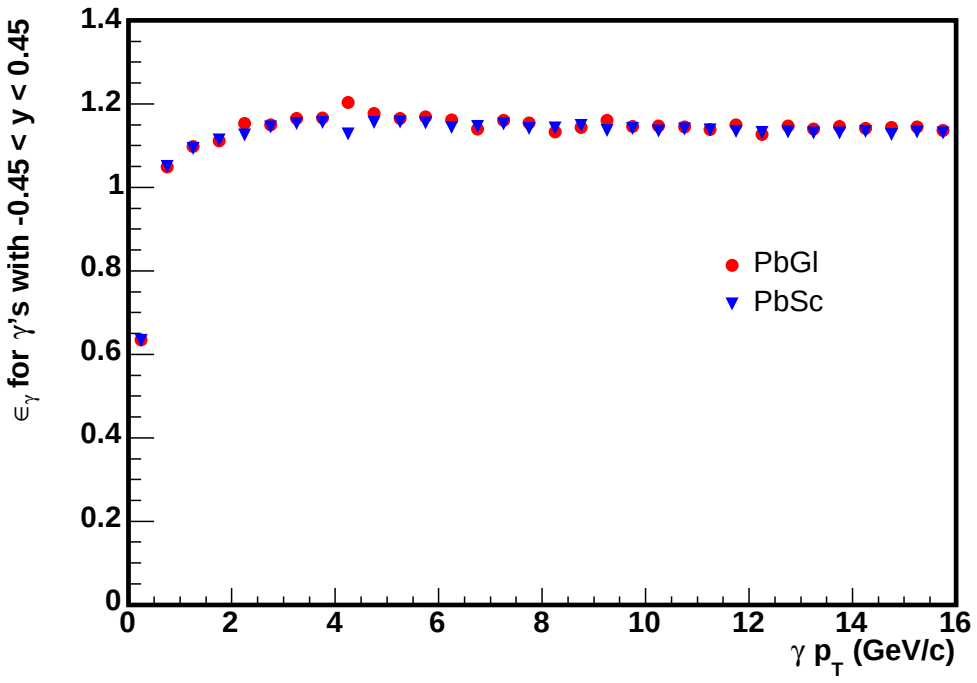

Figure 4.3: Single photon reconstruction efficiency (PID3) for PbGl and PbSc, respectivly. Since the energy resolution is similar for the two subsystems the efficiency is also similar.

Charged particle background

Charged particles are a large fraction of background for the inclusive photons. Especially at low p_T the charged particles contribute a huge part of the raw EMCal cluster spectrum, because charged hadrons deposit on the average only a fraction of their energy in the EMCal and lead to a huge part of the charged particle background at low energies or transverse momenta. At higher p_T the charged particle background is dominated by photon conversion.

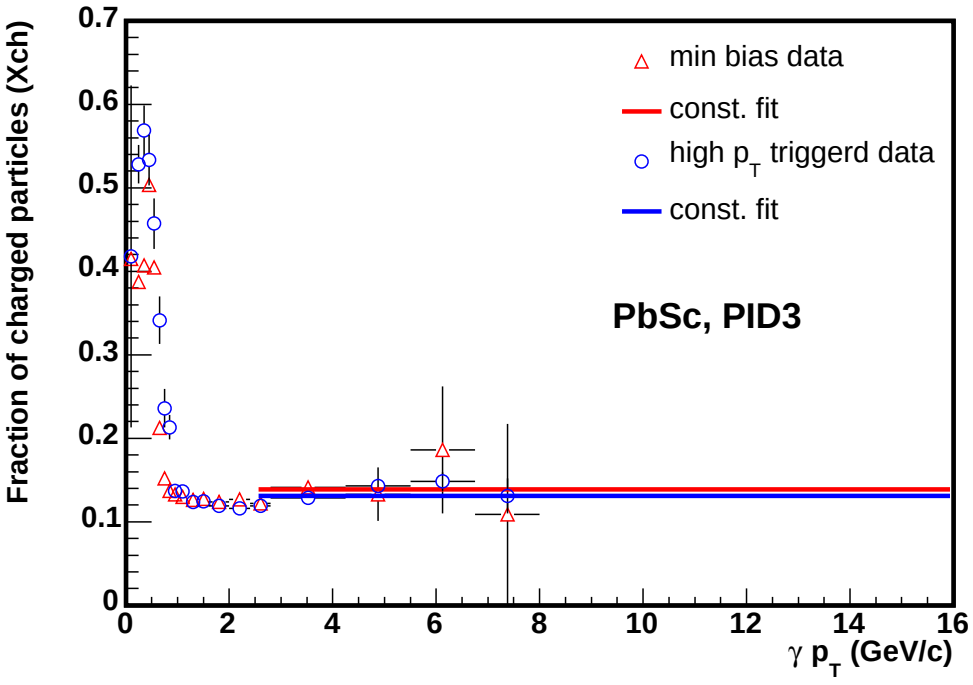

Figure 4.4: The fraction of charged hits in the uncorrected inclusive photon-spectra in the PbSc derived from minimum bias to the high p_T events after PID3. The red and blue lines are fits that are used for $p_T >$ 2.5 GeV

This fraction of charged particles that are not removed by the particle identification cuts can only be removed from the sample on a statistical basis. This is achieved by calculating the distance of each EMCal hit to the closest projection of a charged track on the detector surface. The PC3, which is installed just in front of the EMCal as can be seen in Figure 3.6), is suited to correlate charged hits with hits from the EMCal and therefore serves as a charged particle detector. The procedure is the following:
After projecting a hit signal in the PC3 on the detector surface of the EMCal using a

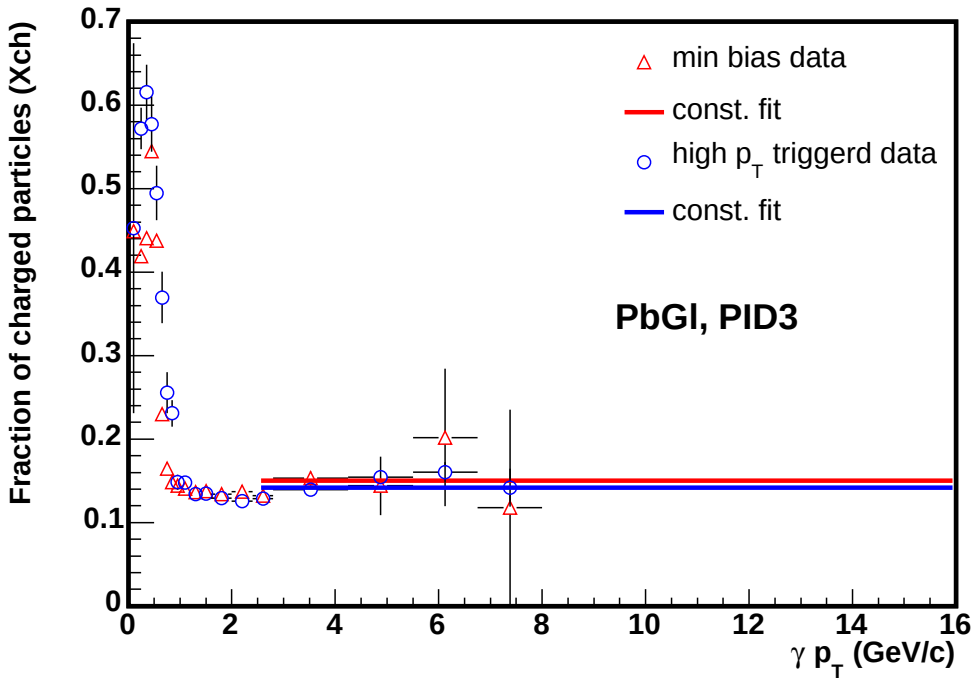

Figure 4.5: Same as Fig: 4.4 but for PbGl. The constant exploration of minimum Bias and high p_T begins at p_T = 2.5 GeV/C.

straight line defined by the PC3 hit and the collision vertex, hits in the EMCal within a certain veto radius are counted as charged hits and are used to correct the inclusive photon sample. The applied veto radius decreases with p_T and covers a range from 25 cm down to 10 cm. To avoid that hits in the EMCal are accidentally correlated with charged hits in the PC3, a mixed event technique has been used. It has to be remarked that one disadvantage of the employed mixed-event technique could be that it is only correct for random associations if the charged hit and the photon are uncorrelated. This is not the case for photons produced in a hadron jet or for π^0 decay photons where one photon converted. The effect of the latter is examined in more detail in [KB04]. For the final correction of the charged contamination a constant extrapolation is used above $p_T = 2.5\,\mathrm{GeV}/c$ (PbGl) and $p_T = 4.5\,\mathrm{GeV}/c$ (PbSc). A constant extrapolation is justified because only the contribution of single-photon conversions at large p_T is desired. This loss of photons is corrected with the conversion correction described below.

For photons originating from a π^0 decay one would expect that the fraction of tagged photons is larger than in the simulation of single photons, because for increasing transverse momentum the two decay photons approach each other and the conversion of one pho-

	PC3 efficiency
PbGl	85 % ± 5 %
PbSc	92 % ± 5 %

Table 4.3: The efficiency of PC3 with the acceptance of PbGl and PbSc. Because of inactive areas of of the PC3 the efficiency gets lower than one.

ton can tag both as charged. This must not be considered, because the contribution from decay photons has already been considered in the background calculation described in Section 4.2.2. When using the PC3 as charged particle veto detector, its efficiency within the EMCal acceptance must be taken into account (see [Zau05]). In Table 4.3 the derived efficiencies of the PC3 in the acceptance range of the EMCal are shown for the two different subsystems.

Neutron/Antineutron background

The raw photon spectrum is also contaminated by neutrons and anti-neutrons which have to be subtracted. The fraction of neutral hits in the EMCal is determined using the same simulation that has already been used in the Au+Au [KB04] and p+p [Rey05] direct-photon analysis in run II. In the simulation, the efficiency of the calorimeter for neutrons and antineutrons $\varepsilon_{n/\bar{n}}$ can be determined. Together with the geometrical acceptance for single particles $a_{n/\bar{n}} = a_\gamma$, this efficiency can be used to derive the uncorrected, raw response of the EMCal to neutrons with a given input spectrum:

$$\left.\frac{d^2N}{dp_T dy}\right|_{n/\bar{n}}^{raw} = \varepsilon_{n/\bar{n}} \cdot a_{n/\bar{n}} \cdot \left.\frac{d^2N}{dp_T dy}\right|_{n/\bar{n}}. \tag{4.14}$$

The correction used in this analysis is identical to the correction in run II p+p (see Fig. 4.6).

Conversion Correction

The conversion correction has been established to account for photons that convert ($\gamma \rightarrow e^+e^-$) in the region between the collision vertex and the PC3. These photons are removed by the charged particle correction (see above). This has to be corrected by calculating the contribution of conversion in the relevant region and then adding the corresponding fraction of photons to the sample. A big advantage of the PC3 is that it is close to the EMCal. This is the reason why conversions taking place between PC3 and EMCal do not

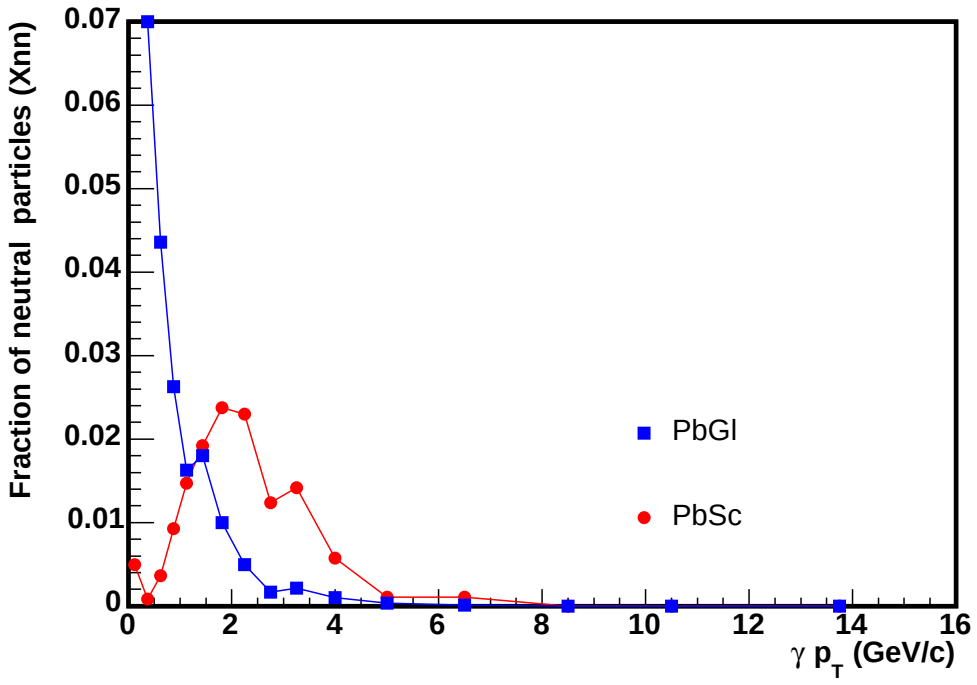

Figure 4.6: Fraction of the Neutron/Antineutron Background correction.

material	PbGl	PbSc East	PbSc West
beam pipe, air, DC, MVD	0.013	0.013	0.013
PC1	0.012	0.012	0.012
RICH	0.021	0.021	0.021
PC2	–	–	0.024
TEC/TRD	0.064	0.064	–
Air	0.003	0.003	0.003
Total	0.113	0.113	0.073

Table 4.4: The material budget in terms of radiation lenght X_0.

have to be considered. If a photon converts in this region, the resulting e^+e^- pair will form one single cluster that is identified as a photon cluster with the full energy of the original photon. To determine the conversion probability before the PC3 the material budget in the relevant region is taken from [Ent04]. Applying the parameters from Table 4.4 the photon conversion probability c_{conv} was calculated as:

	Photon Conversion Probability c_{conv}
PbGl	0.084
PbSc East	0.084
PbSc West	0.055
PbSc Total	0.065

Table 4.5: Photon conversion probabilities used as correction terms.

$$c_{\text{conv}} = 1 - \exp(-\frac{7}{9} \cdot \sum_i \frac{X_i}{X_0}), \tag{4.15}$$

where X_0 is the radiation length and X_i is the thickness of the corresponding material i. The results are given in Table 4.5 where the conversion correction for the whole PbSc was determind by taking the mean of PbSc West and PbSc East weighted with the number of sectors in the corresponding arm.

Trigger Efficiency

The calculation of the trigger efficiency is already explained in Subsection 4.1.1. The ERT trigger efficiency is for PbGl: $\varepsilon^{\text{ERT}}_{\text{PbGl}} = \pm 0.76$ and for PbSc: $\varepsilon^{\text{ERT}}_{\text{PbSc}} = \pm 0.89$.

Bin-Shift Correction

The bin-shift correction takes into account, that in the case of steeply falling spectra an error is introduced when plotting the extracted yield for a given transverse momentum at the center of the bin. The cause is that the geometrical center of the bin does not represent the center of gravity of the entries. This effect becomes worse for larger bin widths and steeper falling spectra. To correct this effect, two methods are possible. The first would be a shift in vertical direction keeping the y-value and the second a shift in horizontal direction keeping their p_{T}-values. The second method is preferred because the different spectra will keep their p_{T}-values and thus can be compared much better by taking point-to-point ratios.
In order to derive the shift, a fit to the invariant yield following Equation 4.16 is used as an approximation of the true spectrum:

$$\begin{aligned} \frac{\mathrm{d}N}{\mathrm{d}p_{\text{T}}} &= p_{\text{T}} \cdot a_{\text{WS}} \cdot \left(\frac{p_1}{b_1 + p_{\text{T}}} \right)^{b_2} \\ &\quad + p_{\text{T}} \cdot (1 - a_{\text{WS}}) \cdot \left(\frac{b_3}{p_{\text{T}}} \right)^{b_4}, \end{aligned} \tag{4.16}$$

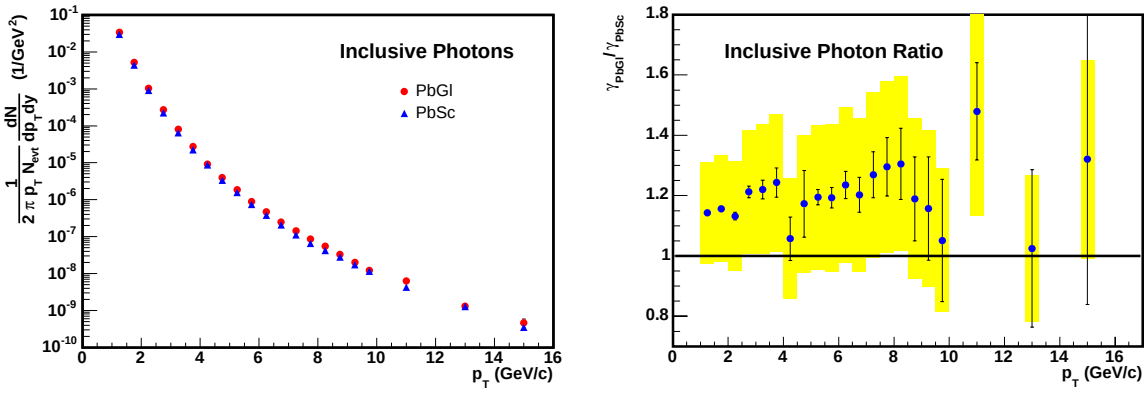

Figure 4.7: Invariant yield of the inclusive photon spectra in d + Au collisions for PbGl and PbSc (right). Ratio of the inclusive photon spactra of PbGl over PbSc. The yellow bars are the systematic errors of the ratio. The cross over from minimum bias to high p_T is chosen at 5 GeV/c.

$$\text{with } a_{WS} = \frac{1}{1+\exp(\frac{p_T - a_1}{a_2})}.$$

For the resulting function $f(p_T)$ the average yield in a given bin with center p_T^c and width Δp_T is compared to the value of the function at the center:

$$r = \frac{\frac{1}{\Delta p_T}\int_{p_T^c-\Delta p_T}^{p_T^c+\Delta p_T} f(p_T)\mathrm{d}p_T}{f(p_T^c)}. \tag{4.17}$$

The corrected yield is then given by:

$$\left.\frac{\mathrm{d}N}{\mathrm{d}p_T}\right|_{\text{corrected}} = \frac{\mathrm{d}N/\mathrm{d}p_T|_{\text{uncorrected}}}{r}. \tag{4.18}$$

As the shifted data points also lead to a different fit result, the fit procedure and the bin shift need to be repeated until the yield corrections become negligible. The correction is in the order of a few percent compared to the original yield.
Figure 4.7 shows the completely corrected invariant yield of the inclusive photons for PbGl and PbSc together with the ratio of PbGl over PbSc.

4.2.2 π^0 Spectra

To extract the direct photons from the inclusive photon yield a good known ledge to the background of photons from hadronic decays is needed. The decay of the π^0 is the largest contribution of the background photons from hadronic decays and forms the basis for the

State	Mass (MeV/c^2)	R_{h/π^0}	Decay branch	Branching ratio
π^0	134.98	–	$\gamma\gamma$	98.798%
			$e^+e^-\gamma$	1.198%
η	547.8	0.45	$\gamma\gamma$	39.43%
			$\pi^+\pi^-\gamma$	4.68%
			$e^+e^-\gamma$	$4.9\cdot10^{-3}$
			$\pi^0\gamma\gamma$	$7.1\cdot10^{-4}$
			$\mu^+\mu^-\gamma$	$3.1\cdot10^{-4}$
ω	782.6	0.8	$\pi^0\gamma$	8.5%
			$\eta\gamma$	$6.5\cdot10^{-4}$
η'	957.8	0.8	$\rho^0\gamma$	30.2%
			$\omega\gamma$	3.01%
			$\gamma\gamma$	2.11%

Table 4.6: Dominant sources of background photons from hadronic decays and the employed m_{T} scaling factors relative to the π^0 measurement R_{h/π^0}. The listed masses, decay branches, and branching ratios are taken from [Eid04].

approximation of the whole background. It is about 85 % of the hole backround photon yield as can be seen in Tabel (4.6). Thus the π^0 spectrum forms the input for a simulation of the hadronic background calculated with the same Monte Carlo method as used for the acceptance and efficiency calculation. The extraction of the π^0 photons is not part of this work but will be outlined for completeness. For more detail see [Bat03].

Neutral pions are detected via their 2γ decay channel. Because of the relatively short mean lifetime of neutral pions of about 10^{-16} s, typical for electromagnetic decays, the pions decay before escaping from the collision region. This makes the decay vertex well known and the pions can be reconstructed via an invariant mass analysis of photon pairs measured by the EMCal.

Invariant Mass Analysis

The invariant mass of a particle pair is given by the absolute value of its four-momentum $P_{12} = P_1 + P_2$. As photons are massless particles this reduces to the determination of the energy E and the opening angle θ between the two photons. This leads to the equation:

$$m_{\gamma\gamma} = \sqrt{\left(P_{\gamma_1} + P_{\gamma_2}\right)^2} = \sqrt{E_{\gamma_1} \cdot E_{\gamma_2} \cdot (1 - \cos\theta_{12})}. \tag{4.19}$$

For a photon pair originating from a π^0 decay the invariant mass is identical to the π^0 rest mass of 134.9766 MeV/c^2 [Eid04]. However, due to the finite energy and position resolution in the detection of the photon pair, the actual reconstructed value is smeared around a mean value. The bin-shift effect leads, as for the inclusive photons, to a deviation to upper values from the nominal 135 MeV as can be seen for PbGl in Figure (4.8).

With the invariant mass analysis the respective π^0 cannot be identified since all possible

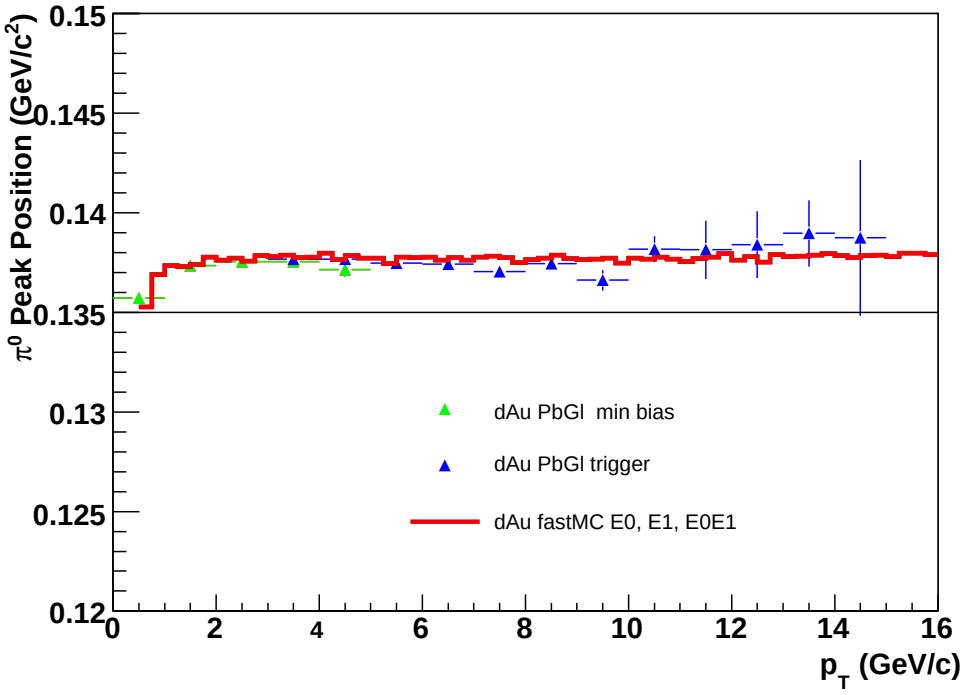

Figure 4.8: The π^0 peak position in GeV/c^2 versus p_T for PbGl. The bin-shift effect leads to a deviation to upper values from the nominal 0.135 GeV. The Figure looks for PbSc similar.

photon-photon combinations have to be considered which lead to a large combinatorial background. One important way to reduce this background is the *mixed event* method described below. For other ways to reduce the combinatorial background like a cut on the energy asymmetry see [KB04].

Mixed Events

The mixed event technique is widely used to determine the combinatorial background of combined particles for example used in the charged particle correction (see Section 4.2.1). The basic idea is to compare the result obtained by combining particles within one event to the result for particle combinations from different events, which are a priori not correlated. After scaling the mixed events describe the background and can be subtracted.

Efficiency and Acceptance

To obtain fully corrected spectra similar corrections as for the inclusive photons are needed. The **geometrical acceptance** of the π^0 is basically calculated similar as for single particles. In addition it is to be considered that two photons are needed for detection which leads to a dependence on the kinematics of the π^0 decay, namely the opening angle between the two photons and hence the transverse momentum of the π^0.

The **efficiency** of the π^0 detection is also determined similar to the inclusive photons. In addition to the efficiency calculation described in [Bat03] a *shower merging correction* has been implemented, which accounts for the fact that decay photons at high-p_{T} cannot be separated.

Shower Merging

For the direct-photon analysis it is of importance to have a simulated hadron decay spectrum of the photons. One effect, important at higher p_{T}, that has to be considered is the shower merging. The minimum opening angle between decay photons of π^0s dependent on the energy of the π^0 as can be seen in Equation 4.19. As higher energies of the decay photons mean higher transverse momenta, the minimal distance d_{min} of the photons on the detector surface gets smaller for increasing p_{T} in GeV:

$$d_{\mathrm{min}}(p_{\mathrm{T}}) \approx \frac{2 \cdot 540 \cdot \tan\left(1/2 \cdot \mathrm{acos}\left(1-(0,135)^2\right)\right)}{1/2 \cdot p_{\mathrm{T}}^2}\mathrm{cm}. \tag{4.20}$$

If two photons are too close to each other to get separated by the detector we call the photon showers merged. This effect has to be included to the π^0 decay photon simulation as the merged photons in the photon spectrum are already excluded by the shower shape cut. This effect is simulated with a Monte Carlo simulation, where the shower width is

implemented. The merging effect was only calculated for π^0's as they build the major part of the decay background and $d_{\min}$ increases for hadrons with higher masses. It is included to the γ/π^0 results (see below) and leads to the decrease of the γ/π^0 for higher p_T seen in Figure 4.10. This effect is larger for PbSc, what comes from the lower granularity of the PbSc in relation to PbGl.

Calculation of the Background from Radiative Decays

The expectation of photons from hadronic decays is determined within the same Monte Carlo simulation employed for the acceptance calculation. The most important input to this simulation is the parameterization of the π^0 yield measured within the same data sample as used for the direct-photon analysis. The decay photons from π^0s are calculated, by simulating there decay on a statistical basis. The other hadronic decays are determind using the m_T scaling (see Section 2.3). For example for the determination of the decay background from ηs in the Fast Monte Carlo we scale the production cross section as given by Equation (2.5) with a factor of $R_{\eta/\pi^0} = 0.45 \pm 0.05$ relative to the parameterized π^0 yield. Other hadrons that contribute to the background photons are listed together with their relevant decay channels in Table 4.6.

4.2.3 γ/π^0 Double Ratio

Now the measured spectra and the expected yield of photons per π^0, calculated with the same fast Monte Carlo as used for the acceptance and efficiency correction, originating from hadronic decays can be compared. This is done for the direct-photon analysis to reduce the systematic error as will be explained in Section 4.2.5. The cancellation effects are:

- The error on the energy scale, which is reduced in general and cancels if it is an overall scale factor,
- The uncertainty in the efficiency calculation, which partially cancels as the single photon efficiency has a direct impact on the two-photon efficiency needed for the invariant mass analysis of the π^0,
- The systematic error due to the conversion correction, which partially cancels for the same reason,
- The overall normalization error of the Level-1 trigger.

A direct comparison of the point-by-point ratio of measured inclusive photons to the measured π^0s, determined with the same PID cuts, is shown in Figure 4.10. The photon

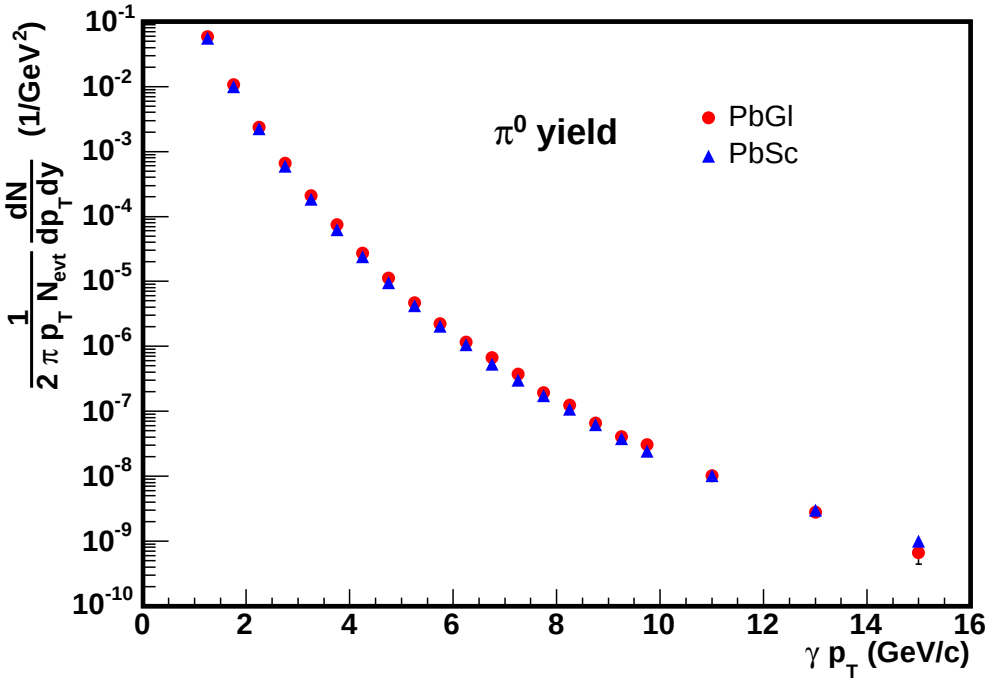

Figure 4.9: Invariant yield of the π^0s for PbGl and PbSc. The cross over from minimum bias to high p_T data is chosen at p_T = 5 GeV.

excess can be characterized more directly in the double ratio of the $\gamma/\pi^0|_{\text{meas}}$, the measured photons per π^0, to the $\gamma/\pi^0|_{\text{bkgd}}$, the expectation from hadronic decays:

$$\frac{N^\gamma/N^{\pi^0}\Big|_{\text{meas}}}{N^\gamma/N^{\pi^0}\Big|_{\text{bkgd}}} = \frac{N^\gamma_{\text{meas}}}{N^\gamma_{\text{bkgd}}} =: R_\gamma. \tag{4.21}$$

This so called double ratio is equivalent to the direct comparison of measured photons to decay photons, since the measured π^0 spectrum and the input π^0 distribution for the decay photon calculation should be the same by construction and cancel each to a large extent. This cancellation introduces only a small systematic error, as it is only sensitive to variations of the shape of the spectrum, not to the overall normalization. An excess above unity reflects a direct-photon signal (see Figure 4.11).

4.2.4 Statistical Error

Equation (4.9) shows that the direct-photon signal is determined as a fraction of the measured direct photon candidate sample. The fraction is determined by the photon excess R_γ

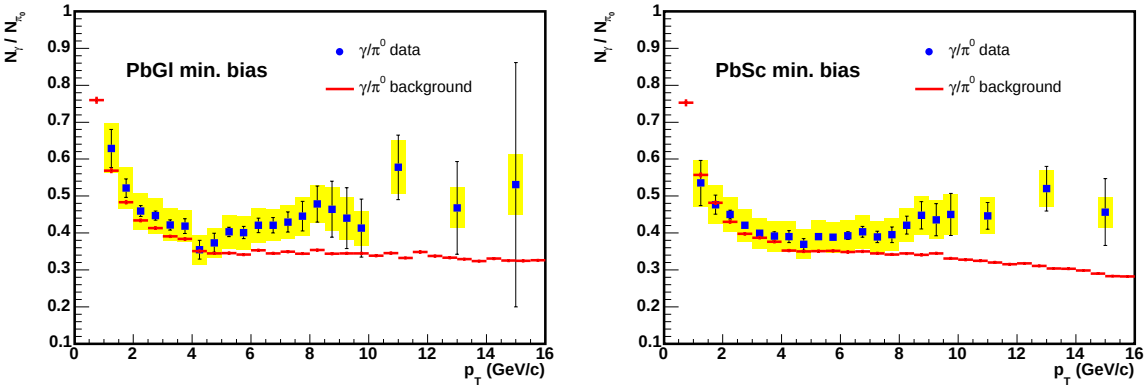

Figure 4.10: γ/π^0 spectra for PbGl and PbSc with shower merging effect for the background. The yellow boxes show the systematic error. The black error bars are the systematic error. As π^0 spectrum a fit to the data is used.

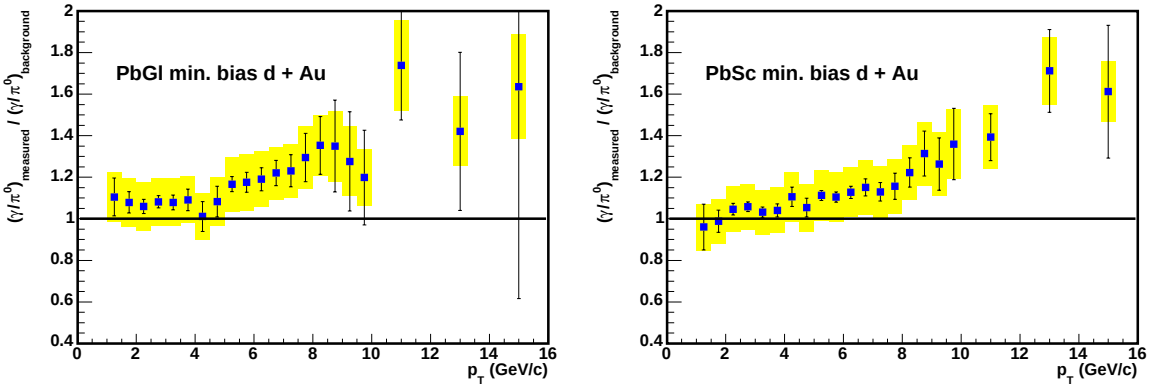

Figure 4.11: Double ratio for PbGl and PbSc. The yellow boxes show the systematic error, while the error bars reflect the statistical error.

(see Equation (4.21)). The error is determined by the asymmetric error of $\left(1-\frac{1}{R_{\text{gamma}}}\right)$ of the inclusive photon sample γ_{meas}. This leads to the equations for the upper and the lower error of γ_{direct}:

$$\sigma_{\text{high}}(\gamma_{\text{direct}}) = \left(1-\frac{1}{R_\gamma+\sigma(R_\gamma)}\right)\cdot(\gamma_{\text{meas}}+\sigma(\gamma_{\text{meas}}))-\gamma_{\text{direct}} \tag{4.22}$$

and

$$\sigma_{\text{high}}(\gamma_{\text{direct}}) = \gamma_{\text{direct}}-\left(1-\frac{1}{R_\gamma+\sigma(R_\gamma)}\right)\cdot(\gamma_{\text{meas}}+\sigma(\gamma_{\text{meas}})). \tag{4.23}$$

A Gaussian error propagation is in this case not adequate because the approximation of the function with a tangential in a point to project the error onto the reciprocal function, does not work if the change of the slope of the function is to high. This is the case for R_γ and leads to an asymmetric error as illustrated in Figure (4.12).

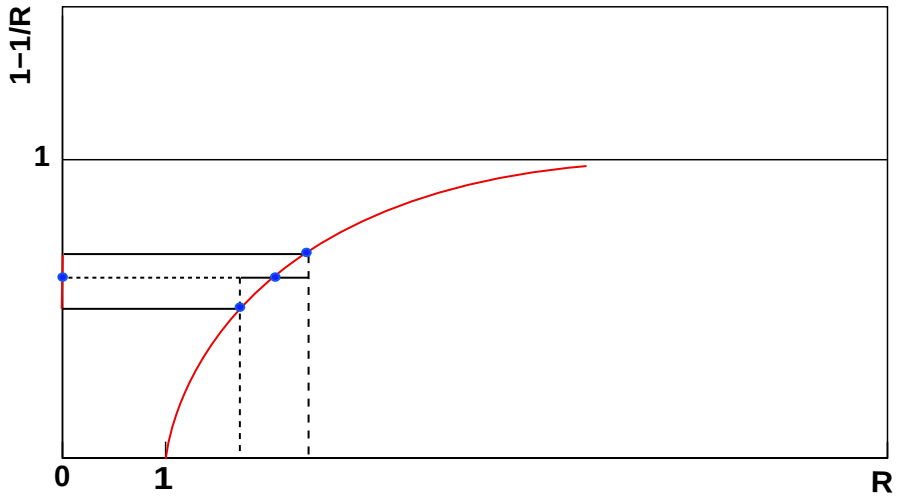

Figure 4.12: The Gaussian error propagation dose not work for $1-\frac{1}{R_\gamma}$. A projection of the error of R_γ onto $1-\frac{1}{R_\gamma}$ leads to asymmetric statistical and systematic errors.

4.2.5 Systematic Error

All systematic errors are estimated as 1 σ errors and summarized in Table 4.7. The systematic errors in this table are characterized as follows [Sah04]:

Systematic errors	type
Photon Yield:	
Charged background	B
Neutral background	B
Conversion correction	C
Shower merging correction	B
Neutral Pion Yield:	
Conversion correction	B
Shower merging correction	B
Peak extraction	A
Strongly Correlated Errors:	
Ratio of γ and π^0 eff.	B
Energy scale calibration	B
Geometric acceptance	B
Further Errors:	
Fit to Neutral Pion Spectrum	A

Table 4.7: Summary of the dominant systematic errors of the electromagnetic calorimeters to measure direct photons and there error type.

Type A (probably) p_T-correlated error, however, the correlation is not known (e.g. points at low p_T might move down while points at high-p_T move up). Thus, it is most conservative to treat this error as p_T uncorrelated.
Type B p_T -correlated error, all points move in the same direction by different factors.
Type C p_T -correlated error, all points move by the same factor (scale error).

If the systematic error of type B is parameterized by a linear function then the constant term of this function can be treated as a scale error (type C). The following sections describe in some detail how the errors were estimated.

Detector Acceptance

Though the geometry of the detector is known, the parameterization of the difference between the impact point of the photon on the detector surface and the maximum tower position of a cluster leads to some uncertainty in the fastMC. The fastMC uncertainty was estimated in a previous analysis of π^0s (see [Rey03]).
It is still under discussion if some detector parts are shifted in comparison to the previously used values (see Appendix D). This would have only a little effect on the acceptance but a remarkable effect on the energy scale [Pre05]. This is tested to be in the systematic error region of the energy scale described below.

Reconstruction Efficiency

The reconstruction efficiency calculation has to consider the cuts for photon identification as well as the energy resolution of the detectors. Thus there are two sources leading to systematic errors in the reconstruction efficiency. The systematic error due to the PID cuts is estimated by comparing the fully corrected yields for different PID classes. The error due to the energy smearing is done by changing the energy smearing in the fastMC described in [KB04]. The quadratic sum of these two errors is given in Table 4.8 for the inclusive photons.

Energy Scale

The main contribution to the systematic uncertainty is the determination of the energy scale. Based on the comparison of the π^0 peak position described above, the energy scale can only be determined with limited accuracy. Therefore, the 1 σ uncertainty in the energy scale is estimated to be 1.5%. The smeared energies are shifted by 1.5% in the fastMC to qantify the error in the yields due to this uncertainty. An energy scale shift caused by a wrong detector geometry is covered by this error.

Gamma1 Normalization Scale

As described in 4.1.1 the normalization of the ERT-triggered data used for higher p_T has to be performed using the scaler counts from the run-control. A comparison of two different scaling methods described in [Bat03] and [Rey05] leads to a difference of about 5%.

Conversion Correction

The systematic error of the conversion correction which is used in this thesis is estimated in [Rey05].

	PbGl		PbSc	
p_T in GeV/c	3.25	8.75	3.25	8.75
Acceptance	3%	3%	3%	3%
Efficiency	4%	4%	4%	4%
Charged particles (X_{ch})	1%	1%	1%	1%
Neutron correction ($X_{n\bar{n}}$)	$\ll 0.1\%$	$\ll 0.1\%$	$\ll 0.1\%$	$\ll 0.1\%$
Conversions	2%	2%	2%	2%
Gamma1 Normalisation	—	5%	—	5%
Trigger Efficiency	—	6 %	—	5%
Energy scale	8.4%	16.8%	8.4%	17.1%
Total syst.	9.7%	19.3%	9.7%	19.3%
Statistical	1.8%	8.2%	1.1%	4.8%

Table 4.8: Summary of the dominant sources of systematic errors on the inclusive photon yields extracted independently with the PbGl and PbSc electromagnetic calorimeters in central d + Au events for different p_T and for PID3.

Charged and Neutral Background Correction

The charged and neutral background is already calculated for p+p collisions in Run 3 the systematic error is also identical (see [Rey05]).

Merging Correction

It is shown that to get a systematic error for the shower merging only the uncertainty of the simulated shower in the used Monte Carlo is of relevance [Zau05]. An upper limit of this error is calculated by simulating showers in only one detector segment and merging them. The result of this merging correction is afterward coopered with the normal merging correction. The discrepancy gives an upper limit for the systematic error. Other errors like the uncertainties of the energy scale are negligible.

4.2.6 Combination of PbSc and PbGl

One of the special properties of the EMCal is the employment of two detector types, which have been analyzed separately in this work as can be seen for the photon yields in Figure 4.7. These two different detector types have been used for a internal consistency check. The comparison of the results shows an overall agreement within the systematic error, also shown in Figure 4.7. This difference is still not understood but well covered by the

error assigned to the individual measurements, so a combination of the results obtained with both detectors is justified. The analysis of two different detector types provides two essentially independent measurements. That leads to a reduction of the total error for the combined results. For combination of the data of PbGl and PbSc the same method as used for the π^0 results is used [Eid04]. This standard weighted least squares method gives the average yield $\bar{x}(p_T)$ in dependence of p_T and the 1 σ error $\delta\bar{x}(p_T)$ by:

$$\bar{x}(p_T) \pm \delta\bar{x}(p_T) = \frac{\sum_{i=1}^{N} w_i(p_T) x_i(p_T)}{\sum_{i=1}^{N} w_i(p_T)} \pm \left(\sum_{i=1}^{N} w_i(p_T) \right)^{-1/2}, \quad (4.24)$$

with

$$w_i(p_T) = \frac{1}{\delta x_i(p_T)^2}. \quad (4.25)$$

x_i and δx_i are the yield and the total error of the measurement at given p_T determined with the PbGl ($i = 1$) and with the PbSc ($i = 2$), respectively, and $N = 2$. Since the total error of each individual measurement is given by the quadratic sum of the statistical error $\delta x_i^{stat}(p_T)$ and the systematic error $\delta x_i^{sys}(p_T)$, the combined error can be rewritten after some transformations as [KB04]:

$$\left(\delta\bar{x}^{stat}(p_T)^2 + \delta\bar{x}^{sys}(p_T)^2 \right), \quad (4.26)$$

with

$$\begin{aligned} \delta\bar{x}^{stat}(p_T)^2 &= \sum_{i=1}^{N} \frac{1}{N} \frac{w_i}{\sum_{j=1}^{N} w_j(p_T)} \cdot \delta x_i^{stat}(p_T)^2, \\ \delta\bar{x}^{sys}(p_T)^2 &= \sum_{i=1}^{N} \frac{1}{N} \frac{w_i}{\sum_{j=1}^{N} w_j(p_T)} \cdot \delta x_i^{sys}(p_T)^2. \end{aligned} \quad (4.27)$$

Similar decomposition of the total error of the combined result also holds for the different types of errors contributing to the systematic error. This is especially important for quantities in which a part of the systematic error cancels (see 4.2.3).

A cross-check of the combined result is made via the χ^2 value. If

$$\chi^2 = \sum_{i=1}^{N} w_i (\bar{x} - x_i)^2 \quad (4.28)$$

is smaller than or equal to $(N-1)$, which is the expectation value of χ^2 if the measurements follow a Gaussian distribution.

If the χ^2 value exceeds this expectation, the total error $\delta\bar{x}$ of the combined result is increased by a scale factor S given by

$$S = \sqrt{\chi^2/(N-1)} \tag{4.29}$$

for S $\leq$ 3 (see [Eid04]).

A table of the results is given in Appendix E.

5. Results

A comparison of the $\gamma/\pi^0|_{\mathrm{meas}}$ and $\gamma/\pi^0|_{\mathrm{bkgd}}$ already shows (see Figure 4.10) a small enhancement of photons compared to the expectation from hadronic decays above $p_{\mathrm{T}} = 5\,\mathrm{GeV}/c$. For lower transverse momenta the measured ratio agrees with the calculated background. This direct-photon signal will be interpreted and compared with theoretical predictions in the following chapter.

5.1 Direct-Photon Yields

As already shown in section 4.2, Equation 4.9 illustrates the method to obtain the final invariant yield of direct photons. To obtain the systematic error of the final direct-photon yields, systematic errors of the double ratio R_γ and of the inclusive-photon yields have to be combined. It is only necessary to consider those errors of the inclusive yields which canceled in the double ratio. This was already explained in Section 4.2.3. The direct-photon yields for PbGl and PbSc are shown in Figure 5.1. A combined yield of the direct-photon yields of these two independent detector systems is obtained by a combination of the combined inclusive yield and the combined π^0 yield. These combinations of the inclusive photons and the π^0 yields are made with the standard weighted least squares method described in Section 4.2.6. The $\gamma/\pi^0|_{\mathrm{bkgd}}$ is again calculated with the fast Monte Carlo method [Rey03]. This direct-photon yield is given in Figure 5.2 and shows a significant direct-photon signal over three orders of magnitude.

The comparison with the NLO pQCD calculation scaled by the appropriate number of binary collisions is also shown in the Figures 5.2 and 5.1. The data is in good agreement with the scaled direct-photon production from the calculation for p + p collisions. The higher direct-photon signal of PbGl relative to PbSc can already be seen when comparing the inclusive-photon yields. This discrepancy is within the systematic error.

5.2 R_{AB}

As already described in Section (2.5) R_{AB} is an appropriate measure for the comparison of theoretical and experimental results. In the following section, two methods to calculate R_{dAu} and comparisons with theory and experiment will be given.

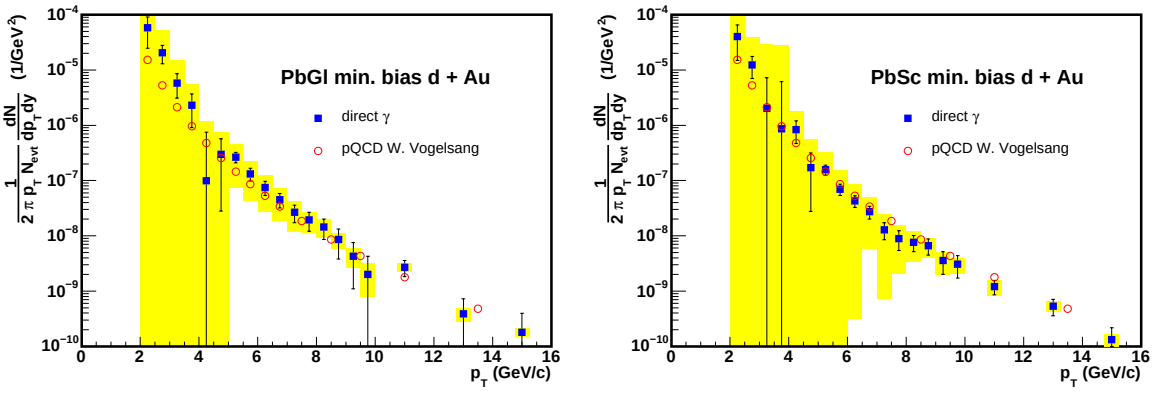

Figure 5.1: Direct-photon yields for PbGl (left) and PbSc (right). The yellow boxes show the systematic error type B and C, while the error bars reflect the statistical error and the systematic error type A. A significant signal is present for PbGl at a transverse momentum above 5 GeV/c and for PbSc above a transverse momentum of 6 GeV/c. The red circles are a NLO pQCD calculation for p + p collisions with the scale parameters $\mu = \mu_{\mathrm{fac}} = \mu_{\mathrm{ren}} = \mu_{\mathrm{fra}} = p_{\mathrm{T}}$ (Appendix F), containing the photons produced in the fragmentation process of hard scattered partons [Rey05] scaled with $\langle N_{\mathrm{coll}} \rangle_f$.

5.2.1 R_{dAu} for Direct Photons

The direct-photon production has already been compared to the expectation of the scaled production of direct photons in p + p collisions from a next-to-leading-order pQCD calculation on the absolute scale (Figure 5.2). This comparison can also be made in terms of the familiar nuclear modification factor employing a pQCD calculation as reference:

$$R_{dAu} = \frac{\mathrm{d}N^{\gamma}_{dAu}}{\langle N_{\mathrm{coll}} \rangle_f \cdot \mathrm{d}N^{\gamma}_{\mathrm{pp,pQCD}}}. \tag{5.1}$$

The resulting R_{dAu} are shown for PbGl and PbSc in Figure (5.3) and for the whole EMCal in Figure (5.4). The colored lines in the figures represent theoretical predictions including a k_T broadening, calculated in [Dum01]. In Au + Au this effect is important for the understanding of the photon signal at intermediate p_T where thermal photons of a QGP are expected to be a significant source. It reflects the influence of a intrinsic transverse momentum of the incoming partons already explained in Section (2.6.1). It can be seen that the R_{dAu} of direct photons cannot test the theory because of its high systematic error at lower transverse momenta.

A second way to determine R_{dAu} for direct photons is to use direct photons of p + p collisions measured during the third PHENIX run in the denominator. The resulting R_{dAu}

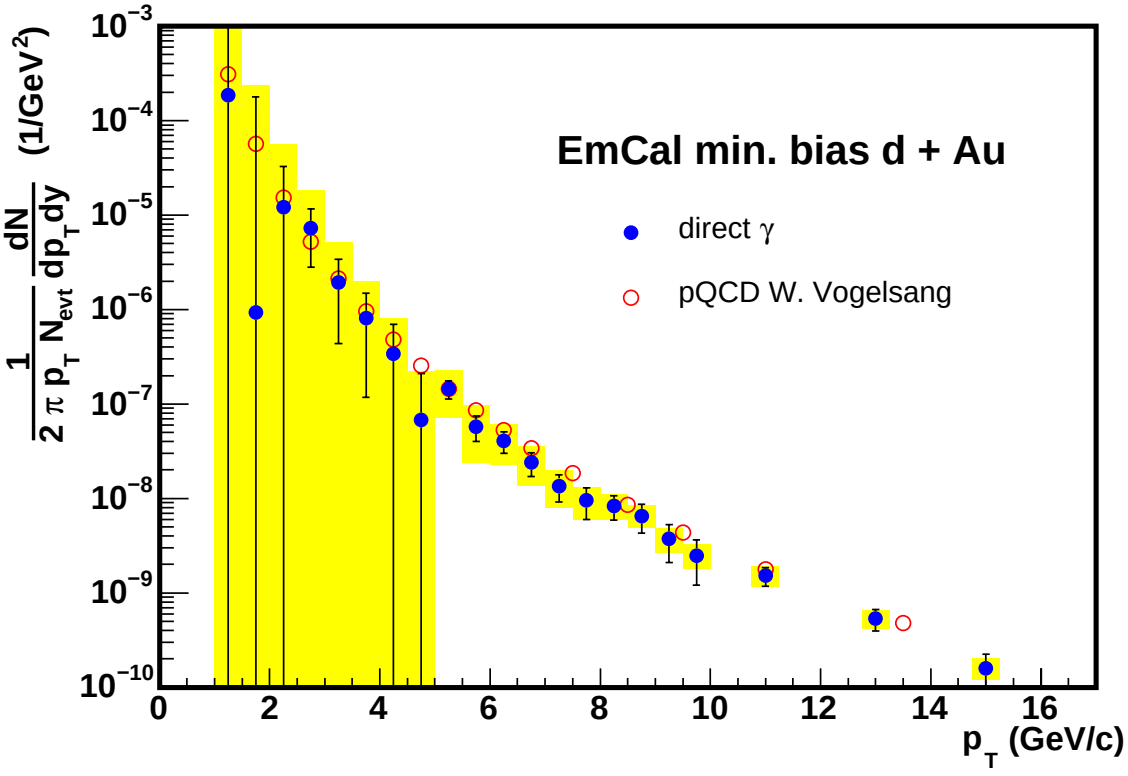

Figure 5.2: Direct-photon yields for the EMCal. The yellow boxes show the systematic error type B and C, while the error bars reflect the statistical error and the systematic error type A. A significant signal can be seen at a transverse momentum above 5.5 GeV/*c*. The red circles are a NLO pQCD calculation for p + p collisions with the scale parameters $\mu = \mu_{fac} = \mu_{ren} = \mu_{fra} = p_T$ (Appendix F), containing the photons produced in the fragmentation process of hard scattered partons [Rey05] scaled with $\langle N_{coll} \rangle_f$.

are shown in the Figures 5.5 and 5.6. This method eliminates systematic errors which are the same for p+p and d+Au collisions in PHENIX run3:

- The reconstruction efficiency is calculated in the same way.
- The acceptance is the same because of the same detector properties.
- The correction for neutral particles is identical.
- The correction for charged particles is similar.

The systematic error of the energy scale dose not cancel because the π^0 peak shifts its position slightly between different run numbers during the d + Au beam time. The figures (5.4, 5.3, 5.5 and 5.6) show clearly, that the pQCD p + p calculations and p + p

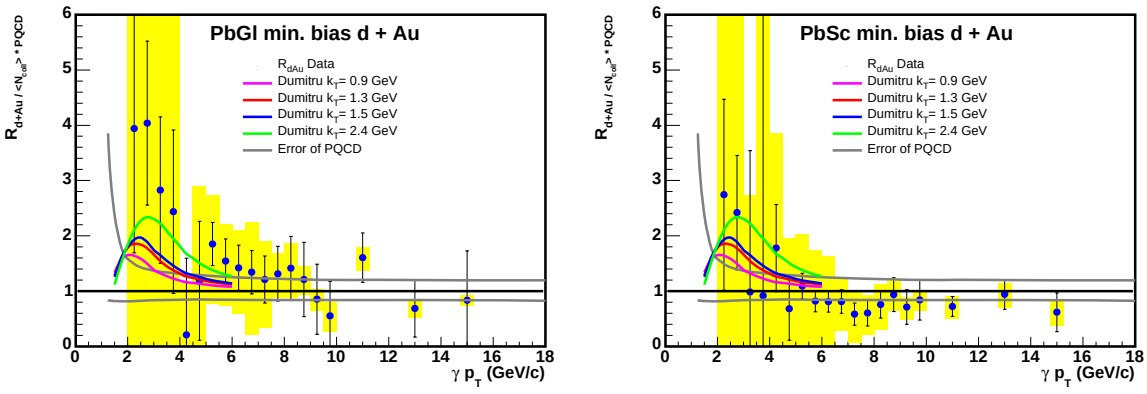

Figure 5.3: R_{dAu} for direct photons of PbGl (left) and PbSc (right). The yellow boxes show the systematic error type B and C, while the error bars reflect the statistical error and the systematic error type A. A significant signal is present for PbGl at a transverse momentum above 5 GeV/c and for PbSc above a transverse momentum of 6 GeV/c. The gray lines show the upper and lower error of the NLO pQCD calculation for p + p collisions (Appendix F) using pQCD scales $\mu = 2p_{\mathrm{T}}$ for the upper and $\mu = p_{\mathrm{T}}/2$ for the lower error [Rey05]. The pQCD, containing the photons produced in the fragmentation process of hard scattered partons, is scaled with $\langle N_{\mathrm{coll}} \rangle_f$. The colored lines show broadening effect models for different k_{T} scaling factors [Dum01].

measurements scaled with $\langle N_{\mathrm{coll}} \rangle_f$ are in good agreement with d + Au direct photons. This shows that the number of initial parton-parton scatterings at high p_{T} scales for direct photons as expected, in contrast prediction from CGC-model.

5.2.2 R_{AB} of π^0 in d + Au and Direct Photons in Au + Au

The nuclear modification factor can be used to compare the direct photons in d + Au collisions with other experimental results and theories.

R_{AB} of π^0s and the Cronin Effect

The Cronin enhancement has already been measured for π^0's in d + Au [Bat03]. One of the reasons to look for direct photons was to find another experimental hint concerning the existence of the Cronin effect. Similar to π^0's no clear Cronin effect can be separated which is shown in Figure (5.7). The direct photon R_{dAu} systematic errors are to large to draw a conclusion in the region between 1.5 GeV/c < p_{T} < 6 GeV/c for a conclusion concerning a nuclear broadening effect.

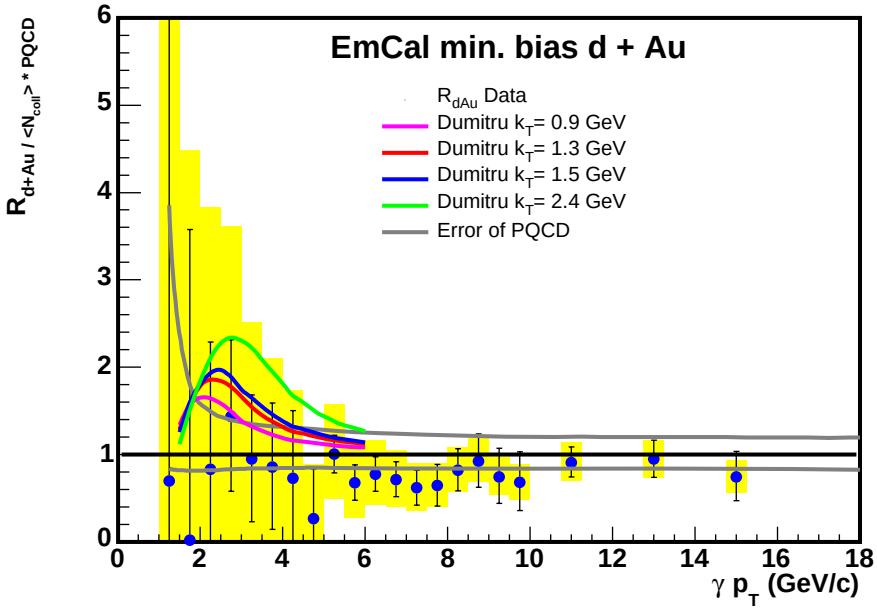

Figure 5.4: R_{dAu} for direct photons measured with the EMCal. The yellow boxes show the systematic errors type B and C, while the error bars reflect the statistical error and the systematic error type A. A significant signal can be seen for a transverse momentum above 5 GeV/c. The gray lines show the upper and lower error of the NLO pQCD calculation for p + p collisions (Appendix F) using pQCD scales $\mu = 2p_{\mathrm{T}}$ for the upper and $\mu = p_{\mathrm{T}}/2$ for the lower error [Rey05]. The pQCD, containing the photons produced in the fragmentation process of hard scattered partons, is scaled with $\langle N_{\mathrm{coll}} \rangle_f$. The colored lines show broadening effect models for different k_{T} scaling factors [Dum01].

R_{AB} of Direct Photons in Au + Au Collisions

In 2002 RHIC collided Au nuclei at $\sqrt{s} = 200$ GeV. One of the results was a direct photon R_{AB} consistent with unity for $p_{\mathrm{T}} > 4\,\mathrm{GeV}/c$ as can be seen on the left side of Figure (5.8). The R_{AuAu} for π^0s is shown in the same Figure for most central collisions. The π^0 signal is clearly suppressed with respect to the direct-photon signal in Au + Au which can be explained with jet-quenching as a final state effect. On the right side of Figure (5.8) the nuclear-modification factor of d + Au collisions is shown for π^0 and direct photons. The signals are both consistent with unity. Thus no high-p_{T} particle suppression can be observed in d + Au collisions e.g. of a color-glass condensate, what gives a clear evidence that jet-quenching is a final state effect of the hot and dense matter in central Au + Au collisions.

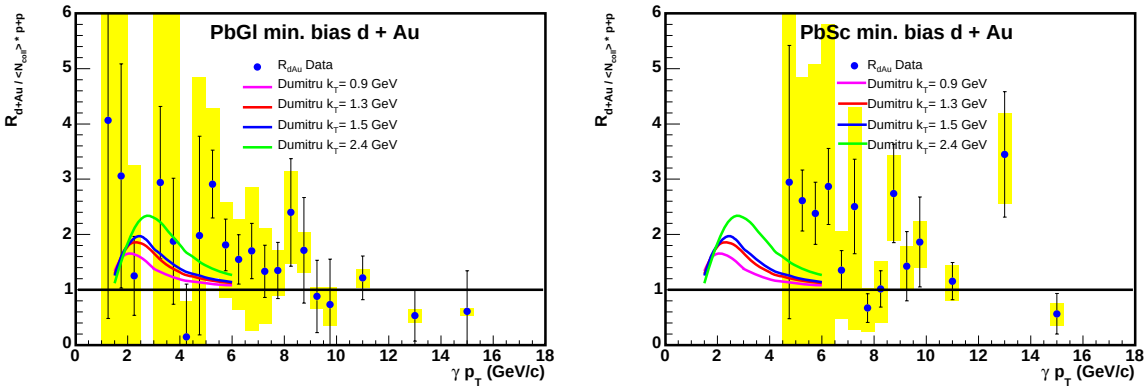

Figure 5.5: R_{dAu} for direct photons of PbGl (left) and PbSc (right) with p + p direct photons as reference. The yellow boxes show the systematic error type B and C, while the error bars reflect the statistical error and the systematic error type A. A significant signal is present for PbGl at a transverse momentum above 5 GeV/c and for PbSc above a transverse momentum of 6 GeV/c. The colored lines show nuclear broadening effect models for different k_T scaling factors [Dum01].

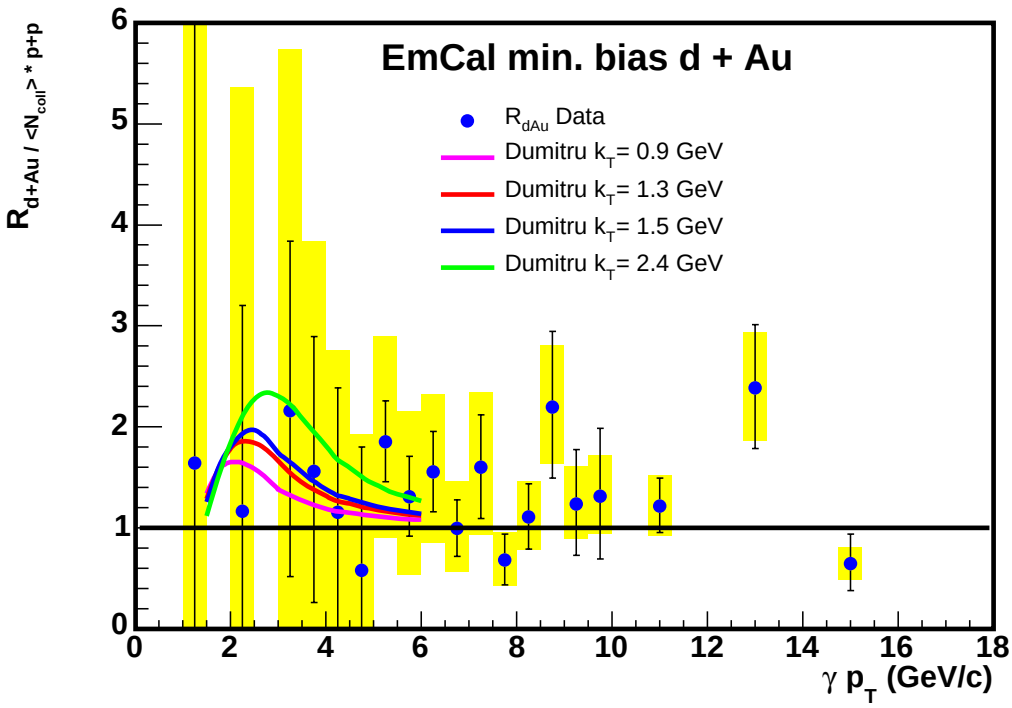

Figure 5.6: R_{dAu} for direct photons for the EMCal with p + p direct photons as reference. The yellow boxes show the systematic error type B and C, while the error bars reflect the statistical error and the systematic error type A. A significant signal is present at a transverse momentum above 5 GeV/c. The colored lines show nuclear broadening effect models for different k_T scaling factors [Dum01].

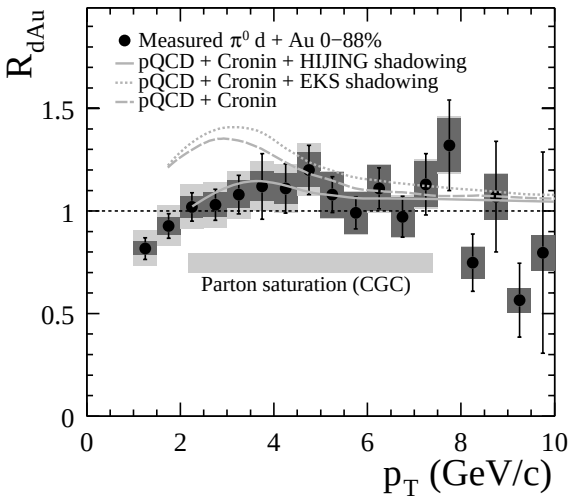

Figure 5.7: R_{dAu} for π^0 of the EMCal together with theoretical predictions from the parton saturation model (CGC) in [Kha03] and of the expectation of nuclear shadowing and Cronin enhancement [Lev03], with different shadowing parameterizations.

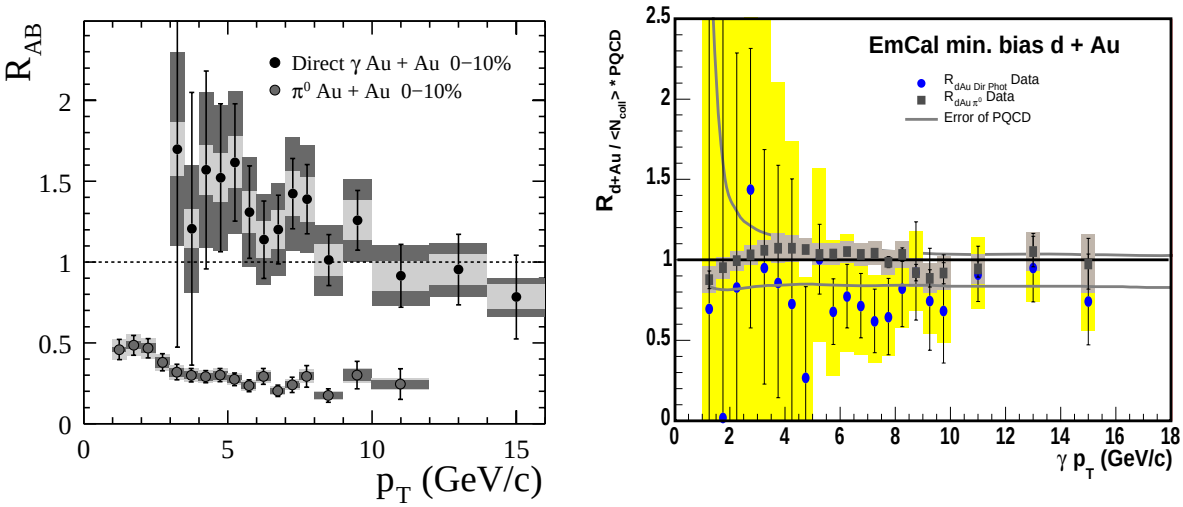

Figure 5.8: R_{AuAu} for direct photons and π^0s measured with the EMCal of the most central collision (right) from [KB04]), together with R_{dAu} for direct photons and π^0s measured with the EMCal for all centralities (left).

6. Conclusions

In this thesis the production of direct photons in d + Au collisions at a collision energy of $\sqrt{s_{NN}}$ = 200 GeV has been studied. The analysis bases on measurements of the PHENIX experiment at the RHIC collider at BNL. The results of the analysis have been used to calculate the nuclear modification factor R_{dAu} for direct photons.

The transverse momentum distribution of the direct photon yield is determined by subtracting the photons coming from hadronic decays from the inclusive photon yield. The photons from hadronic decays are determined by simulations based on the π^0 measurement of the same data set. The photons are measured with the PHENIX detector, the thesis describes the steps which are necessary to obtain fully corrected direct photon yields as a function of the transverse momentum.

The nuclear modification factor R_{dAu} is calculated in two different ways.
First, as the ratio of the direct photon yield in d + Au with pQCD predictions for p + p collisions, scaled with the number of binary nucleon nucleon collisions N_{coll}.
Second, as the ratio of the direct photon yield in d + Au and p + p collisions, again scaled with N_{coll}.
The particle yields of direct photons are expected to scale with N_{coll} for $p_T \gtrsim 2$ GeV/c in absence of medium effects.

The results on the nuclear modification factor of direct photons in d + Au are similar to the results for π^0 or η measurement. Particles from jets coming from hard scatterings are not suppressed in d + Au collisions. The results of direct photons do not show any significant evidence concerning the Cronin effect.

Direct photons in Au + Au collisions at a collision energy of $\sqrt{s}$ = 200 GeV have already been made in 2002. Both, the results in Au + Au and d + Au collisions for direct photons show no suppression for photons with high transverse momentum.
In contrast hadrons like π^0 or η are clearly suppressed in central Au + Au collisions but not in d + Au.
That is a new evidence that jet quenching is a final state effect of hot and dense matter in central $A + A$ collisions with high energy densities and the CGC is no candidate for high-p_{T} particle suppression.

A. Kinematic Variables

To study ion collisions it is useful to choose the kinematic variables in a way that they are subject to simple transformations when changing the reference frame. According to the rules of special relativity a particle is characterized by its *four-momentum*[1]:

$$P^{\mu} = (E, \vec{p}) = (E, p_x, p_y.p_z), \tag{A.1}$$

with the energy E and the usual three-momentum of the particle $\vec{p}$. The absolute value of the four-momentum is called invariant mass m_{inv}. It is the same in all reference frames or invariant under Lorentz transformation:

$$m_{\text{inv}}^2 = P^2 = P^{\mu}P_{\mu} = E^2 - \vec{p}\cdot\vec{p}. \tag{A.2}$$

If a particle is free the invariant mass is identical to its rest mass m_0 and Equation (A.2) becomes the well-known relativistic energy-momentum relation.

The sum of the four-momenta of two colliding particles leads to the definition of the *Mandelstam* variable s:

$$s = (P_1 + P_2)^2, \tag{A.3}$$

with $\sqrt{s}$ determining the center of mass energy of the reaction.

The beam of the colliding particles is usually considered to point into the z-directions. Thus the transverse momentum component p_{T} and the longitudinal component p_{L} can be written as:

$$p_T = p\cdot\sin(\vartheta), \tag{A.4}$$

$$p_L = p\cdot\cos(\vartheta), \tag{A.5}$$

where p is the absolute value of the momentum $|\vec{p}|$ and ϑ is the angle with respect to the beam axis.

The transverse momentum p_{T} is invariant under Lorentz transformation in z-direction, while p_{L} is not invariant. Therefore the dimensionless rapidity y is defined. It is directly related to the transverse velocity $\beta_L = p_{\text{L}}/E$ of a particle:

$$\begin{aligned} y &= \operatorname{atanh}\beta_L \\ &= \frac{1}{2}\ln\left(\frac{E+p_{\text{L}}}{E-p_{\text{L}}}\right). \end{aligned} \tag{A.6}$$

[1] Here, as well as in the following we will use the convention $\hbar = c = 1$.

It has the advantage to be additive under Lorentz transformation into a reference frame that moves at a velocity β with respect to the old reference frame in longitudinal direction:

$$y' = y + \operatorname{atanh}(\beta). \tag{A.7}$$

For this reason the shape of a distribution is independent of the reference frame when it is given in units of the rapidity. The rapidity is connected to the energy of a particle and to its longitudinal momentum via the transverse mass $m_T = \sqrt{{p_T}^2 + m_0^2}$:

$$E = m_T \cdot \cosh(y), \tag{A.8}$$
$$p_L = m_T \cdot \sinh(y). \tag{A.9}$$

In the limit $E \gg m_0$ the rapidity can be approximated by the *pseudo-rapidity* η:

$$\eta = \frac{1}{2} \ln\left(\frac{p + p_L}{p - p_L}\right) \tag{A.10}$$
$$= -\ln\left[\tan\left(\frac{\vartheta}{2}\right)\right]. \tag{A.11}$$

The pseudo-rapidity is only determined by the angle ϑ of the particle direction of motion with respect to the beam axis. For this reason it is usually easier to determine the pseudo-rapidity than the rapidity of a particle. Similar to Equation (A.8) and (A.9) holds:

$$E = p_T \cdot \cosh(\eta), \tag{A.12}$$
$$p_L = p_T \cdot \sinh(\eta). \tag{A.13}$$

B. Lists of Analyzed Runs

69502	69650	69654	70087	70451	70456	72119	72361	72669	74413
74428	74443	74463	74691	74857	74865	74868	75622		

Table B.1: List of runs containing all triggers used in the analysis of the d + Au data.

77531	77521	77520	77414	77415	77394	77391	77392	77390	77380
77374	77322	77313	77312	77266	77255	77247	77252	77096	77094
75549	75747	75983	76274	75365	75377	75379	75399	75401	75403
75532	75533	75547	74855	74857	74865	74868	74405	77547	74448
74463	74660	74662	74664	74844	74852	74854	70092	70093	70094
70073	70074	70075	70076	70078	70083	70087	70088	70090	70091
77533	78810	78817	78838	78839	79047	79048	79050	79066	79067
79340	79341	79343	79560	79579	79603	79615	79621	79622	79624
79626	79628	79629	79630	79632	79641	79642	79643	79644	79740
79749	79750	79753	79762	79764	79765	79863	79872	79873	79875
79885	79888	80151	80158	80161	80172	80304	80312	74443	77678
77683	77686	77688	66304	69649	69650	69652	69654	69656	69657
69658	69659	69709	69717	70072	78207	78181	78035	78033	78025
78553	78632	78578	69648	69502	78808	78633	77530	77389	77320
77314	78034	78179	78030	78029	77687	78205			

Table B.2: List of filtered runs containing only Gamma1 triggers used in the analysis of the d + Au data.

C. Excluded Modules and FEMs

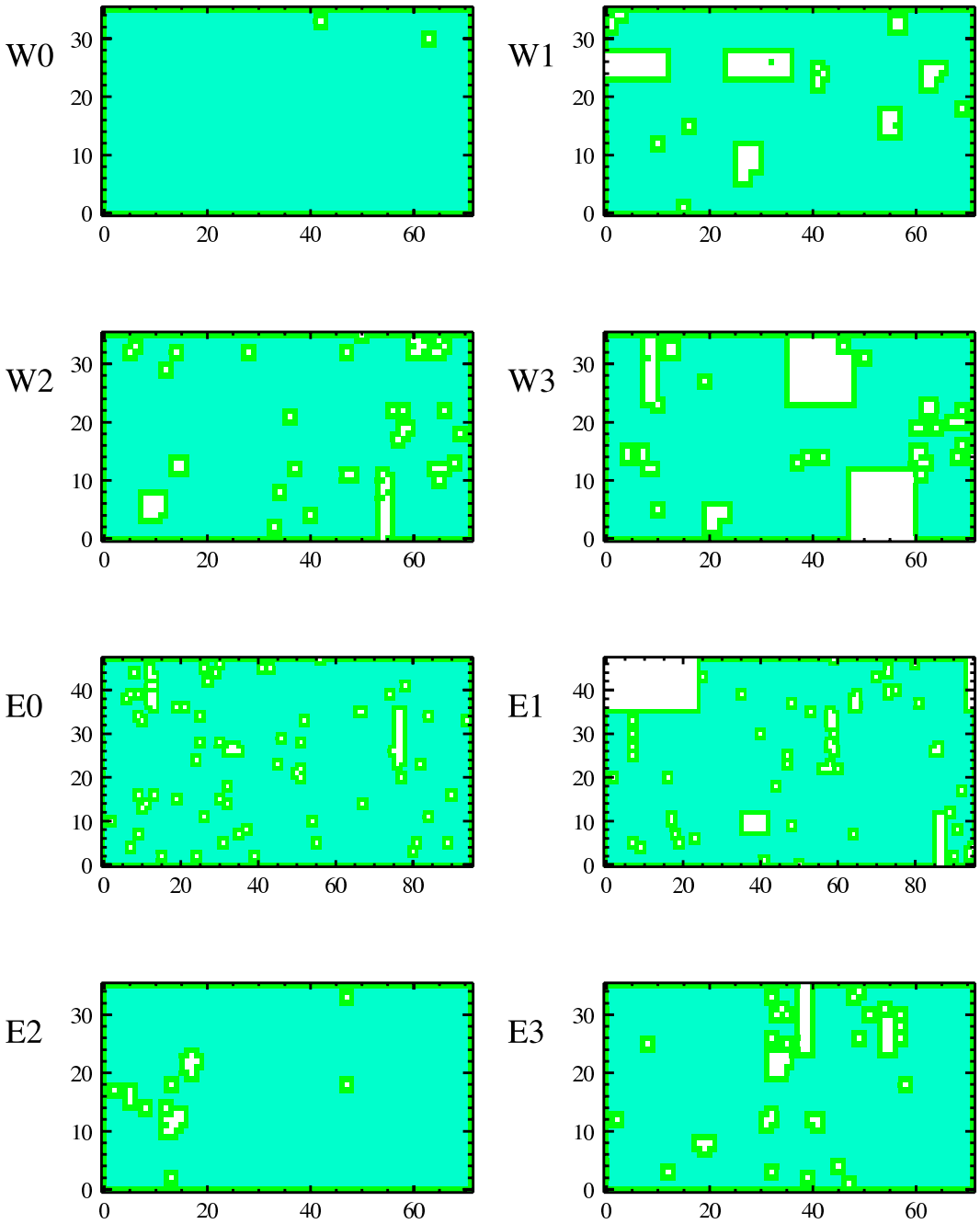

Figure C.1: Mod flagged as eps or dead for the analysis of the d + Au data (white) and the excluded area around it. The regions excluded on the edge of the calorimeter sectors are also shown.

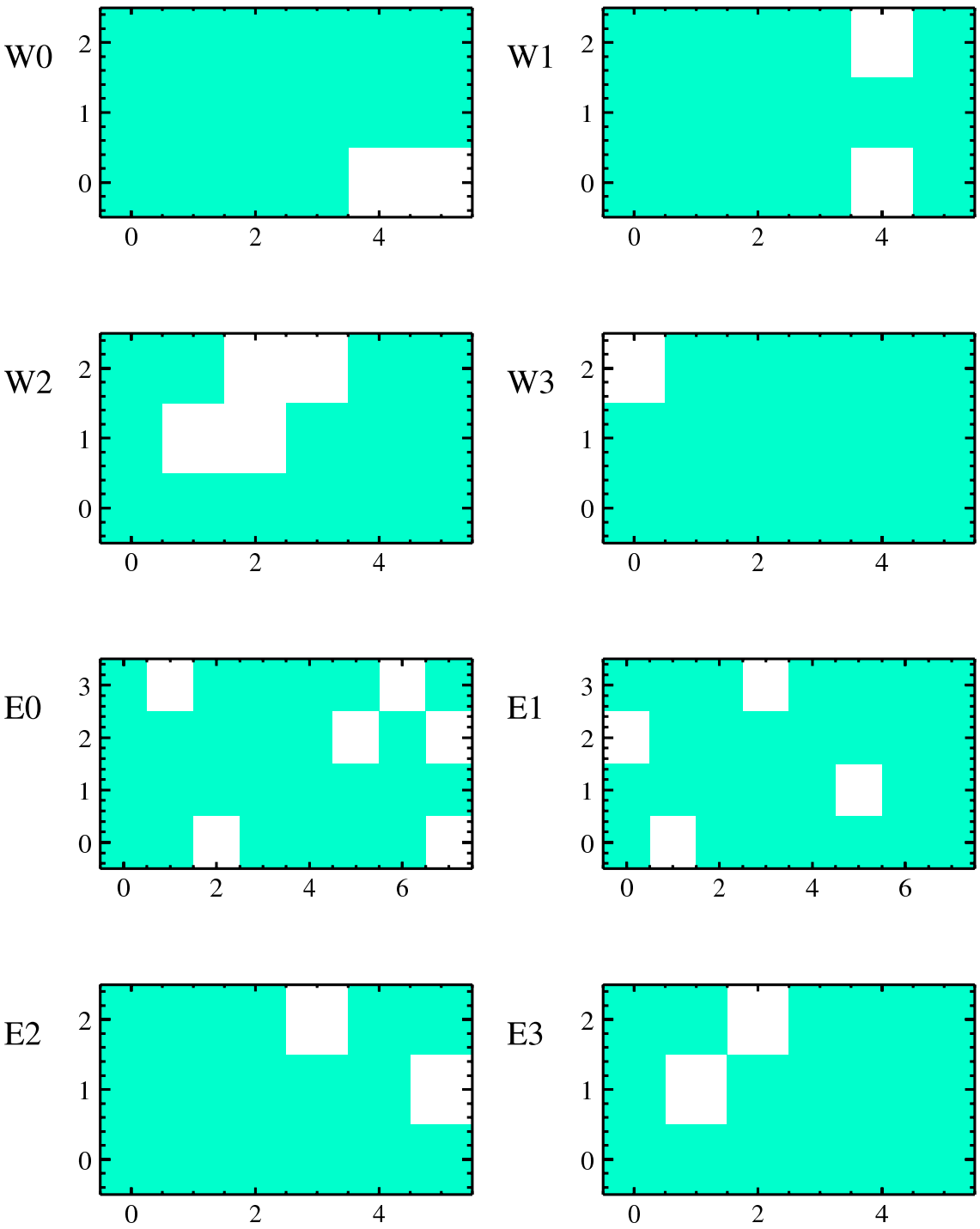

Figure C.2: FEMs masked for the 4×4 ERT trigger during the d + Au run (white)

D. Shift of the Detector Geometry

It is still under discussion if some parts of the detector are shifted in comparison to the previously used values. This would have influence to the acceptance of the detector and would influence the energy-scale, which is calibrated with the π^0 peak.
Evidences of the shift were found, by comparing projections of tracks of identified electrons on the EMCal surface with reconstructed positions of corresponding clusters in the EMCal [Pre05]. Systematic differences between projected and reconstructed positions, increasing with increase of the distance to the center of the sector were found.
An explanation for this observation could be a shift of the detector in *x*- an *y*-position in comparison to the previously used values. The most relevant correction is the correction in *x*-Position as it influences the decay angle between two π^0 decay photons as motivated in Figure D.1.

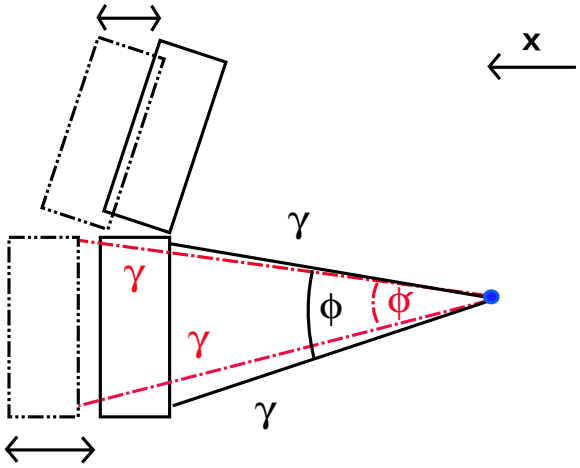

Figure D.1: To evaluate the size of the error on the energy scale the detector is shifted in x-position with the factors $c_{\mathrm{sec}}^{\mathrm{corr}}$ given in Table D.1.

Sector	W0	W1	W2	W3	E0	E1	E2	E3
$c_{\text{sec}}^{\text{corr}}$	1,005	1,004	1,009	1,011	0,996	0,995	1,008	1,010

Table D.1: In the Monte Carlo method implemented correction factors c_{corr} for the shift of the different EMCal sectors.

	PbGl	PbSc
$E_{\text{det}}^{\text{scale}}$	1,004	0,994

Table D.2: In the Monte Carlo method implemented correction factors $E_{\text{det}}^{\text{scale}}$ PbGl and PbSc to correct the energy shift of the π^0-peak.

The position of the EMCal detector is corrected in the Monte Carlo simulation by implementing scaling factors $c_{\text{sec}}^{\text{corr}}$ for each sector given in Table D.1.
As the π^0-peak is used for the calibration of the energy scale, the shifted π^0 peak position influences the energy calibration. This effect is corrected in the Monte Carlo simulation with factors for the energy scale for PbSc and PbGl given in Table D.2. They are calculated by comparing π^0-peak position of a Monte Carlo simulation with uncorrected geometry and the π^0-peak position of a Monte Carlo simulation with corrected geometry. This leads to a shift of the inclusive photon yield of $-3,8\%$ for PbGl and $+2,5\%$ for PbSc. The effect is within the Systematic error of the linear energy scale correction. It would explain a fraction of the difference between PbGl and PbSc measurements.

E. Data Tables

E.1 π^0 Production in d + Au Collisions

p_T (GeV/c)	$\frac{1}{2\pi p_T N_{evt}} \frac{d^2N}{dp_T dy} \left(\frac{c^3}{GeV^2}\right)$	Stat. error	Sys ErrA	Sys ErrB	Sys ErrC
1.25	0.0556121	0.00466198	0.00295809	0.00478731	0
1.75	0.0100588	0.00048603	0.000535044	0.000766098	0
2.25	0.00223794	6.94983e-05	0.000119039	0.000172686	0
2.75	0.000622509	1.56998e-05	3.31122e-05	4.9544e-05	0
3.25	0.000195184	5.64579e-06	1.03821e-05	1.61105e-05	0
3.75	6.99657e-05	2.93564e-06	3.72158e-06	5.99668e-06	0
4.25	2.55854e-05	1.40098e-06	1.36093e-06	2.27545e-06	0
4.75	1.06029e-05	2.26535e-07	5.63984e-07	9.86946e-07	0
5.25	4.44438e-06	1.15796e-07	2.36403e-07	4.23254e-07	0
5.75	2.09006e-06	6.88193e-08	1.11173e-07	2.05292e-07	0
6.25	1.09193e-06	4.0985e-08	5.80813e-08	1.10376e-07	0
6.75	6.30728e-07	2.53842e-08	3.35494e-08	6.5477e-08	0
7.25	3.46852e-07	1.71787e-08	1.84496e-08	3.69087e-08	0
7.75	1.80704e-07	1.17125e-08	9.6119e-09	1.96765e-08	0
8.25	1.17504e-07	9.50789e-09	6.25022e-09	1.3073e-08	0
8.75	6.15381e-08	7.05983e-09	3.2733e-09	6.98606e-09	0
9.25	3.7839e-08	4.47026e-09	2.01271e-09	4.37822e-09	0
9.75	2.84843e-08	3.74676e-09	1.51512e-09	3.35588e-09	0
11	9.53475e-09	9.77316e-10	5.07168e-10	1.17125e-09	0
13	2.60069e-09	4.75361e-10	1.38334e-10	3.40829e-10	0
15	6.19982e-10	2.19959e-10	3.29777e-11	8.75378e-11	0

Table E.1: Minimum bias π^0 yield for PbGl d + Au collisions with analysis class PID3 [Bat03].

p_T (GeV/c)	$\frac{1}{2\pi p_T N_{evt}} \frac{d^2N}{dp_T dy} \left(\frac{c^3}{GeV^2}\right)$	Stat. error	Sys ErrA	Sys ErrB	Sys ErrC
1.25	0.0519649	0.00553366	0.00276409	0.00436932	0
1.75	0.00932233	0.000502476	0.000495868	0.000688841	0
2.25	0.00211517	5.79678e-05	0.000112509	0.000158476	0
2.75	0.000559543	1.25508e-05	2.97629e-05	4.33186e-05	0
3.25	0.000172922	4.08104e-06	9.19798e-06	1.39116e-05	0
3.75	5.91259e-05	1.56689e-06	3.145e-06	4.94872e-06	0
4.25	2.27264e-05	7.77072e-07	1.20885e-06	1.97718e-06	0
4.75	9.03957e-06	1.77701e-07	4.80828e-07	8.2472e-07	0
5.25	3.97702e-06	7.74457e-08	2.11544e-07	3.71565e-07	0
5.75	1.93085e-06	3.66911e-08	1.02705e-07	1.86277e-07	0
6.25	9.90116e-07	2.20324e-08	5.26658e-08	9.84023e-08	0
6.75	4.96945e-07	1.3886e-08	2.64333e-08	5.07668e-08	0
7.25	2.84972e-07	8.28046e-09	1.51581e-08	2.98644e-08	0
7.75	1.62448e-07	6.66221e-09	8.64087e-09	1.74328e-08	0
8.25	1.01627e-07	4.35574e-09	5.40569e-09	1.11499e-08	0
8.75	5.79625e-08	3.47757e-09	3.08311e-09	6.4926e-09	0
9.25	3.54613e-08	2.41479e-09	1.88624e-09	4.05057e-09	0
9.75	2.29008e-08	2.02443e-09	1.21813e-09	2.66475e-09	0
11	9.48729e-09	5.73476e-10	5.04643e-10	1.2384e-09	0
13	2.82222e-09	2.7806e-10	1.50118e-10	4.32176e-10	0
15	9.36782e-10	1.68755e-10	4.98288e-11	1.70134e-10	0

Table E.2: Minimum bias π^0 yield for PbSc d + Au collisions with analysis class PID3 [Bat03].

p_T (GeV/c)	$\frac{1}{2\pi p_T N_{evt}} \frac{d^2N}{dp_T dy} \left(\frac{c^3}{GeV^2}\right)$	Stat. error	Sys ErrA	Sys ErrB	Sys ErrC
1.25	0.0539136	0.00359672	0.00286775	0.0036472	0
1.75	0.00966934	0.000349873	0.000514326	0.000601466	0
2.25	0.00216933	4.47699e-05	0.00011539	0.000138082	0
2.75	0.000586013	9.87224e-06	3.11709e-05	3.86972e-05	0
3.25	0.000182011	3.38147e-06	9.68142e-06	1.24954e-05	0
3.75	6.32824e-05	1.55214e-06	3.36608e-06	5.41435e-06	0
4.25	2.38112e-05	7.48141e-07	1.26655e-06	1.88441e-06	0
4.75	9.67124e-06	1.4063e-07	5.14428e-07	7.46108e-07	0
5.25	4.17314e-06	6.74823e-08	2.21976e-07	3.29353e-07	0
5.75	1.99812e-06	3.72735e-08	1.06283e-07	1.62173e-07	0
6.25	1.03194e-06	2.20911e-08	5.48903e-08	8.5979e-08	0
6.75	5.43782e-07	1.32458e-08	2.89246e-08	4.65308e-08	0
7.25	3.06832e-07	8.61961e-09	1.63208e-08	2.68001e-08	0
7.75	1.6945e-07	6.32368e-09	9.01331e-09	1.50732e-08	0
8.25	1.0692e-07	4.62509e-09	5.68721e-09	9.69016e-09	0
8.75	5.91438e-08	3.50462e-09	3.14595e-09	5.44476e-09	0
9.25	3.62729e-08	2.30887e-09	1.92941e-09	3.39378e-09	0
9.75	2.45363e-08	1.87214e-09	1.30512e-09	2.33712e-09	0
11	9.50704e-09	5.42885e-10	5.05694e-10	9.50199e-10	0
13	2.7366e-09	2.59582e-10	1.45564e-10	2.93666e-10	0
15	7.96764e-10	1.3652e-10	4.23811e-11	9.04788e-11	0

Table E.3: Minimum bias π^0 yield for EmCal d + Au collisions with analysis class PID3.

E.2 Inclusive Photon Production in d + Au Collisions

p_T (GeV/c)	$\frac{1}{2\pi p_T N_{evt}} \frac{d^2N}{dp_T dy} \left(\frac{c^3}{GeV^2}\right)$	Stat. error	Sys ErrA	Sys ErrB	Sys ErrC
1.25	0.0341371	0.000175516	0	0.00230852	0.000682741
1.75	0.00513714	2.9662e-05	0	0.000346263	0.000102743
2.25	0.00103039	7.85929e-06	0	7.22859e-05	2.06078e-05
2.75	0.000271676	3.09997e-06	0	2.03294e-05	5.43352e-06
3.25	7.95697e-05	1.44599e-06	0	6.4082e-06	1.59139e-06
3.75	2.76208e-05	7.75161e-07	0	2.39296e-06	5.52415e-07
4.25	9.18413e-06	4.12067e-07	0	8.51582e-07	1.83683e-07
4.75	3.90618e-06	2.57199e-07	0	3.84961e-07	7.81236e-08
5.25	1.86012e-06	2.78973e-08	0	2.294e-07	1.00171e-07
5.75	8.8106e-07	1.77215e-08	0	1.10345e-07	4.74465e-08
6.25	4.67291e-07	1.22181e-08	0	5.96341e-08	2.51644e-08
6.75	2.49375e-07	8.56051e-09	0	3.24517e-08	1.34293e-08
7.25	1.42017e-07	6.17548e-09	0	1.88318e-08	7.64786e-09
7.75	8.5348e-08	4.65525e-09	0	1.15159e-08	4.59613e-09
8.25	5.50256e-08	3.64666e-09	0	7.54225e-09	2.96322e-09
8.75	3.30122e-08	2.72787e-09	0	4.58905e-09	1.77776e-09
9.25	1.98692e-08	2.05181e-09	0	2.79704e-09	1.06999e-09
9.75	1.21332e-08	1.56759e-09	0	1.72757e-09	6.53395e-10
11	6.33388e-09	5.24441e-10	0	9.25007e-10	3.4109e-10
13	1.31009e-09	2.21471e-10	0	1.99922e-10	7.05506e-11
15	4.61624e-10	1.2338e-10	0	7.55245e-11	2.48592e-11

Table E.4: Minimum bias inclusive photon yield for PbGl d + Au collisions with analysis class PID3.

p_T (GeV/c)	$\frac{1}{2\pi p_T N_{evt}} \frac{d^2N}{dp_T dy} \left(\frac{c^3}{GeV^2}\right)$	Stat. error	Sys ErrA	Sys ErrB	Sys ErrC
1.25	0.0298764	8.81747e-05	0	0.00202039	0.000597528
1.75	0.00444393	1.4605e-05	0	0.000299538	8.88786e-05
2.25	0.000910142	3.92793e-06	0	6.385e-05	1.82028e-05
2.75	0.000224114	1.48804e-06	0	1.67703e-05	4.48227e-06
3.25	6.51938e-05	6.93939e-07	0	5.25043e-06	1.30388e-06
3.75	2.22149e-05	3.69732e-07	0	1.92462e-06	4.44298e-07
4.25	8.68891e-06	2.20789e-07	0	8.05663e-07	1.73778e-07
4.75	3.33107e-06	1.27917e-07	0	3.28283e-07	6.66214e-08
5.25	1.55702e-06	1.32913e-08	0	1.9202e-07	8.38482e-08
5.75	7.38346e-07	8.5296e-09	0	9.24712e-08	3.97611e-08
6.25	3.78259e-07	5.7905e-09	0	4.82721e-08	2.03699e-08
6.75	2.07357e-07	4.10863e-09	0	2.69838e-08	1.11665e-08
7.25	1.11885e-07	2.9052e-09	0	1.48362e-08	6.0252e-09
7.75	6.58962e-08	2.16242e-09	0	8.89131e-09	3.54862e-09
8.25	4.21636e-08	1.67774e-09	0	5.77928e-09	2.27058e-09
8.75	2.77617e-08	1.31999e-09	0	3.85917e-09	1.49501e-09
9.25	1.71698e-08	1.01123e-09	0	2.41704e-09	9.24624e-10
9.75	1.15445e-08	8.08983e-10	0	1.64375e-09	6.21691e-10
11	4.28215e-09	2.27359e-10	0	6.25371e-10	2.30601e-10
13	1.27836e-09	1.15281e-10	0	1.9508e-10	6.8842e-11
15	3.49471e-10	5.6694e-11	0	5.71755e-11	1.88196e-11

Table E.5: Minimum bias inclusive photon yield for PbSc d + Au collisions with analysis class PID3.

p_T (GeV/c)	$\frac{1}{2\pi p_T N_{evt}} \frac{d^2N}{dp_T dy} \left(\frac{c^3}{GeV^2}\right)$	Stat. error	Sys ErrA	Sys ErrB	Sys ErrC
1.25	0.0316506	9.31804e-05	0	0.0023406	0.000633012
1.75	0.00473566	1.57132e-05	0	0.00036378	9.47132e-05
2.25	0.000962534	4.22011e-06	0	7.74242e-05	1.92507e-05
2.75	0.000243247	1.61081e-06	0	2.05222e-05	4.86495e-06
3.25	7.08667e-05	7.47199e-07	0	6.24108e-06	1.41733e-06
3.75	2.42557e-05	3.94924e-07	0	2.22022e-06	4.85113e-07
4.25	8.90581e-06	2.25573e-07	0	8.40121e-07	1.78116e-07
4.75	3.54188e-06	1.31554e-07	0	3.4454e-07	7.08375e-08
5.25	1.67765e-06	1.44238e-08	0	1.67574e-07	3.3553e-08
5.75	7.9466e-07	9.16427e-09	0	8.11763e-08	1.58932e-08
6.25	4.11552e-07	6.19735e-09	0	4.29276e-08	8.23104e-09
6.75	2.23356e-07	4.3793e-09	0	2.36839e-08	4.46713e-09
7.25	1.22425e-07	3.06821e-09	0	1.32066e-08	2.4485e-09
7.75	7.23757e-08	2.27347e-09	0	7.91937e-09	1.44751e-09
8.25	4.62954e-08	1.7582e-09	0	5.12721e-09	9.25908e-10
8.75	2.9589e-08	1.36487e-09	0	3.29924e-09	5.9178e-10
9.25	1.8095e-08	1.02835e-09	0	2.03417e-09	3.61901e-10
9.75	1.17568e-08	8.07601e-10	0	1.32966e-09	2.35135e-10
11	4.81711e-09	2.34443e-10	0	5.63419e-10	9.63422e-11
13	1.28919e-09	1.12899e-10	0	1.52887e-10	2.57838e-11
15	3.7428e-10	5.41783e-11	0	4.67265e-11	7.48561e-12

Table E.6: Minimum bias inclusive photon yield for EmCal d + Au collisions with analysis class PID3.

E.3 Direct Photon Yield in d + Au Collisions

p_T $\left(\frac{\text{GeV}}{c}\right)$	$\frac{1}{2\pi p_T N_{\text{evt}}} \frac{d^2N}{dp_T dy}$ $\left(\frac{c^3}{\text{GeV}^2}\right)$	low Stat. err.	high Stat. err.	Sys ErrA	low Sys ErrB	high Sys ErrB	Sys ErrC
5.25	3.25517e-07	4.78141e-08	4.50532e-08	0	1.89999e-07	1.53279e-07	3.72024e-08
5.75	1.67991e-07	2.88163e-08	2.67058e-08	0	8.84632e-08	7.14436e-08	1.76212e-08
6.25	8.16236e-08	1.86103e-08	1.70046e-08	0	4.77475e-08	3.85188e-08	9.34582e-09
6.75	3.18376e-08	1.21989e-08	1.09836e-08	0	2.68108e-08	2.1576e-08	4.98751e-09
7.25	2.09183e-08	8.59278e-09	7.54289e-09	0	1.49494e-08	1.20412e-08	2.84034e-09
7.75	2.3185e-08	5.89071e-09	5.01674e-09	0	7.83456e-09	6.37943e-09	1.70696e-09
8.25	1.34758e-08	4.93484e-09	4.03434e-09	0	5.20353e-09	4.2233e-09	1.10051e-09
8.75	1.1854e-08	3.61908e-09	2.79793e-09	0	2.75183e-09	2.27518e-09	6.60243e-10
9.25	6.82245e-09	2.52831e-09	1.9046e-09	0	1.68485e-09	1.38839e-09	3.97384e-10
9.75	2.31769e-09	2.23896e-09	1.55708e-09	0	1.21777e-09	9.83508e-10	2.42665e-10
11	3.16555e-09	5.4763e-10	4.52509e-10	0	4.58631e-10	3.95743e-10	1.26678e-10
13	4.53731e-10	2.94071e-10	1.87149e-10	0	1.10732e-10	9.13037e-11	2.62018e-11
15	2.60484e-10	1.75176e-10	9.31358e-11	0	3.17776e-11	2.81651e-11	9.23248e-12

Table E.7: Significant minimum bias direct photon yield for PbGl d + Au collisions with analysis class PID3.

p_T $\left(\frac{\text{GeV}}{c}\right)$	$\frac{1}{2\pi p_T N_{\text{evt}}} \frac{d^2N}{dp_T dy}$ $\left(\frac{c^3}{\text{GeV}^2}\right)$	low Stat. err.	high Stat. err.	Sys ErrA	low Sys ErrB	high Sys ErrB	Sys ErrC
6.25	4.27194e-08	-1.02293e-08	1.02293e-08	0	4.24095e-08	3.40853e-08	7.56518e-09
6.75	2.72441e-08	-7.13364e-09	7.13364e-09	0	2.15126e-08	1.734e-08	4.14715e-09
7.25	1.28334e-08	-4.37429e-09	4.37429e-09	0	1.21074e-08	9.74113e-09	2.2377e-09
7.75	8.92016e-09	-3.47789e-09	3.47789e-09	0	6.85914e-09	5.5278e-09	1.31792e-09
8.25	7.67346e-09	-2.48231e-09	2.48231e-09	0	4.33029e-09	3.4923e-09	8.43271e-10
8.75	6.63594e-09	-2.15909e-09	2.15909e-09	0	2.50109e-09	2.04138e-09	5.55233e-10
9.25	3.57911e-09	-1.57299e-09	1.57299e-09	0	1.54821e-09	1.26349e-09	3.43397e-10
9.75	3.0544e-09	-1.33161e-09	1.33161e-09	0	9.78748e-10	8.06562e-10	2.3089e-10
11	1.20801e-09	-3.50778e-10	3.50778e-10	0	3.85064e-10	3.14366e-10	8.56431e-11
13	5.31624e-10	-1.74913e-10	1.74913e-10	0	1.1009e-10	9.04699e-11	2.55673e-11
15	1.32666e-10	-8.5812e-11	8.5812e-11	0	3.32029e-11	2.69359e-11	6.98941e-12

Table E.8: Significant minimum bias direct photon yield for PbSc d + Au collisions with analysis class PID3.

p_T $\left(\frac{\text{GeV}}{c}\right)$	$\frac{1}{2\pi p_T N_{\text{evt}}} \frac{\mathrm{d}^2 N}{\mathrm{d}p_T \mathrm{d}y} \left(\frac{c^3}{\text{GeV}^2}\right)$	low Stat. err.	high Stat. err.	Sys ErrA	low Sys ErrB	high Sys ErrB	Sys ErrC
5.25	1.57072e-07	-3.31344e-08	3.31344e-08	0	1.71674e-07	1.38039e-07	3.11404e-08
5.75	6.98088e-08	-1.6434e-08	1.6434e-08	0	8.34689e-08	6.70732e-08	1.47669e-08
6.25	4.27194e-08	-1.02293e-08	1.02293e-08	0	4.24095e-08	3.40853e-08	7.56518e-09
6.75	2.72441e-08	-7.13364e-09	7.13364e-09	0	2.15126e-08	1.734e-08	4.14715e-09
7.25	1.28334e-08	-4.37429e-09	4.37429e-09	0	1.21074e-08	9.74113e-09	2.2377e-09
7.75	8.92016e-09	-3.47789e-09	3.47789e-09	0	6.85914e-09	5.5278e-09	1.31792e-09
8.25	7.67346e-09	-2.48231e-09	2.48231e-09	0	4.33029e-09	3.4923e-09	8.43271e-10
8.75	6.63594e-09	-2.15909e-09	2.15909e-09	0	2.50109e-09	2.04138e-09	5.55233e-10
9.25	3.57911e-09	-1.57299e-09	1.57299e-09	0	1.54821e-09	1.26349e-09	3.43397e-10
9.75	3.0544e-09	-1.33161e-09	1.33161e-09	0	9.78748e-10	8.06562e-10	2.3089e-10
11	1.20801e-09	-3.50778e-10	3.50778e-10	0	3.85064e-10	3.14366e-10	8.56431e-11
13	5.31624e-10	-1.74913e-10	1.74913e-10	0	1.1009e-10	9.04699e-11	2.55673e-11
15	1.32666e-10	-8.5812e-11	8.5812e-11	0	3.32029e-11	2.69359e-11	6.98941e-12

Table E.9: Significant minimum bias direct photon yield for EmCal d + Au collisions with analysis class PID3.

E.4 R_{dAu} of Direct Photons in d + Au Collisions

p_T $\left(\frac{\text{GeV}}{c}\right)$	R_{dAu}	low Stat. error	high Stat. error	low Sys ErrB	high Sys ErrB
5.25	2.26764	0.313853	0.333086	1.32358	1.06778
5.75	1.96793	0.312845	0.337569	1.0363	0.836926
6.25	1.55062	0.32304	0.353544	0.907069	0.731751
6.75	0.948825	0.327333	0.363553	0.799016	0.64301
7.25	0.950884	0.342877	0.390602	0.679555	0.547358
7.75	1.56912	0.339523	0.398672	0.530228	0.431747
8.25	1.32854	0.397733	0.486511	0.513	0.416362
8.75	1.67207	0.394664	0.510492	0.388161	0.320926
9.25	1.35494	0.378255	0.502123	0.334611	0.275735
9.75	0.637646	0.428385	0.615985	0.335035	0.270584
11	1.88851	0.23096	0.27951	0.273611	0.236094
13	0.803484	0.289342	0.454649	0.196089	0.161684
15	1.21257	0.3835	0.721314	0.147927	0.131111

Table E.10: Significant minimum bias direct photon R_{dAu} data pionts made with pQCD calculation as reference for PbGl with analysis class PID3.

$p_T\ (\frac{\text{GeV}}{c})$	R_{dAu}	low Stat. error	high Stat. error	low Sys ErrB	high Sys ErrB
6.25	0.63349	0.172594	0.182147	0.628893	0.505454
6.75	0.993084	0.172905	0.185017	0.784161	0.632065
7.25	0.618439	0.168331	0.181863	0.583453	0.469423
7.75	0.703103	0.188881	0.209526	0.54065	0.435711
8.25	0.706639	0.19269	0.216146	0.398771	0.321602
8.75	1.12979	0.205275	0.237134	0.425819	0.347551
9.25	0.981125	0.208767	0.247157	0.424404	0.346356
9.75	1.09115	0.224762	0.27591	0.349647	0.288135
11	0.741355	0.120327	0.139848	0.236313	0.192926
13	0.745414	0.166856	0.212611	0.154362	0.126852
15	0.391548	0.22048	0.354134	0.0979945	0.0794979

Table E.11: Significant minimum bias direct photon R_{dAu} data pionts made with pQCD calculation as reference for PbSc with analysis class PID3.

$p_T\ (\frac{\text{GeV}}{c})$	R_{dAu}	low Stat. error	high Stat. error	low Sys ErrB	high Sys ErrB
5.25	1.00282	0.219271	0.214727	0.564497	0.512767
5.75	0.676187	0.206839	0.202405	0.440914	0.39767
6.25	0.773036	0.200055	0.195815	0.385007	0.348464
6.75	0.713557	0.202769	0.198371	0.336178	0.304354
7.25	0.617711	0.200218	0.195895	0.286514	0.259139
7.75	0.643739	0.241435	0.232945	0.263119	0.238862
8.25	0.821149	0.24303	0.235693	0.26464	0.242682
8.75	0.921893	0.314125	0.296003	0.257097	0.237653
9.25	0.743923	0.32751	0.305926	0.22424	0.206742
9.75	0.682155	0.349835	0.323905	0.210062	0.193985
11	0.909034	0.17697	0.168476	0.228028	0.214543
13	0.947881	0.217327	0.208168	0.217182	0.208441
15	0.741218	0.294283	0.269727	0.18916	0.183285

Table E.12: Significant minimum bias direct photon R_{dAu} data pionts made with pQCD calculation as reference for EmCal with analysis class PID3.

$p_T\ (\frac{\text{GeV}}{c})$	R_{dAu}	low Stat. error	high Stat. error	low Sys ErrB	high Sys ErrB
5.25	3.56613	0.49357	0.523817	2.08149	1.67921
5.75	2.30702	0.36675	0.395734	1.21486	0.981134
6.25	1.68894	0.351857	0.385082	0.987984	0.797026
6.75	1.20386	0.415318	0.461274	1.01379	0.815847
7.25	1.04735	0.377663	0.43023	0.748498	0.602889
7.75	1.60864	0.348074	0.408713	0.543582	0.442622
8.25	2.25072	0.673814	0.824215	0.869091	0.705374
8.75	2.36974	0.559336	0.723491	0.550118	0.454831
9.25	1.39501	0.38944	0.516971	0.344506	0.283889
9.75	0.843646	0.566781	0.814986	0.443273	0.358
11	1.42954	0.20435	0.247306	0.207115	0.178715
13	0.624576	0.257617	0.4048	0.152427	0.125683
15	0.883274	0.315813	0.594003	0.107755	0.0955048

Table E.13: Significant minimum bias direct photon R_{dAu} data pionts made with p + p analysis [Zau05] as reference for PbGl with analysis class PID3.

$p_T\ (\frac{\text{GeV}}{c})$	R_{dAu}	low Stat. error	high Stat. error	low Sys ErrB	high Sys ErrB
6.75	1.65658	0.288426	0.308631	1.06946	0.862029
7.25	2.65581	0.722876	0.780985	2.36348	1.90156
7.75	0.77863	0.209171	0.232033	0.51408	0.414298
8.25	0.948998	0.258778	0.290279	0.573328	0.462379
8.75	3.30948	0.601309	0.694634	1.03343	0.843481
9.25	1.96833	0.418828	0.495846	0.616856	0.503416
9.75	2.42037	0.498563	0.612019	0.5973	0.492219
11	1.18764	0.22531	0.261862	0.368011	0.300444
13	2.73044	0.700055	0.892022	0.714106	0.586838
15	0.358437	0.228178	0.366499	0.141492	0.114785

Table E.14: Significant minimum bias direct photon R_{dAu} data pionts made with p + p analysis [Zau05] as reference for PbSc with analysis class PID3.

p_T $\left(\frac{\text{GeV}}{c}\right)$	R_{dAu}	low Stat. error	high Stat. error	low Sys ErrB	high Sys ErrB
5.25	1.85319	0.405206	0.396808	1.04317	0.947578
5.75	1.30675	0.39972	0.391151	0.852076	0.768506
6.25	1.55257	0.401792	0.393276	0.773249	0.699856
6.75	0.99294	0.28216	0.276041	0.467803	0.423519
7.25	1.59929	0.518375	0.507185	0.741802	0.670927
7.75	0.680429	0.255196	0.246222	0.278115	0.252476
8.25	1.10708	0.327656	0.317764	0.356791	0.327186
8.75	2.19513	0.747967	0.704816	0.612175	0.565878
9.25	1.23328	0.542947	0.507165	0.371745	0.342737
9.75	1.31343	0.673574	0.623649	0.404455	0.373499
11	1.21746	0.277034	0.263738	0.305395	0.287334
13	2.38669	0.626775	0.600361	0.546847	0.524838
15	0.646255	0.290069	0.265863	0.164925	0.159803

Table E.15: Significant minimum bias direct photon R_{dAu} data pionts made with p + p analysis [Zau05] as reference for EmCal with analysis class PID3.

F. NLO pQCD results for direct photons in p + p collisions

For the comparison of the direct photon production in d + Au to the expectation from hard scattering a NLO pQCD calculation of p + p collisions form W. Vogelsang is used. In particular, the employed parameter set is the same that showed the best agreement with the π^0 measurement: The invariant cross section for direct photon production in p + p collisions at $\sqrt{s} = 200\,\mathrm{GeV}$ is calculated for three different scales $\mu = \mu_{\mathrm{fac}} = \mu_{\mathrm{rat}} = \mu_{\mathrm{fra}}$[1]: $2p_{\mathrm{T}}$, p_{T} and $p_{\mathrm{T}}/2$, where the particle distribution function is given by [Pum02] and the parton fragmentation functions into photons by [Glu93] (CTEQ06M). The cross section is divided into the contribution from photons directly produced in hard scatterings and in those from fragmentation of hard-scattered partons. To obtain the invariant yield, the cross section is divided by the total inelastic cross section $\sigma_{in} = 42.2\,\mathrm{mb}$ for p + p at $\sqrt{s} = 200\,\mathrm{GeV}$.

p_{T} (GeV/c)	$E \cdot \frac{\mathrm{d}^3\sigma}{\mathrm{d}p^3}$ $\left(\frac{\mathrm{mb}c^3}{\mathrm{GeV}^2}\right)$		
	Total	Direct	Fragmentation
1.25	1.534E-01	3.357E-02	1.199E-01
1.75	2.793E-02	9.253E-03	1.867E-02
2.25	7.520E-03	3.057E-03	4.464E-03
2.75	2.589E-03	1.179E-03	1.410E-03
3.25	1.046E-03	5.148E-04	5.312E-04
3.75	4.740E-04	2.476E-04	2.264E-04
4.25	2.367E-04	1.287E-04	1.080E-04
4.75	1.263E-04	7.112E-05	5.518E-05
5.25	7.154E-05	4.136E-05	3.018E-05
5.75	4.247E-05	2.509E-05	1.738E-05
6.25	2.620E-05	1.576E-05	1.044E-05
6.75	1.674E-05	1.020E-05	6.534E-06
7.50	9.108E-06	5.654E-06	3.451E-06
8.50	4.252E-06	2.703E-06	1.548E-06
9.50	2.143E-06	1.387E-06	7.563E-07
11.00	8.774E-07	5.787E-07	2.987E-07
13.50	2.358E-07	1.599E-07	7.585E-08

Table F.1: Differential cross section for the direct photon production in p + p collisions from NLO pQCD ($\mu = p_{\mathrm{T}}$).

[1] Were μ_{fac} is the factorization scale, μ_{rat} the renormalization scale and μ_{fra} the fragmentation scale.

p_T (GeV/c)	$E \cdot \frac{d^3\sigma}{dp^3}$ $\left(\frac{mb c^3}{GeV^2}\right)$		
	Total	Direct	Fragmentation
1.25	1.250E-01	2.471E-02	1.003E-01
1.75	2.299E-02	6.912E-03	1.608E-02
2.25	6.167E-03	2.290E-03	3.877E-03
2.75	2.147E-03	8.911E-04	1.257E-03
3.25	8.761E-04	3.933E-04	4.827E-04
3.75	3.994E-04	1.907E-04	2.087E-04
4.25	2.002E-04	9.983E-05	1.003E-04
4.75	1.072E-04	5.552E-05	5.170E-05
5.25	6.052E-05	3.236E-05	2.816E-05
5.75	3.581E-05	1.969E-05	1.612E-05
6.25	2.205E-05	1.241E-05	9.636E-06
6.75	1.405E-05	8.048E-06	6.006E-06
7.50	7.645E-06	4.476E-06	3.172E-06
8.50	3.580E-06	2.146E-06	1.434E-06
9.50	1.798E-06	1.104E-06	6.944E-07
11.00	7.333E-07	4.618E-07	2.716E-07
13.50	1.970E-07	1.279E-07	6.903E-08

Table F.2: Differential cross section for the direct photon production in p + p collisions from NLO pQCD ($\mu = 2p_T$).

p_T (GeV/c)	$E \cdot \frac{d^3\sigma}{dp^3}$ $\left(\frac{mb c^3}{GeV^2}\right)$		
	Total	Direct	Fragmentation
1.25	9.620E-01	5.126E-02	9.107E-01
1.75	5.330E-02	1.453E-02	3.877E-02
2.25	1.139E-02	4.875E-03	6.517E-03
2.75	3.597E-03	1.837E-03	1.759E-03
3.25	1.414E-03	7.959E-04	6.179E-04
3.75	6.288E-04	3.771E-04	2.517E-04
4.25	3.094E-04	1.927E-04	1.168E-04
4.75	1.636E-04	1.048E-04	5.879E-05
5.25	9.103E-05	5.995E-05	3.104E-05
5.75	5.345E-05	3.584E-05	1.761E-05
6.25	3.268E-05	2.222E-05	1.045E-05
6.75	2.071E-05	1.422E-05	6.484E-06
7.50	1.117E-05	7.768E-06	3.401E-06
8.50	5.161E-06	3.654E-06	1.508E-06
9.50	2.579E-06	1.848E-06	7.312E-07
11.00	1.056E-06	7.625E-07	2.929E-07
13.50	2.830E-07	2.074E-07	7.560E-08

Table F.3: Differential cross section for the direct photon production in p + p collisions from NLO pQCD ($\mu = p_T/2$).

Bibliography

[Ack03] K.H. Ackermann et. al., Nuclear Instrumental Methods **A 499** (2003) 624.

[Ada03] M. Adamczyk et. al., Nuclear Instrumental Methods **A 499** (2003) 437.

[Adc03] K. Adcox et. al., Nuclear Instrumental Methods **A 499** (2003) 469.

[Adc03] K. Adcox et. al., Nuclear Instrumental Methods **A 499** (2003) 489.

[Adl03a] S.S. Adler et. al., Phys. Rev. Lett. **91** (2003) 072301.

[Aki03] H. Akikawa et al. Nucl. Instrum. Meth. **A 499** (2003) 537.

[Aph03] L. Aphecetche et al. Nucl. Instrum. Meth.**A 499** (2003) 521.

[Aiz03] M. Aizawa et al. Nucl. Instrum. Meth. **A 499** (2003) 508.

[All03] M.Allen et. al., Nuclear Instrumental Methods **A 499** (2003)508

[Aur98] P. Aurenche et. al. *Phys. Rev.* **D58** (1998) 085003.

[Arn01] P. Arnold, G.D. Moor, and L.G. Yaffe. JHEP **12** (2001) 480.

[Aro03] S.H.Aronson et. al., Nuclear Instrumental Methods **A 499** (2003) 480

[Bac03] B.B. Back et. al., Nucl. Instrum. Meth. **A 499** (2003) 603.

[Bat03] L. Aphecetche et. al., *Neutral Pion Spectra measured with the EMCal in* $\sqrt{s_N N}$ *= 200 GeV d + Au-Collisions*, **An203**, 2003.

[Bai95] R. Baier, Yu. L. Dokshitzer, S. Peigné and D. Schiff, Phys. Lett. **B 345** (1995) 277.

[Bai97] R. Baier, Yu. L. Dokshitzer, A. H. Müller, et. al. *Nucl. Phys.* **B 483** (1997) 291.

[Bou76] M. Bourquin and J. M. Gaillard. *Nucl. Phys.* **B 114** (1976) 334.

[Cas98] C. Caso et al., Eur. Phys. J. **C3** (1998) 1.

[Chi02] M. Chiu, G. David, J. Frantz, et al. *EMCal Calibration in Preparation for QM 2002*. PHENIX Internal Technical Note **An400**, 2002.

[Col85] J. C. Collins, D. E. Soper, and G. Sterman. *Nucl. Phys.* **B261** (1985) 104.

[Cro75] J. W. Cronin et al., Phys. Rev. **D 11** (1975) 3105

[Dum01] A. Dumitru et al., Phys. Rev., *Nuclear broadening effects on hard prompt photons at relativistic energies,* **C 64** (2001) 054909.

[Eid04] S. Eidelman et al., Physics Letters **B592** (2004) 1+.

[Ent04] D. d'Enterria et. al., *Photon and π_0 efficiency losses due to photon conversions in PHENIX central-arms for Run 1-3,* PHENIX analysis note **An322**, 2004.

[Fra04] J. Frantz et. al. *Run2 π^0 and Direct Photon Analysis Note,* PHENIX Analysis Note **An280**, 2004.

[Fro61] M. Friossart. *Phys. Rev.* **123** (1961) 65.

[Fis06] Wolfgang Fischer, *RUN OVERVIEW OF THE RELATIVISTIC HEAVY ION COLLIDER*, http://www.agsrhichome.bnl.gov/RHIC/Runs/, 2006.

[Glu93] M.Gluck, E.Reya and A. Vogt. *Phys. Rev.* **D48** (1993) 116.

[Gyu90] M. Gyulassy and M. Plumer. *Phys. Lett.* **B243** (1990) 432.

[Gyu00] M. Gyulassy and P. Levai et al. *Phys. Rev. Lett.* **85** (2000) 5535.

[Har96] J. W. Harris und B. Müller, Ann. Rev. Nucl. Part. Sci. **46** (1996) 71.

[Ian03] E. Icancu and R. Venugolpalan. *The Color Glass Condensate and High Energy Scattering in QCD.* hep-ph/0303204, 2003.

[IKP06] http://qgp.uni-muenster.de/AGWessels/index.php?msel=Arbeitsgruppe&subsel=Publikationen

[Kar88] F. Karsch, *Z. Phys.* **C38** (1988) 147.

[Kar02] F. Karsch, *Lect. Notes Phys.* **583** (2002) 209.

[Kau04] M. Kaufman and D. d'Enterria. *Systematics of η/π^0 at High p_T in Hadronic Collisions*. PHENIX internal Analysis Note **An337**, 2004.

[Kap91] J. Kapusta et al.,*Phys. Ref.* **D44** (1991) 2774.

[KB00] C. Klein-Bösing. *Simulation der Detektoreigenschaften des Bleiglaskalorimeters in den Experimenten WA98 und PHENIX,* Diplomarbeit, Institut für Kernphysik, Universität Münster, 2000.

[KB04] C. Klein-Bösing. *Production of Neutral Pions and Direct Photons in Ultra Relativistic Au + Au Collusions,* Dissertation, Institut für Kernphysik, Universität Münster, 2004.

[Kha03] D. Kharzeev, E. Levin and L. McLerran, Phys. Lett. **B561** (2003) 93.

[Kel00] S. Kelly, D. Morrison, J. Nagle, et al. *Calculation of the Number of Participating Nucleons for Centrality Classes Defined with the ZDC and BBC.* PHENIX Internal Analysis Note 33, 2000.

[Lev03] P. Levai, G. Papp, G. G. Barnafoldi, et al. *Pion Production in d+Au Collisions at RHIC Energy.* nucl-th/0306019, 2003.

[Mig56] A. B. Migdal. *Phys. Rev.* **103 6** (1956) 1811.

[Mul06] B. Müller and J. L. Nagel, *Results from the Relativistic Heavy Ion Collider*, Annu. Rev. Nucl. and Part. Phys., 2006 1.

[Neu95] S. Neumaier et al., Nucl. Instr. and Meth. **A 360** (1995) 593.

[Pau05] P. Stankus. *Direct Photon Production in Relativistic Heavy-Ion Collisions* Oak Ridge National Laboratory, Oak Ridge, Tennessee, 2005.

[Pei97] T. Peitzmann, *Kernmaterie unter extremen Bedingungen – Die experimentelle Suche nach dem Quark-Gluon-Plasma –*, Habilitationsschrift, Institut für Kernphysik, Münster, 1997.

[Pei02] T. Peitzmann and M. H. Thoma *Phys. Rept.* **364** (2002) 175.

[Per98] D.H. Perkins, *Introduction to High Energy Physics,* Addison-Wesley, 1998.

[Pil00] G. Piller and W. Weise. *Phys. Rept.* **330** (2000) 1.

[Pum02] J. Pumplin et al. JHEP **07** (2002) 012.

[Pre05] D. Peressounko et al., *Influence of EMCAL misalignment on photon,* π^0 *and* η *spectra.* PHENIX internal note **An377**, 2005.

[Rey03] K. Reygers, *Fast Monte Carlo Simulation for* π^0 *and Photon Analysis,* PHENIX CVS Repository offline/analysis/PbGl/gampi0v2/acceptance/,2003.

[Rey05] K. Reygers, Ch. Klein-Bösing, T. Awes, S. Bathe, H. Büsching ,*Direct Photons measured with the PbGl and the PbSc in* $\sqrt{(}s_N N)$ *= 200 GeV Au+Au Collisions (Run02)*, PHENIX analysis Note **An353**, 2005.

[RHIC] http://www.bnl.gov/RHIC/, 2006.

[Sah04] B. Sahlmüller, *Production of* η *Mesons in* $\sqrt{s_{NN}}$*= 200 GeV d+Au and p+p Collisions Measured by the PHENIX Experiment*, Diplomarbeit, Institut für Kernphysik, Universität Münster, 2004.

[Sch94a] G. Schepers. *Entwicklung und Erprobung eines LED-gestützten Monitorsystems für ein modulares Bleiglasspektrometer*. Diplomarbeit, Institut für Kernphysik, Universität Münster, 1994.

[Ste01] F.D.Steffen. *Phys. Lett.*, **B510** (2001) 98.

[Tho01] A. W. Thomas and W. Weise. *The Structure of the Nucleon.* WILEY-VCH, Berlin, 2001.

[Tur03] Simon Turbide, Ralf Rapp, Charles Gale, *HADRONIC PRODUCTION OF THERMAL PHOTONS*, Phys. Rev. **C69** 014903, 2004.

[Wan92] X.-N. Wang and m. Gyulassy. *Phys. Rev. Lett.* **68** (1992) 1480.

[Wil74] K. G. Wilson, Phys. Rev. **D 14** (1974) 2455.

[Won94] C.-Y. Wong, *Introduction to High-Energy Heavy-Ion Collisions*, World Scientific Publishing Co., 1994.

[Zau05] O. Zaudtke et. al., *Search for Direct-Photons in p+p-Collisions at* $\sqrt{s}$ *= 200 GeV in Run III - Preliminary (PbGl)*, PHENIX Analysis Note **An478**, Universität Münster, 2005.

Danksagung

Schließlich und endlich möchte ich mich bei all denen bedanken, die zum Gelingen dieser Arbeit beigetragen haben.

Prof. Dr. Johannes P. Wessels danke ich dafür, dass er mir das Schreiben dieser Arbeit ermöglicht hat. Bei PD Dr. Klaus Reygers möchte ich mich für die Betreuung meiner Arbeit bedanken. Seine unermüdliche Diskussionsbereitschaft, die zahlreichen Anregungen und die Hilfestellung bei physikalischen und technischen Fragestellungen haben diese Arbeit entscheidend vorangebracht. Aus den selben Gründen möchte ich mich bei Oliver Zaudtke, Dr. Christian Klein-Bösing, Dr. Stefan Bathe, Dr. Henner Büsching und Baldo Sahlmüller bedanken. Für die kritische Durchsicht meiner Diplomarbeit danke ich besonders Christoph Baumann, Dr. Christian Klein-Bösing, Dr. Helmut Neukirchen, PD Dr. Klaus Reygers und Baldo Sahlmüller. Darüber hinaus möchte ich für das gute Klima im Büro Alexander Wilk, Melanie Hoppe, Jan Fiete Grosse-Oetringhaus, Katharina Büscher und Markus Rammler danken.
Außerdem bin ich froh darüber viele neue Freunde und Bekannte in der Arbeitgruppe gefunden zu haben.
Für die angenehme Arbeitsatmosphäre und ihre Unterstützung gilt mein Dank der gesamten PHENIX Kollaboration sowie allen aktuellen und ehemaligen Mitgliedern der Arbeitsgruppe: B. Bathen, C. Baumann, K. Büscher, D. Emschermann, Dr. R. Glasow, H. Gottschlag, N. Heine, M. Hoppe, H. Hünteler, PD Dr. A. Khoukaz, M. Rammler, Prof. em. Dr. R. Santo, W. Verhoeven und den schon oben genannten.

Schließlich danke ich meinen Eltern, dass sie mir das Studium der Physik ermöglicht haben, und meiner ganzen Familie sowie Christina, die mich fortwährend bei der Verwirklichung meiner Ziele und unterstützt haben.

Eigenständigkeitserklärung

Ich versichere, diese Arbeit selbstständig verfasst und keine anderen als die angegebenen Hilfsmittel und Quellen benutzt zu haben.
Münster, 21. Februar 2006

Jan Auffenberg